KTH CICERO

CFD of Duct Acoustics
for Turbocharger Applications

Emma Alenius

Licentiate Thesis

Postal address	**Visiting address**	**Contact**
Royal Institute of Technology	Teknikringen 8	+46 8 790 6757
MWL/AVE	Stockholm	ealenius@kth.se
SE-100 44 Stockholm		
Sweden		

CFD of Duct Acoustics for Turbocharger Applications

Emma L. Alenius 2010

KTH Department of Aeronautical and Vehicle Engineering
SE-100 44 Stockholm, Sweden

Abstract

The search for quieter internal combustion engines drives the quest for a better understanding of the acoustic properties of engine duct components. In this work the main focus is the turbocharger compressor and a discussion of turbocharger acoustics and earlier work within the area is presented, giving an insight into its sound generating mechanisms and the damping effect it has on pressure pulses, i.e. incoming waves. However, despite the fact that turbo-charging was developed during the first part of the 20th century, there is not much research results available within the area of centrifugal compressor acoustics.

To improve the understanding of the acoustics of engine duct components, methods based on compressible Large Eddy Simulation (LES) are explored. With these methods it is possible to capture both the complex flow, with sound generating mechanisms, and acoustic - flow interactions. It is also possible to get a detailed insight into some phenomena by access to variables and/or areas where it is difficult to perform measurements. In order to develop these methods the linear scattering of low frequency waves by an orifice plate have been studied, using an acoustic two-port model. This simple geometry was chosen since the flow has several of the characteristics seen in a compressor, like unsteady separation, vortex generation and shock waves at high Mach numbers. Furthermore the orifice plate is in itself interesting in engine applications, where constrictions are present in the ducts. The results have been compared to measurements with good agreement and the sensitivity to different parameters has been studied, showing an expected dependence on inlet Mach number and difficulties to simultaneously keep the amplitude low enough for linearity and high enough to suppress flow noise with the short times series available in LES.

During the development of new engines the industry uses 1D engine CFD tools. These tools are developed to give performance data, but sometimes also the acoustic pulsations are studied. The duct components are modelled and the turbocharger is often modelled with a map, representing its fluid mechanical properties measured under steady state conditions. An aim in this work has been to study the limitations of the models available in the commercial software GT-Power. The scattering of incoming waves was simulated and the results were compared to measurements, showing a large discrepancy for the compressor and a significant discrepancy for the orifice plate.

Descriptors: Aero acoustics, large eddy simulation, IC-engines, 1D models, Turbocharger, Orifice Plate.

The more I learn, the more I learn how little I know.

Socrates (469 BC - 399 BC)

Contents

CHAPTER 1

Introduction

Noise from road vehicles is one of the main sources of community noise in the world. Noise is thereby an important issue in vehicle design, both due to tougher noise legislations and higher demands on driver experience and comfort. For lower speeds the engine related noise gives the dominating contribution to the noise from road vehicles. In general the aim is to reduce the engine exterior noise, but in some cases, e.g. for sports car engines, it is also of interest to tune the noise (mainly the interior) to give a specific easily recognized sound.

The main noise source in an internal combustion engine is the cylinders. The low frequency pulsations generated there propagate through the intake and exhaust ducts to be radiated by the air intake respectively the exhaust pipe. All duct components will influence the sound propagation and this influence is called the components passive acoustic properties. The duct components will also generate noise, which is the components active acoustic properties, and this will contribute to the overall sound of the engine. So to understand the acoustics of the engine each duct component must be studied. In this work, it is the acoustic properties of the turbocharger compressor that are the main interest, but a simpler geometry consisting of a constriction is also considered.

Turbochargers consist of a turbine and a compressor and are used to increase the power output of an engine for a given engine size. The turbine, which is driven by the exhaust gases, drives the compressor, which compresses the air going into the cylinders. Turbochargers are today used in most modern diesel engines and their use in spark ignited engines is increasing due to the trend of engine down-sizing. Despite this and the fact that turbo-charging was developed during the first part of the 20th century, there are not much research results available within the area of turbocharger acoustics. The research within turbine and compressor acoustics has mainly been conducted for axial machines, such as jet engines where noise traditionally has been more of a problem. The acoustics of turbochargers is however becoming an issue due to the trend of making smaller faster turbochargers, where the generated acoustic power increases rapidly with the rotational speed. In general it can be said that the turbocharger has a damping effect on incoming low frequency waves, at the same time as it generates a high frequency noise. In this thesis a discussion of the damping effect of the turbocharger and known sound generating

mechanisms is presented, together with an overview of earlier work that has been performed within these areas.

Constrictions are common objects in duct systems, such as those found in internal combustion engines. The constriction studied in this work is a thin orifice plate, i.e. a plate with a centrally located orifice, placed in a circular duct. By reflecting and damping incoming acoustic waves these constrictions will modify the resonances in the system, which can result in very high sound levels. The noise generated by a constriction can normally be neglected compared to other sound sources in the system, but under certain flow configurations it can cause a high tonal noise (whistle) if it couples to a resonance in the system. Besides the acoustic effect a constriction has on the engine, it is also of interest as a simple geometry for exploring computational methods to study the acoustics of compressible flows in IC-engine related geometries. The computational effort for the constricted pipe is much smaller than that for a compressor, at the same time as the flow is expected to have several of the important characteristics seen in a compressor; such as unsteady separation, vortex generation and shock waves.

To improve the understanding of the acoustic properties of engine duct components direct noise computations are performed, using compressible Large Eddy Simulation (LES). With this method sound generating mechanisms can be captured, as well as the interaction between the flow and incoming waves. To compute the scattering, i.e. reflection and transmission, of incoming waves and the generated sound from the simulation results an acoustic two-port model is used. In this thesis the above methodology for studying the acoustics of duct components is presented and applied to compute the scattering of incoming waves by a ducted orifice plate. To validate the method, the results are compared to measurements and theory.

In industry 1D CFD tools for engine simulations are often used during the development phase of new engines. In these tools the entire engine, including combustion and the turbocharger, is simulated and the engine components are modelled using different types of models. The programs are optimized for producing performance data, but the acoustic pulsations are an integral part of the simulations. Turbochargers are represented by zero or one dimensional models, which usually cannot capture the interaction with acoustic waves correctly. There are however models that are capable of capturing the low frequency response of the compressor, as shown by Rämmal & Galindo (2010). In this thesis the possibility of studying wave propagation with models present in GT-Power, a common commercial 1D CFD tool, is investigated by studying the interaction between incoming sound waves and a compressor and an orifice plate, respectively.

CHAPTER 2

The Turbo Charger

2.1. Introduction

Turbochargers are today used in most modern diesel engines of all types and sizes and their use in gasoline engines is increasing due to the trend of engine down-sizing. A turbocharger consists of a compressor and a turbine. The energy available in the hot exhaust gases is used to drive the turbine, which via a shaft drives the compressor that compresses the intake air. The power output of the engine depends on the amount of fuel burned per engine cycle, which in turn depends on the amount of fresh air available in the cylinders. By compressing the air going into the cylinders the compressor will thereby allow for a higher power output at a given engine size, or a smaller engine at a given power output. This results in less losses and thereby improved efficiency. (Heywood 1988)

In small internal combustion engines, e.g. automotive or truck engines, centrifugal compressors and radial turbines are in general used. The reason for this is that small radial turbo-machines have higher efficiency than small axial machines, which have a large relative tip clearance and a bad blade length to height ratio. An example of a radial turbocharger can be seen in Figure 2.1. As for all fluid machines the turbine and the compressor, respectively, consist of a rotor and a stator. The rotor is a rotating wheel, which extracts or adds work to the fluid. The stator is the stationary part, which accelerates and expands or decelerates and compresses the fluid.

The compressor consists of a rotor, a diffuser and a volute, where the two latter components together form the stator, see Figure 2.1. Air is drawn axially into the rotor that adds energy to the fluid and redirects the flow to the radial direction. The diffuser then converts some of the added kinetic energy to potential energy before the volute, which further diffuses the air and redirects the flow to the axial direction. (Dixon 2005)

The turbine is built up similarly to the compressor, but there are more variations in the turbine design. In Figure 2.1 a nozzle-less twin entry turbine can be seen. The exhaust gases first enter the volute, which adds a considerable swirl velocity to the gas and forces it out in the radial direction, thereby distributing it around the rotor. The gas then passes the rotor where part of
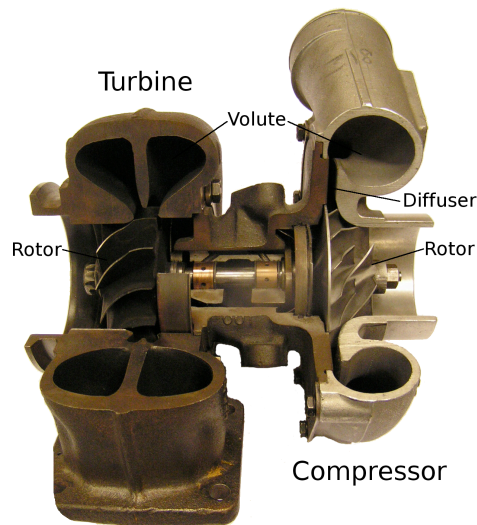
FIGURE 2.1. A turbocharger unit, with the turbine to the left and the compressor to the right.

its energy is used to drive the wheel, which in turn drives the compressor, and the flow is redirected into the axial direction. It is possible to add a nozzle with guide vanes between the volute and the rotor, resulting in additional flow turning and acceleration of the gas. This can normally make the turbine aerodynamically more efficient and the volute can be made smaller for the same expansion ratio. Furthermore, in so called variable geometry turbines nozzle blades of variable angle are used to change the working characteristics of the turbine to better match the engine operating point. (Baines (2005).) The variable geometry turbines are today commonly used in diesel engines. In gasoline engines the exhaust temperature is higher, which puts more strain on movable vanes, so normally nozzle-less turbines are used due to cost reasons.

For multiple cylinder engines the exhaust manifold and the turbine volute can be split into multiple entries. Different cylinders are then connected to different entries giving less interference between the cylinders. Commonly twin entry turbines are used, where the volute is split into two entries. This can be done by splitting the volute in the meridional direction, where both entries feed the whole periphery of the rotor, see Figure 2.1. An alternative is a volute where each entry feeds a sector of the rotor.

Depending on the type of compressor or turbine different amount of the expansion or compression occur in the rotor and in the stator. This is described by the degree of reaction (R), which usually is defined as the ratio of static

enthalpy change in the rotor to the total enthalpy change over the unit (or stage in the case of a multi stage turbo-machine) (Japikse & Baines 1994):

$$R = \frac{\Delta h_{rotor}}{\Delta h_{0,unit}}$$

For a unit where the expansion or compression is the same over the stator and rotor $R = 0.5$. When all the expansion or compression takes place in the stator $R = 0$, which is the case for some axial turbines. The opposite, $R = 1$, is very uncommon. In general the degree of reaction is most important as a design parameter for axial turbines, since for axial compressors and radial turbines or compressors the reaction is generally constricted by other design parameters. The degree of reaction is determined by the blade shapes and angles, which for radial machines often are restricted by other factors. (Japikse & Baines 1994)

The turbine, which is situated after the exhaust manifold just downstream of the cylinders, is working under highly pulsatile conditions. The frequency and the amplitude of the pulsations depend on the number of cylinders, their size and the engine operation point. The compressor, which is situated upstream of the cylinders, before the inlet manifold and the intercooler, is also subjected to flow fluctuations. They are of the same frequency as the pulsations in the turbine, but have a much lower amplitude.

2.2. Compressor Performance

Two important parameters of a turbocharger compressor are the pressure ratio and the efficiency. The former is important because it determines the boost pressure, i.e. how much more air that is pressed into the cylinders compared to a naturally aspirated engine, while the latter affects the efficiency of the entire turbocharger and thereby also the engine. Another important parameter is the flow rate, since the compressor only can operate stably within a certain range of flow rates.

Turbocharger compressors and turbines are characterized with performance maps, an example of a compressor map can be seen in Figure 2.2. These maps represent the fluid mechanical properties of the device and relate its rotational speed, mass flow, pressure ratio (total to total for compressor, total to total or total to static for turbine) and efficiency. The maps are measured under steady state conditions for several operating points and the data is interpolated to intermediate points. The turbine and compressor maps are normally presented in the form of reduced or corrected mass flow and speed (GT-Power 2004):

$$\dot{m}_{\text{corrected}} = \dot{m}_{\text{actual}} * \sqrt{\frac{T_{\text{inlet}}}{T_{\text{reference}}}} \Big/ \frac{p_{\text{inlet}}}{p_{\text{reference}}} \tag{2.1}$$

$$\dot{m}_{\text{reduced}} = \dot{m}_{\text{actual}} * \sqrt{T_{\text{inlet}}}/p_{\text{inlet}} \tag{2.2}$$

$$\text{rpm}_{\text{corrected}} = \text{rpm}_{\text{actual}} \Big/ \sqrt{\frac{T_{\text{inlet}}}{T_{\text{reference}}}} \tag{2.3}$$

$$\text{rpm}_{\text{reduced}} = \text{rpm}_{\text{actual}}/\sqrt{T_{\text{inlet}}} \tag{2.4}$$

where T is the temperature and p is the pressure. These corrections are performed to reduce the dependency of the results on the temperature and pressure conditions during measurements compared to different conditions during real operation, e.g. high temperatures. What these corrections really do is that they scale the results with the Mach number. The corrected mass flow and rpm are defined as the values that give the same axial respectively blade Mach numbers under reference condition as the respective Mach numbers in the measurements. The reduced variables are the mass flow and rpm rescaled to Mach numbers representing the axial respectively blade Mach numbers at the measuring conditions, neglecting geometry and gas constants.

2.2.1. *Operation Range*

The flow through the compressor is only stable within a certain range of mass flows. At lower mass flows the compressor enters surge, which is an unsteady system phenomenon where the flow breaks down and can be reversed at the compressor inlet. It is accompanied by high amplitude pressure pulsations that produce very high sound levels and can cause the machine to fail. At higher mass flows the compressor is choked as the flow reaches Mach one at the smallest cross-section and the efficiency drops fast.

Choking sets a limit for the flow capacity of the compressor. As the mass flow is increased and choke is approached areas of transonic flow appear and the losses increase drastically. This leads to reduced efficiency and pressure ratio, which can be seen to the right in the compressor map, Figure 2.2, where the efficiency and pressure ratio decrease rapidly with increasing mass flow for a constant compressor speed (Baines 2005). At this point the mass flow can only be increased by increasing the rotational speed of the compressor. (Dixon 2005)

Surge sets a limit for the minimum flow rate through the compressor at a given pressure ratio. The left end of the compressor map, see Figure 2.2, usually represents the onset of surge, but since it is a system phenomena it is difficult to predict and it can depend on other components like the intercooler (cools the air after the compressor) and the inlet manifold. (Baines 2005)
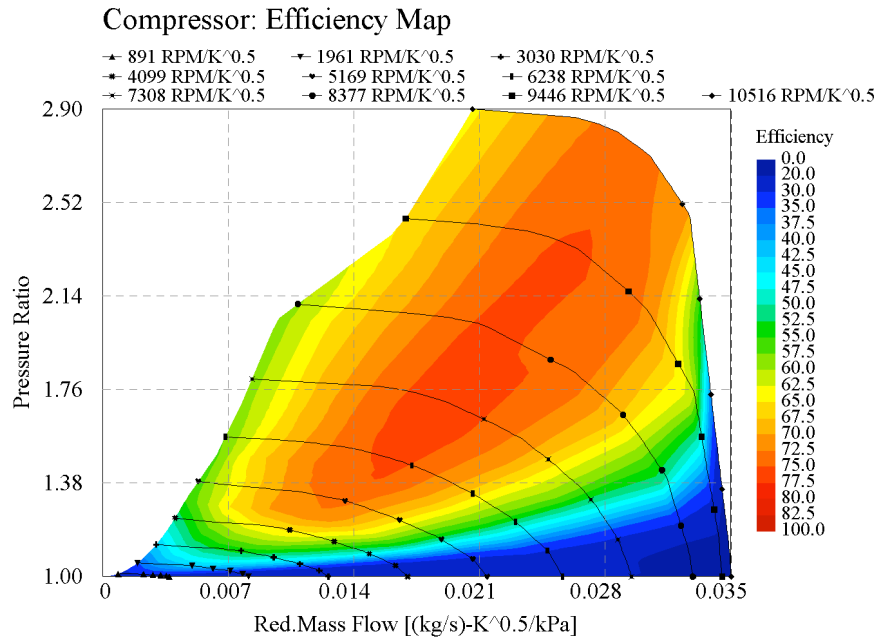
FIGURE 2.2. Performance map for a turbo-compressor. The dots on the speed-lines indicate the operating points where measurements have been performed, while the rest of the map is an interpolation from these points.

Surge is a complex phenomenon that is not well understood. It is believed to begin with stall, which occurs at low flow rates when an adverse pressure gradient causes the flow to separate from a surface. Stall can occur in any part of the compressor, one important example is blade stall when the flow separates from the suction side of a blade. When separation occurs the flow no longer follows lines parallel to the surfaces and there is an aerodynamic blockage of the flow, leading to a loss of total pressure. As the stall becomes stronger or starts to appear in several components of the compressor the pressure ratio eventually starts to decrease with the mass flow rate. (Baines 2005)

In the normal operating range of the compressor the pressure ratio increases with decreasing mass flow rate, see Figure 2.2. However, as surge is approached and stall appears in the compressor the increase becomes very small and eventually the pressure ratio starts to decrease with the mass flow, which occurs to the left of the operating points shown in the map. When the compressor operates at a point where the speed line, i.e. the line with constant rpm going through that point, has a negative slope the pressure increase with decreasing

flow. A small negative disturbance in the mass flow will then result in an increased pressure ratio, but as the disturbance is removed the flow goes back to the original operating point. When the compressor operates at a point where the speed line has a positive slope a small negative disturbance in the mass flow will result in a decreased pressure ratio. The air delivered from the compressor to the inlet manifold will now have lower pressure than that in the manifold, resulting in a pressure wave that propagates upstream through the compressor. This will enhance the stall, giving even lower mass flows and pressure ratios until the mass flow is very small. At this point the compressor can go back to the original operating point, where a small disturbance will cause the whole process to repeat itself. (Baines 2005)

Rotating stall (RS) is a famous phenomena that is observed in axial machines, while its occurrence in radial machines is unknown. An introduction to RS can be found in Kameier & Neise (1997). It appears when the rotating machine operates at low flow rates and some local disturbances lead to stall on one of the blades. This means that the flow separates at the tip of the blade at the suction side so that blade passage is partially blocked. The flow is then diverted away from this passage to a neighbouring one, increasing the angle of attack to that blade causing the flow to stall. The flow angle is then reduced at the pressure side of the originally stalled blade so that it becomes un-stalled. This way the stall cell moves around the rotor in the opposite direction to that of the blades in the rotor frame of reference, but slower than the rotational speed. Hence, in a fixed reference frame it moves in the rotation direction, but at a slower rate than the blade. More than one stall cell is also possible. The stall cell moves around the rotor in a more or less frozen pattern, i.e. if one follows the cell one can hardly experience any variations in the flow field with time.

2.3. 1D & 0D Models for Turbochargers in Pulsatile Flow

For engine design purposes it is important to have a fast and simple model for the turbocharger. The compressor and the turbine are often modelled with their performance maps, assuming quasi-steady flow. This is for example the case in the two commonly used commercial 1D CFD codes for engine simulations GT-Power and BOOST, where the map is used as a boundary condition between two attached pipes. The maps are however used differently in the two programs. For the compressor modelling GT-Power uses the rotational speed and the pressure ratio between the attached pipes to interpolate the mass flow from the map. In BOOST the rotational speed and the mass flow are used to interpolate the pressure ratio and the isentropic efficiency from the map.

In addition to using turbocharger maps many different models have been proposed either for model simplification or for improved modelling performance under pulsatile flow. Most of these models are for the turbine, since it is situated downstream of the cylinders where the amplitude of the pulsations is

much higher. Here a few non-linear models that have been proposed in the literature will be presented.

2.3.1. *Compressor Models*

Torregrosa *et al.* (2006) have suggested a model for the compressor. In the model the map is used as a boundary condition between two cavities that are connected to the engine ducts. The volumes represent the volume inside the compressor and they are supposed to account for the effect of accumulation of mass, which takes place in the compressor under pulsating flow conditions. Both volumes are set to have equal size, which is half the size of the total volume inside the compressor.

To get the desired characteristics from the model the connection between the map and the cavities was implemented in a certain way. Using the pressure in the adjacent cavities at the previous time-step and the rotational speed, the mass flow through the compressor and the efficiency are obtained from the map. This is used to calculate the stagnation temperature at the compressor outlet and the turbo-compressor work performed. Finally the new thermodynamic conditions inside the cavities are calculated by applying equations for mass conservation and energy balance at each cavity.

To check the above model it was integrated into a general engine gas exchange model, which was able to supply the required boundary conditions. The simulation results were compared to measurements performed on an engine, for one truck and one automotive turbocharger. One operating point per turbocharger was simulated and the comparison was performed in both time and frequency domain, up- and downstream of the compressor, for the pressure and the up- and downstream propagating waves. In general the results of the model are acceptable, with better results at the downstream side and for the automotive turbocharger.

Rämmal & Galindo (2010) later used the model developed by Torregrosa *et al.* (2006) to simulate the passive acoustic properties of a turbocharger compressor. The compressor model was connected to two ducts, at the end of which sound waves were excited. A difference between this model and the original one was that the volumes were not set to equal size. Instead, they were set equal to the volume before and the volume after the rotor. The transmission loss and the scattering matrix were calculated as a function of frequency for several operating points of the compressor. The results were compared to measurements performed by Rämmal & Åbom (2009) with good agreement.

2.3.2. *Turbine Models*

The simplest way to model the turbine is to replace it with a nozzle, a model that has been outlined by Watson & Janota (1982). The effective area of the nozzle should be set so the pressure drop matches that of the turbine for the

same value of the mass flow. A realistic value for the equivalent turbocharger efficiency can be obtained by a few trial and error simulations with different nozzles. The model can represent the flow characteristics of a turbine reasonably well, except for the case of radial turbines with high expansion ratios (above 1.83), which turbocharger turbines usually have.

A more advanced model has been proposed by Payri *et al.* (1996). It consists of two convergent nozzles with an intermediate volume. Twin entry turbines are handled by having two, instead of one, nozzles in parallel into the intermediate volume. The nozzles represent the stator, which produces the first expansion of the flow, and the rotor, which further expands the flow, assuming quasi-steady flow behaviour. The intermediate volume should account for the accumulation of mass that takes place in the turbine during pulsating flow. The size of the volume should be similar to that inside the turbine. However, simulations with different volume sizes (0.5V, V and 2V) showed that the time domain results are insensitive to errors in the volume size. This implies that low frequency pulsations are insensitive to volume size, but it is not know how higher frequency waves are affected.

In the model the effective areas of the nozzles are determined from the characteristic curves of the turbine, supplied by the manufacturer, under the assumption that the reaction degree of the turbine is 0.5. This means that the expansion ratio is assumed to be the same for the stator and the rotor, which usually is true for radial turbines running at their design point. For pulsating flow the turbine operating point is different in every time-step so the effective area of the nozzles should be constantly updated. This is a time consuming operation, so it is suggested to keep the stator area constant, while the rotor area is calculated for each engine operating point or to keep both areas constant at their mean values. Simulations showed that calculating the rotor area at every time-step had a small influence on the resulting pressure pulses in the time domain.

Results from simulations using the above model were compared to measurements performed on a turbine in an engine test-bench. Good agreement was found for the average mass flow rate and the turbine work as a function of rotational speed. For the instantaneous pressure variations, at the exhaust port and the turbine outlet, the agreement was acceptable.

An extension to the above model for variable geometry turbines has been proposed by Serrano *et al.* (2008). The model is essentially the same as the one proposed by Payri *et al.* (1996), with the difference that the expansion ratio is not assumed to be the same for stator and rotor. Instead the reaction degree of the turbine is calculated using geometrical parameters and the turbine performance map. The reaction degree is then used when the effective areas of the stator and rotor nozzles are calculated. The model was implemented in a 1D CFD code together an engine model. Simulation results were compared

to measurements performed on three turbines in an engine test bench. The comparison showed that the model is capable of capturing the fluid-dynamic behaviour of the turbine in time domain for all three turbines. For one turbine the results were also compared in frequency domain, with acceptable results.

Baines (2005) has suggested a model for the turbine that has similarities to the model by Payri *et al.* (1996). The volute is modelled with a cavity, where accumulation of mass takes place during pulsating flow, giving a damping effect on the pulsations and thereby a smoother inflow to the rotor. The volume is followed by the rotor, which is modelled on a quasi-steady bases. The rate of change of mass in the cavity is determined by the difference between the mass flow into the volute and the mass flow out from the volute to the turbine. This is then related to the rate of change of pressure in the cavity by means of the perfect gas equation. The mass flow going into the rotor has to be determined from a simple 1D model of the turbine rotor, given the rotor pressure ratio, the shaft speed, the rotor overall dimensions and an estimate of the rotor efficiency. The model is tested and gives a turbine performance consistent with measurements, i.e. it captures the essential features of the pulsations.

Chen *et al.* (1996) have proposed a 1D model for a mixed flow turbine, which was an improvement of the earlier model presented by Chen & Winterbone (1990) for radial turbines. The turbine casing is modelled as a converging duct. The spiral part is modelled as a pipe with a length equal to the length from the tip of the casing tongue to a 180° azimuthal angle. The volume of the casing can be set correctly by properly defining the pipe area. 1D unsteady flow analysis is then applied to the converging pipe. This model gives a length to the casing, which can be important in unsteady flow analysis. The rotor is simulated with a quasi-steady flow method, since the Strouhal number of this part is small. Several loss models are then introduced into the simulation model to improve predictions at off design points.

The simulation results were compared to measurements and simulations with a quasi-steady model. The instantaneous mass flow rate was captured better with the new unsteady method than with the quasi-steady model, but none of the models gave good results. For the fluctuating turbine power both models showed poor agreement with the measurements, even though the new model slightly improved the results.

CHAPTER 3

Aero-Acoustics

Acoustic problems have two parts, sound generation and sound propagation and scattering, i.e. reflection and transmission of waves by objects. In this chapter there will be an introduction to sound propagation, scattering and generation. For more information please refer to a book like Pierce (1989) or Howe (1998). The chapter will further include an introduction to computational aero acoustics and an introduction to the acoustics of turbocharger compressors and ducted orifice plates.

3.1. Wave Propagation and Scattering

3.1.1. *Sound Propagation in Ducts*

Acoustics waves are disturbances from a mean fluid state that propagate with the speed of sound. The acoustic fluctuations can be seen in all fluid variables, but the theory will be presented using the acoustic pressure, which is later related to the other variables. The amplitude of acoustic fluctuations is normally very low compared to the mean variables in the fluid and the propagation is therefore often assumed to be linear. This assumption holds up to amplitudes of around 1 % of the mean values. First the theory for linear propagation in an ideal stationary fluid will be presented and then the effect of flow, dissipation and non-linearities will be discussed. The linear propagation of sound in a stationary fluid is described by the homogeneous wave equation:

$$\frac{\partial^2 p'}{\partial t^2} - c^2 \nabla^2 p' = 0 \qquad (3.1)$$

Where p' is the acoustic pressure and c is the speed of sound. The solution to the homogeneous wave equation in 1 dimension is:

$$p'(t, x) = f(x - ct) + g(x + ct) \qquad (3.2)$$

Where f and g are two (plane) waves that propagates in the positive and negative x-direction, respectively.

Special types of waves are harmonic waves. They have a time dependence that is proportional to $\sin(\omega t)$ and $\cos(\omega t)$, where $\omega = 2\pi f$ is the angular frequency and f is the frequency. However for simplicity the time dependence

is often written as a complex exponential, $e^{-i\omega t}$. The harmonic behaviour also means that the wave has a fixed wavelength, $\lambda = c/f$, which corresponds to the length one period of the wave occupies in space. Harmonic waves are important in many practical applications, because acoustic waves with more general time dependence can be written as a sum of their harmonic components. If this is combined with the solution to the homogeneous wave equation, Equation (3.2), the 1D acoustic pressure fluctuations can be written as:

$$p'(t,x) = \sum_{n=1}^{\infty} \hat{p}_{+n}e^{i(k_n x - \omega_n t)} + \hat{p}_{-n}e^{i(k_n x + \omega_n t)} \tag{3.3}$$

Where $\hat{p}_{+n}$ and $\hat{p}_{-n}$ are the complex valued Fourier amplitudes of the up- and downstream propagating waves at each frequency ω_n and $k_n = \omega_n/c$ is the wavenumber, which is related to the wavelength as $k = 2\pi/\lambda$.

In a duct it is convenient to express the wave equation, Equation (3.1), in cylindrical coordinates, which gives:

$$\frac{1}{c^2}\frac{\partial^2 p'}{\partial t^2} - \frac{1}{r}\frac{\partial}{\partial r}\left(r\frac{\partial p'}{\partial r}\right) - \frac{1}{r^2}\frac{\partial^2 p'}{\partial \varphi^2} - \frac{\partial^2 p'}{\partial x^2} = 0 \tag{3.4}$$

Where r is the radial direction and φ is the angle in the azimuthal direction. The solution to this wave equation for a harmonic wave in a cylindrical duct with rigid wall is a sum of modes, which have specific pressure patterns at cross sections of the duct:

$$p'_{\pm} = \sum_{m=0}^{\infty}\sum_{s=0}^{\infty}[A_m\cos(m\varphi) + B_m\sin(m\varphi)]J_m(k_{r,ms}r)e^{i(k_x x \pm \omega t)} \tag{3.5}$$

$$J'_m(k_{r,ms}R) = 0 \tag{3.6}$$

$$k_{r,ms}^2 + k_{x,ms}^2 = k^2 = (\omega/c)^2 \tag{3.7}$$

Where m and s are the azimuthal respectively radial mode orders, k_x and $k_{r,ms}$ are the wave numbers in the axial and radial directions, A_m and B_m are amplitudes, J_m are the Bessel functions of the first kind, R is the radius of the duct and $\pm$ is for up- or downstream propagating waves, where the total acoustic pressure is retrieved by summing these two waves.

The constriction on the radial wave number gives that only wave numbers $k_{r,ms} = \pi\alpha_{ms}/R$ are allowed, where $\pi\alpha_{ms}$ is solution number s to $J'_m = 0$ and can be found in tables. Furthermore, the relation between the radial and axial wave numbers gives that k_x becomes imaginary when $\pi\alpha_{ms}/ka > 1$. This means that the mode cannot propagate in the duct, instead the amplitude decays exponentially along the duct. The frequency at which a certain mode starts to propagate in the duct is called the cut on, or cut off, frequency for that mode. For low frequencies only the plane wave mode ($m = 0$ and $s = 0$), which

has constant pressure at duct cross-sections, can propagate. This corresponds to a one dimensional wave.

The acoustic pressure can be linearly related to the acoustic density (ρ') and velocity (u') through the plane wave relation:

$$p' = c^2 \rho', \qquad p'_\pm = \pm \rho_0 c u'_\pm \qquad (3.8)$$

Where ρ_0 is the ambient, or mean, density and $\pm$ is for up- and downstream propagating waves.

The amplitudes of the up- and downstream propagating waves for the different variables can be related to the total amplitudes of the fluctuations in the following way:

$$p' = p'_+ + p'_-, \qquad \rho' = \rho'_+ + \rho'_-, \qquad , u' = u_+ - u_- \qquad (3.9)$$

When flow is introduced in the duct the problem becomes more complicated. The waves now propagate with the speed of sound plus/minus the flow speed (U) in the down- and upstream directions, respectively. This implies that the wave number becomes:

$$k_\pm = \frac{\omega}{c \pm U} = \frac{k_0}{1 \pm M} \qquad (3.10)$$

Where $M = U/C$ is the Mach number of the flow, k_0 is the wave number in the undisturbed fluid. However, the above theory with the mode shapes, the plane wave relation between the acoustic variables and the possibility to sum different waves to get the total acoustic fluctuations is still valid.

In the above theory it has been assumed that the fluid is ideal and there is no dissipation, i.e. a sound wave can propagate an infinitely long distance without a decrease in amplitude. In reality this is not true and the amplitude of the wave will decrease gradually. The decrease is however small and can often be neglected over short distances. If dissipation is accounted for it is done by adding a small complex part to the wave number ($k_d = i\alpha + k$). The amount of dissipation depends on the fluid and the duct diameter and it mainly occurs next to the wall in the thermo-viscous acoustic boundary layer. The dissipation is also affected by convection, see e.g. Dokumaci (1998), and for very low frequencies by turbulence, see e.g. Knutsson & Åbom (2010).

As the amplitude of the waves is increased the propagation becomes nonlinear. The shape of the wave will then be distorted as the wave propagates and energy will be transferred among different harmonics, i.e. waves with frequencies that are a multiple of the same base frequency f_0 ($f = nf_0$, $n = 1, 2, ...$). The distortion of the wave shape is in the form of wave steepening, where the wave front becomes more and more steep due to the compression part of the wave propagating slightly faster than the expansion part. This means
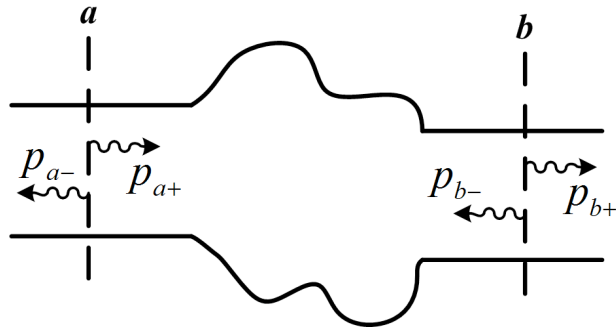
FIGURE 3.1. Definition of wave propagation directions for waves impinging on an object. The wave amplitudes are referred to a certain reference cross-section.

that the distance from the expansion to compression part of the wave decreases until eventually a shock wave is formed after the so called shock wave formation distance, which depends on the wave amplitude, see e.g. Pierce (1989).

3.1.2. *Wave Scattering*

When a sound wave impinges on an object it will partly be reflected, transmitted and absorbed. This effect of the object is known as its passive acoustic property.

Consider sound waves impinging on the general object in Figure 3.1. If $\hat{p}_{b-} = 0$, the reflection and transmission of $\hat{p}_{a+}$ are defined as $R(\omega) = \hat{p}_{a-}/\hat{p}_{a+}$ respectively $T(\omega) = \hat{p}_{b+}/\hat{p}_{a+}$. These quantities will be complex and contain information both about the amplitude of the reflection/transmission and if the object introduces a phase shift to the wave.

The reflection at boundaries is an important example of wave reflection. At a rigid wall the velocity is zero and there will be total reflection, $R = 1$. When a duct terminates into free space, or a large baffle, the pressure is approximately constant, implying that $p' \approx 0$ at the end of the duct. This will also give total reflection, but the reflected wave will be 180° off phase with the incoming wave, $R = -1$. However, in reality the pressure is not exactly constant and the reflection decreases for higher frequencies.

3.2. Sound Generation

There are different phenomena that can lead to the generation of sound. The aerodynamic sound sources are often divided into three categories. Within each category sound is generated by the same type of mechanisms, which in turn can be caused by different underlying phenomena. The three categories are termed monopole, dipole and quadrupole type of sources and are explained below.

Monopole type of sources correspond to sound generation by fluctuating volume flows. This can occur if there is unsteady flow injection from e.g. a tail pipe, unsteady heat injection from e.g. combustion or if the fluid is displaced by a moving surface, e.g. a loudspeaker. Another cause for this type of sound generation is high Mach number flows, where there are non isentropic flow fluctuations and the non-acoustic density fluctuations correspond to a volume fluctuation of the fluid.

Dipole type of sources correspond to sound generation by fluctuating surface forces. There are several different reasons as to why the surface pressure can fluctuate. For stationary surfaces it can be e.g. unsteady flow separation, unsteady vortex shedding or vortices hitting the surface. For moving surfaces it can be that the surface is moving through a non uniform flow field or with a varying velocity.

Quadrupole type of sources correspond to sound generation by free field turbulent fluctuations or by varying tangential shear stresses at a surface. The generated so called turbulence noise is broadband, just as the turbulent fluctuations. However, this is normally a very week source, except for in high speed jets with Mach numbers close to one, and it is therefore often neglected when there are monopole or dipole type of sources present.

In the presence of sources linear acoustics is governed by the wave equation with sources (S):

$$\left(\frac{\partial^2}{\partial t^2} - c^2 \frac{\partial^2}{\partial x_i^2} \right) \rho' = S(x_i, t) \tag{3.11}$$

In the absence of sources, i.e. in a free stationary field, this equation reduces to the classical homogeneous wave equation, Equation (3.1). The source term is determined by deriving the wave equation from the equations for conservation of mass and momentum. The oldest and most widely known wave equation with source terms is that by Lighthill (1952), which is derived without any simplifications, meaning that it is an exact equation. It represent sound generation by fluid fluctuations in a confined region of a free field, where the fluid is stationary. The Lighthill source term is:

$$S(x_i, t) = \frac{\partial^2 T_{ij}}{\partial x_i \partial x_j} = \frac{\partial^2}{\partial x_i \partial x_j} \left(\rho u_i u_j + P_{ij} - c^2 (\rho - \rho_0) \delta_{ij} \right) \tag{3.12}$$

Where T_{ij} is the Lighthill stress tensor, c is the speed of sound and ρ_0 is the density the fluid would have if it were at rest. $P_{ij} = p\delta_{ij} + \sigma_{ij}$ is the compressive stress tensor, where p is the pressure, σ_{ij} is the stress tensor and δ_{ij} is the Kronecker delta (vanishing if i and j differ and unity if they are equal to each other). The Lighthill source term represents a distribution of quadrupoles of strength density T_{ij}. However, in practice the Lighthill stress tensor (T_{ij}) will not only contain the generation of sound, but also the convection of sound with

the flow, the propagation of sound with variable speed and gradual dissipation by conduction and viscosity.

The most general form of the wave equation with aerodynamic sources is that for sound generation by turbulence and surfaces in arbitrary motion proposed by Ffowcs Williams & Hawkings (1969). This equation is, like the one by Lighthill (1952), derived without any simplifications. It is here presented for the case of impermeable surfaces, where the surface velocity equals the velocity of the fluid at the surface:

$$
\left(\frac{\partial^2}{\partial t^2} - c^2 \frac{\partial^2}{\partial x_i^2} \right) \rho' H(f) = \frac{\partial}{\partial x_i} \left(P_{ij} \delta(f) \frac{\partial f}{\partial x_j} \right) + \frac{\partial}{\partial t} \left(\rho_0 v_i \delta(f) \frac{\partial f}{\partial x_i} \right)
$$
$$
\frac{\partial^2}{\partial x_i \partial x_j} [T_{ij} H(f)] \tag{3.13}
$$

Here f is a marker function defining surfaces and non-fluid regions. It is defined so that $f = 0$ at surfaces, $f < 0$ inside solid objects and $f > 0$ in the fluid domain. $H(f)$ is a Heaviside function, which is chosen to be unity in the fluid domain and zero inside objects. $\delta(f)$ is the Dirac delta function, which is the generalized derivative of the Heaviside function. Furthermore, it is possible to write $\frac{\partial f}{\partial x_i} = |\nabla f| n_i$, where n_i is the normal vector of the surface.

The first term in Equation (3.13) ($\frac{\partial}{\partial x_j}(...)$) is only present on surfaces and represents a dipole distribution of source strength density $P_{ij} n_j$. The second term ($\frac{\partial}{\partial t}(...)$) is only present on moving surfaces. It is of monopole character and represents the volume displacement effect that occur as the surface moves through the fluid. The third term ($\frac{\partial^2}{\partial x_i \partial x_j}(..)$) is the Lighthill source term. If there are no surfaces present, only this source term remains and the equation is reduced to the classical equation by Lighthill (1952).

Since there is no simplification in the derivation of Equation (3.13) it is valid under subsonic, transonic and supersonic conditions. However, in the presence of shocks T_{ij} will contain discontinuities other than those at surfaces and hence the equation has to be reformulated.

Ffowcs Williams & Hawkings (1969) also studied possible solution strategies for the above wave equation. They came to the conclusion that for low speeds the surface generated sound is governed by the applied force and displaced inertia. However, for high speed problems they conclude that these mechanisms are negligible. For very high velocities an intense beam will instead be radiated in the direction for which the surface normal coincides with the Mach wave direction and the strength of this beam depends on the surface curvature.

3.3. Acoustic Two-Ports

An acoustic two-port gives the linear relation between the acoustic properties up- and downstream of a duct component as a function of frequency in the plane wave range. There are several different formulations of the two-port and here it is convenient to use the scattering matrix formulation, see Glav & Åbom (1997). The scattering matrix ($\mathbf{S}$) relates the amplitudes of the incoming ($\hat{p}_+$) and the outgoing waves ($\hat{p}_-$), up- (a) and downstream (b) of the component, see Figure 3.1 . In the general case the scattering matrix can be written as:

$$\begin{pmatrix} \hat{p}_{a-} \\ \hat{p}_{b+} \end{pmatrix} = \mathbf{S} \begin{pmatrix} \hat{p}_{a+} \\ \hat{p}_{b-} \end{pmatrix} + \begin{pmatrix} \hat{p}_{a-}^s \\ \hat{p}_{b+}^s \end{pmatrix}, \qquad \mathbf{S} = \begin{pmatrix} S_{11} & S_{12} \\ S_{21} & S_{22} \end{pmatrix} \qquad (3.14)$$

where S_{11} and S_{22} are the upstream respectively downstream reflection coefficients, S_{21} and S_{12} are the up- to downstream respectively down- to upstream transmission coefficients and p_a^s and p_b^s is the generated sound radiated in the up- respectively downstream directions. The elements of the scattering matrix will be complex and contain information about both the amplitude of the coefficients and a possible phase shift taking place between the up- and downstream sampling positions used for the acoustic variables.

To determine the four unknown scattering-matrix elements it is assumed that the level of the incoming sound is high enough to neglect the generated sound. Furthermore two independent cases, with different incoming waves, are required. This is achieved either by running with the acoustic excitation up- and downstream of the component, or by running with two different loads. Using the result from these two cases the scattering-matrix can be calculated from:

$$\begin{pmatrix} S_{11} & S_{12} \\ S_{21} & S_{22} \end{pmatrix} = \begin{pmatrix} \hat{p}_{a-}^1 & \hat{p}_{a-}^2 \\ \hat{p}_{b-}^1 & \hat{p}_{b-}^2 \end{pmatrix} \begin{pmatrix} \hat{p}_{a+}^1 & \hat{p}_{a+}^2 \\ \hat{p}_{b+}^1 & \hat{p}_{b+}^2 \end{pmatrix}^{-1} \qquad (3.15)$$

where 1 denotes the first case and 2 the second case.

When sampling of acoustic variables is performed it usually has to be done at a distance from the studied object. The reason is that it is desirable to avoid sampling in acoustic near fields or in regions with high flow fluctuation levels. In acoustic near fields there can be higher order modes, which rapidly decays further away from the object, and this might influence the result. In regions of high flow fluctuation levels it is difficult to extract the low amplitude acoustic fluctuations. When the sampling is performed at a distance from the object, the phase of the scattering matrix elements contain not only a possible phase shift due to the object, but also the phase shift from the wave propagation between the object and the sampling positions. To avoid this, the scattering matrix can be moved to the object with the following equation (Lavrentjev *et al.* 1995):

$$\mathbf{S}' = \mathbf{T}_+\mathbf{S}\mathbf{T}_-^{-1} \tag{3.16}$$

Where $\mathbf{S}'$ is the modified scattering matrix that has been moved to the object and $\mathbf{T}_\pm$ are:

$$\mathbf{T}_+ = \begin{pmatrix} e^{ik_{a+}x'_a} & 0 \\ 0 & e^{ik_{b+}x'_b} \end{pmatrix}, \qquad \mathbf{T}_- = \begin{pmatrix} e^{-ik_{a-}x'_a} & 0 \\ 0 & e^{-ik_{b-}x'_b} \end{pmatrix} \tag{3.17}$$

Where x_a and x_b are the distances from the up- and downstream measuring positions to the object and k_+ and k_- are the wave numbers for waves propagating in the up- respectively downstream directions at the up- (a) and downstream (b) sides of the orifice, see Equation (3.10). The phase of the modified scattering matrix is sensitive to the flow Mach number, meaning that a small error in the latter can give a significant effect on the scattering matrix, as shown by Holmberg (2010).

If the active part of the two port is to be determined in the case of reflecting boundaries, at the end of the ducts, the reflections at these boundaries and the scattering matrix of the object must be known. The reason is that some of the pressure fluctuations correspond to reflected waves that were generated earlier. The generated sound can then, according to Lavrentjev *et al.* (1995), be calculated with the following expression:

$$\mathbf{p^s} = (\mathbf{E} - \mathbf{SR})(\mathbf{E} + \mathbf{R})^{-1}\mathbf{p} \tag{3.18}$$

Where $\mathbf{E}$ is the identity matrix, $\mathbf{p}$ is the measured pressure up- and downstream of the object, $\mathbf{p^s}$ is the generated waves and $\mathbf{R}$ is the reflection matrix:

$$\mathbf{p} = \begin{pmatrix} p_a \\ p_b \end{pmatrix} \qquad \mathbf{p^s} = \begin{pmatrix} p_{a-}^s \\ p_{b+}^s \end{pmatrix} \qquad \mathbf{R} = \begin{pmatrix} R_a & 0 \\ 0 & R_b \end{pmatrix} \tag{3.19}$$

Where R_a and R_b are the reflections in the up- and downstream ducts.

To use Equation (3.18) to calculate the generated sound the scattering matrix and the reflection matrix have to be determined at the cross section where the pressure ($\mathbf{p}$) is sampled, which as stated earlier usually has to be at a distance from the object. The scattering matrix can be moved using Equation (3.16), where the distances x_a and x_b in Equation (3.17) have to be negative if it is moved further away from the object. The reflection matrix can be moved in a similar way:

$$\mathbf{R}' = \mathbf{T}_+^{-1}\mathbf{R}\mathbf{T}_- \tag{3.20}$$

Where the distances x_a and x_b just as for the scattering matrix have to be positive if it is moved closer to the orifice and negative if it is moved further

away. Sometimes it is also of interest to move the generated waves ($\mathbf{p^s}$) to the component, which can be done with (Lavrentjev *et al.* 1995):

$$\mathbf{p^{s\prime}} = \mathbf{T}_+^{-1}\mathbf{p^s} \tag{3.21}$$

Where $\mathbf{p^{s\prime}}$ is the modified source vector that has been moved to the component.

3.3.1. *Plane Wave Decomposition*

To compute the scattering matrix the sampled acoustic fluctuations have to be decomposed into up- and downstream propagating waves. To compute these waves a plane wave decomposition method is used. It is based on the assumption that the acoustic fluctuations can be written as a sum of the up- and downstream propagating waves, see Equation (3.9). If both the pressure and the velocity are available, which is the case in CFD, the plane wave relation, Equation (3.8), can be used to decompose the waves according to:

$$p_+ = \frac{1}{2}[p' + \rho_0 c_0 u'], \qquad p_- = \frac{1}{2}[p' - \rho_0 c_0 u'] \tag{3.22}$$

If only the pressure is available, which normally is the case in measurements, the wave is instead decomposed assuming harmonic waves:

$$p' = \hat{p}e^{-i\omega t} \tag{3.23}$$

$$p_+ = \hat{p}_+ e^{-i(\omega t - k_+ x)}, \qquad k_+ = k/(1 + M) \tag{3.24}$$

$$p_- = \hat{p}_- e^{-i(\omega t + k_- x)}, \qquad k_- = k/(1 - M) \tag{3.25}$$

where ω is the angular frequency, k is the wavenumber and M is the Mach number. By measuring the pressure at two positions ($x = 0$ (1) and $x = s$ (2)) the pressure can now be determined using the two-microphone method (see e.g. Chung & Blaser (1980)):

$$\hat{p}_1 = \hat{p}_+ + \hat{p}_- \tag{3.26}$$

$$\hat{p}_2 = \hat{p}_+ e^{ik_+ s} + \hat{p}_- e^{-ik_- s} \tag{3.27}$$

If the pressure is measured at more positions it is possible to get an overdetermined system, which reduces the error. Furthermore, with more measuring positions it is possible to solve the non linear system of equations to get also the wave numbers and the Mach number.

3.4. Transmission Loss

The transmission loss (TL) is a measure of how much of the acoustic power that is lost as a sound wave passes an object. More exactly it is the difference between the power of the wave approaching the object and the power of the transmitted wave when there is a reflection free termination. If the scattering matrix for the object is known the transmission loss is calculated as (Åbom 1991):

$$
TL = \begin{cases}
10\log\left(\frac{A_a(1+M_a)^2\rho_b c_b}{A_b(1+M_b)^2\rho_a c_a |T_a|^2}\right) & \text{Downstream} \\
10\log\left(\frac{A_b(1-M_b)^2\rho_a c_a}{A_a(1-M_a)^2\rho_b c_b |T_b|^2}\right) & \text{Upstream}
\end{cases}
\tag{3.28}
$$

Where A is the duct area.

3.5. Computational Aero Acoustics

Computational aero acoustics (CAA) is used to numerically solve acoustic problems. The most direct method is direct noise computation (DNC), where the acoustics is simulated as part of the flow through compressible non-linear CFD. This method theoretically works for all types of acoustic problems, but it is computationally very expensive and errors can be significant due to the amplitude of the acoustic fluctuations only being a small fraction of the mean flow values. There are different CFD models that can be used for DNC, but the most common is probably DNS for very simple geometries and LES for a bit more complex geometries. More information about LES for acoustics can be found in Wagner *et al.* (2007).

When wave propagation and scattering is studied linear methods are often used to reduce the computational cost. The exception is for cases that involve high amplitude oscillations and thereby non-linear propagation, like e.g. the buzz-saw noise generated in compressors at high rotational speeds or the high amplitude oscillations generated at the cylinders of an internal combustion engine or whistling phenomena where the acoustic amplitude grows until it is limited by non-linear effects. For simple cases of linear wave propagation there are analytical functions available. One example is sound propagation in a straight duct where the sound field is known at some plane. Another example is the free field propagation of sound from a source region to an observer. However, when the geometry becomes more complicated, the acoustic field is required in a larger region or flow effects on the propagation are important numerical methods are needed. This involves the solution of either the wave equation or some more complex set of equations, where the most common is the linearized Euler equations (LEE), which is the linearized flow governing equations where viscous effects have been neglected. The wave equation is

normally only solved for very simple geometries, while LEE, and similar methods, are used to solve more general wave propagation problems. Kierkegaard *et al.* (2008) e.g. used the linearized Navier-Stokes equations to simulate the scattering of sound waves by a ducted orifice plate.

Even though it is uncommon it is possible to do direct noise computations of linear propagation or scattering problems. This has been shown by Föller & Polifke (2010) and Föller *et al.* (2010), who successfully used LES with second order accurate numerical methods to compute the scattering by an area expansion and a t-junction, respectively. They simulated the entire 2-port in one simulation by using completely non-reflecting boundary conditions and different broadband excitation signals at all boundaries. The outgoing waves were then correlated to the different excitation signals and the two port was obtained with a Wiener-Hopf-Inversion technique.

Sound generation is essentially a non-linear phenomena, which means that non-linear methods are needed. Here a short summary of some methods will be presented, but for more information see e.g. Colonius & Lele (2004). If the acoustic field only is required in a confined small region close to the source region direct noise computations are often performed. An area where DNC commonly is performed is jet noise, where e.g. Bogey & Bailly (2007) performed a LES of a circular jet at Mach 0.6 and 0.9 and correlated the flow fluctuations at the jet centerline and shear layers with the radiated pressure fluctuations. Furthermore, Gloerfelt & Lafon (2008) performed a LES of a jet from a diaphragm in a duct. More information about DNC and its applications can be found in e.g. Bailly *et al.* (2010).

If acoustic information is required at a larger distance from the source hybrid methods are often used. In these methods the full non-linear equations are solved in the source region (i.e. a DNC is performed) and the result is used as input to some linear propagation equation. This is then used to propagate the sound to the observer and can be solved on a much coarser grid. The input to the propagation equation can either be in the form of source terms, which are computed in the source region and interpolated to the acoustic grid, or in the form of a boundary condition containing the generated acoustic fluctuations extracted from an integration surface around the source region. Using a formulation based on source terms has the advantage of giving information about the sound generation mechanisms. However it is not always possible to study the source terms individually at different positions in space, since acoustic fluctuations generated at different positions can be out of phase and cancel each other out rather than being added together. Although it might be possible to test which sources in which regions that have the largest impact on the resulting sound field. A disadvantage with using source terms is that the result is sensitive to phase errors in the solution, since this will cause errors in the source cancellation, which in turn can result in errors in the predicted sound levels. Another disadvantage is that the result is sensitive to the interpolation scheme

used to move data to the acoustic grid, as shown by e.g. Piellard & Bailly (2010). Furthermore, numerical errors can act as sound sources. If information about the source terms is not required the above problems can be avoided by using an integral method, i.e. by using an integration surface around the source region. The problem then becomes that the method is sensitive to where the integration surface is placed, since it is important to included all sources and that no turbulent fluctuations are interpreted as acoustic waves at the surface. This has been observed by e.g. Gröschel *et al.* (2008), who found a strong sensitivity to the position of the integration surface when using a hybrid methods based on LES and FFowcs Williams and Hawkings method.

The simplest types of hybrid methods are based on acoustic analogies, which are a rearrangement of the full flow governing equations into an equation with a wave propagation operator at the left hand side and the rest of the terms as sources on the right hand side. The most well known acoustic analogy is Lighthill's equation and a more general analogy is that by Ffowcs Williams & Hawkings (1969), Equation (3.13), see Section 3.2. The source terms in these type of analogies represent different sound generating mechanisms, see Section 3.2, and should therefore represent the amount of noise generated by the different mechanisms. The downside with the acoustic analogies is that it is the free-field wave equation that is solved, which does not include convection and refraction effects due to a mean flow. These effects are instead incorporated in the source terms, which implies that it could be difficult to separate the real acoustic sources from convection and refraction "sources" and the result becomes more sensitive to numerical errors. Furthermore, the quadrupole source term present in these acoustic analogies consists of a second derivative, which easily yields numerical errors. Ffowcs Williams and Hawkings analogy can however also be used as an integral method, which prevents these problems. This is a common method and it has been used by e.g. Lai & Luo (2007) to predict the noise from flow over an open cavity. Despite their shortcomings acoustic analogies can be useful in predicting the far-field sound and are often used, but then normally with higher order accurate numerical methods and for external flow problems where there is no flow outside the source region. There are however examples of acoustic analogies being used for internal flows, where Piellard & Bailly (2010) used Lighthill's acoustic analogy to compute the sound from a ducted diaphragm using data from second order accurate LES.

When it comes to the more complex hybrid methods available, LEE with source terms is the most common. A newer method, which has become popular but is not very tested yet, is the Acoustic Perturbation Equations (APE), which were derived by Ewert & Schröder (2003) from the linearized Euler equations with source terms. APE have the advantage over LEE of being hydrodynamically stable. This is observed in sheared flows, where LEE can become unstable when vortices that grow in shear layers are not damped by viscosity or non-linearities as they physically would be. The disadvantage with APE is that it

is developed for sound generation by vorticity and is inappropriate for other types of sound generation. There are also other methods available that have been proposed as corrections to LEE to avoid instable solutions, which also can be avoided by solving the equations in the frequency domain, but this will not be considered here. These methods have in common that they describe linear wave propagation in a mean flow and both this mean flow and the source terms are input to the equations. This is an improvement compared to the acoustic analogies, since it allows for a better separation of source mechanisms and convection and refraction effects and the methods are less sensitive to errors in the source data. When it comes to studying the sources themselves these methods have also proven capable of showing the origin of the sound for some cases. Addad *et al.* (2003) e.g. performed a hybrid LES - LEE simulation, of a forward-backward facing step, which clearly showed the acoustic pressure oscillations and their origin. Furthermore, Gröschel *et al.* (2008) performed a hybrid LES-APE simulation of a jet, which clearly showed which source term that caused the sound generation and the result proved to be better than that computed with a FW-H integral method.

3.6. Turbocharger Acoustics

3.6.1. *Passive Properties*

The turbocharger damps incoming acoustic pulsations that are generated at the engine cylinders, which are the main noise source in an IC engine. The pulsations are damped both by reflection and absorption of acoustic energy. The direction of propagation of engine pulses is upstream for the compressor and downstream for the turbine. This means that for a compressor the upstream transmission loss (or upstream reflection and up- to downstream transmission) is the most interesting in a practical sense. The downstream TL is however interesting from an academical point of view. For the turbine it is the other way around, i.e. the downstream transmission loss is the most interesting. A number of experimental studies concerning the passive properties of the turbocharger have been performed and can be found in the literature. The most complete and accurate measurements are the recent studies by Rämmal & Åbom (2009) and Tiikoja *et al.* (2010).

Earlier the response of the compressor to engine pulsations has been experimentally investigated by Serrano *et al.* (2006). Four different turbochargers were tested and the measurements were performed on a test rig with a four-cylinder Diesel engine. Measurements were performed at several operating points for each compressor. However, since the turbocharger was integrated with an engine only the effect at the engine firing frequency was studied and this frequency changes with the engine operating point. Furthermore, since only one test case per operating point was possible, it was assumed that the reflection upstream of the compressor was negligible, i.e. that there were no

incoming waves from the upstream side. The fact that both the reflection and transmission coefficients are lower than unity is then used as an indication that this assumption is reasonable.

The results of Serrano *et al.* (2006) showed that the transmission coefficient decreases with mass flow. However the strength of this effect varied with compressor and for some compressors with the rotational speed. Studying the compressor maps it was concluded that the decreasing transmission with increasing mass flow is due to an increase in the inclination of the map speed lines. That is, in regions of flat speed lines the transmission is fairly independent of mass flow, but when the inclination increases the transmission decreases. It is further observed that the transmission is inversely scaled with the compressor volume. The reflection coefficient seems independent of both mass flow and rotational speed. Some variations are observed, but they seem erratic. As for the transmission the reflection is much lower for the larger compressor.

An experimental study of the passive properties of the turbine has been performed by Peat *et al.* (2006). They performed measurements on an impulse test rig for three rotational speeds of the turbine. The speeds were 0, 28000 and 56000 rpm, where the highest is about a third of the turbine speed at practical operating conditions. The results showed that the turbine has a non-symmetric effect on incoming waves. The transmission coefficient shows similar frequency dependence in both directions, with peaks at roughly the same frequencies, but the magnitude is much higher for upstream propagating waves. For the reflection coefficient both the magnitude and the frequency variation depend strongly on the propagation direction. Studying the influence of the rotational speed a dependency can be observed for very low frequencies, while it seems to have a minimal effect at higher frequencies for the investigated speeds. For the low frequencies the transmission decrease with increasing rotational speed, while the reflection increase for downstream propagating waves and seems unaffected for upstream propagating waves.

In the more resent and complete studies, Rämmal & Åbom (2009) investigated the passive properties of the compressor and Tiikoja *et al.* (2010) investigated the passive properties of both the compressor and the turbine. The investigations were performed with different turbochargers in the acoustic turbocharger test-rig at the CICERO center, KTH. A steady flow was provided and loudspeakers were used to excite incoming waves with frequencies up to 1600 Hz. The measurements were performed at several realistic operating points of the turbocharger.

The results of both Rämmal & Åbom (2009) and Tiikoja *et al.* (2010) showed a strong non-symmetric effect for the compressor, with lower transmission loss (TL) in the downstream direction. For low frequencies (up to around 500 Hz) the compressors were almost transparent (TL < 5 dB) in the downstream direction, while for higher frequencies the TL started to increase.

The downstream TL was further observed to be almost independent of operating point, with the exception of higher frequencies (above 1100 Hz) in the measurements by Rämmal & Åbom (2009). In the upstream direction the TL was significantly influenced by the operating point and both Rämmal & Åbom (2009) and Tiikoja et al. (2010) concluded that the mass flow had the strongest effect on the TL, where a higher mass-flow resulted in a higher transmission loss. This is the same phenomena as observed by Serrano et al. (2006), where the transmission decreased with mass flow. Furthermore, Rämmal & Åbom (2009) reported that the TL tends to increase when the pressure ratio is increased for a constant mass flow, an effect that is more clearly seen for the upstream direction. At higher frequencies (above 800 Hz) both Rämmal & Åbom (2009) and Tiikoja et al. (2010) found distinct peaks in the upstream TL. The source of these peaks has still not been found and their characteristics were different in the two measurements. Rämmal & Åbom (2009) mainly found peaks for the low mass flow operating points and there were often two peaks in the spectra. The frequency at which the first peak occurred tended to be at lower frequencies for higher mass flows, while the pressure ratio seemed to have a significant influence on the peak levels. The measurements by Tiikoja et al. (2010) showed one peak in the TL, which like in the measurements by Rämmal & Åbom (2009), was at a lower frequency for higher mass flows. However, in the measurements by Tiikoja et al. (2010) the peaks seemed to be significantly stronger for operating points close to the choke line.

Tiikoja et al. (2010) also performed measurements of the transmission loss of the turbine, where the inlet temperature was limited to around 100°C. As for the compressor, the upstream TL was dependent on the mass flow, while the downstream TL was almost independent of operating point. The level of the downstream TL was however significantly higher for the turbine than for the compressor and no peaks were found in the upstream transmission loss (for the studied frequencies), except for in the no flow case.

3.6.2. *Compressor Sound Generation*

Not much research has been performed within the field of centrifugal compressor acoustics and much of the theory and ideas of the sound generating mechanisms come from the study of axial machines, which is much more comprehensive. In their overview of turbocharger acoustics Rämmal & Åbom (2007) include a summary of the aerodynamic sound generating mechanisms in rotating machines. Raitor & Neise (2008) have performed an experimental study of the dominating sound generating mechanisms in larger centrifugal compressors (with an impeller leading edge diameter of 156 mm) and the radiated sound field up- and downstream of the compressor. An example of the sound spectra at the compressor inlet can be seen in Figure 3.2 for different rotational speeds. However, to the author's knowledge no study has been performed with the smaller type of centrifugal compressors that are used in cars or trucks.
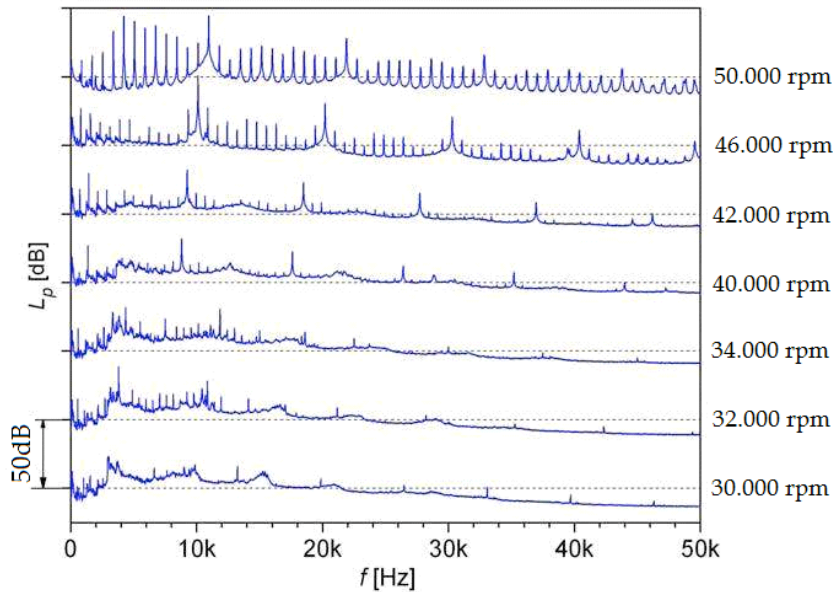
FIGURE 3.2. Pressure spectra of sound radiated in the upstream direction from a centrifugal compressor. Reprinted from Raitor & Neise (2008), with permission from Elsevier.

The aerodynamic sources in a rotating fluid machine have different strengths and importance depending on the operating point. Different source mechanisms will further excite specific acoustic modes, so the radiated sound will not only depend on the source strength, but also on the cut on frequencies of the up- and downstream ducts. In general it can be said that the generation of turbulent noise is very weak compared to other sound sources. Furthermore, the blade pressure is an important sound generating mechanism and there are several flow phenomena that can contribute to this and act as sound sources. A summary of the sound generating mechanisms in a turbocharger compressor is listed below, where the different contributions to the noise spectra can be seen in Figure 3.2. This is followed by a discussion of the different mechanisms. The discussion is mainly based on the summary of Rämmal & Åbom (2007) and the experimental results of Raitor & Neise (2008).

- Buzz-saw noise is seen as harmonics of the rotation frequency for supersonic rotor speeds.
    - At supersonic rotor speeds there are steady, in the rotor frame of reference, shock waves attached to the blades and they generate the buzz-saw noise.

- The pressure signature of the shocks propagates upstream and buzz-saw noise is therefore mainly seen at the upstream side.
- Close to the rotor most energy is in the blade passing frequency harmonics, but as the high amplitude sawtooth shaped wave propagates upstream energy is redistributed between the harmonics and dissipated by non-linear effects. So further upstream the energy is more evenly spread between the rotor harmonics.

- Blade passing frequency tones and their harmonics (BPF) can be seen for most rotational speeds and they increase in amplitude with the rotational speed.
  - A non-uniform stationary inflow will give rise to these tones at all speeds. Due to the experimental set up of Raitor & Neise (2008), with a straight inlet duct, the inflow is however expected to be quiet uniform, which could explain the low amplitudes for low rotor speeds in Figure 3.2.
  - The rotation of the rotor steady pressure field will generate BPF tones (mainly at the upstream side). It is however cut off at subsonic rotor speeds and will therefore only radiate noise at supersonic rotor speeds. At these speeds the rotor locked flow field will consist of shock waves attached to the blades in addition to the steady blade pressures. The relative effect of these sources has not been shown, but the author assumes that the former, which generates the so called buzz-saw noise described above, is the stronger source, since the measurements in Figure 3.2 are performed rather close to the rotor and the latter is assumed to be week.
  - Rotor-stator interaction generates BPF tones at all rotor speeds. This is however only important for compressors with vaned diffusers and on the outlet side.

- Tip clearance noise (TCN) is a broadband noise that is most important at low flow rates and not to high (subsonic) rotational speeds.
  - The generation is due to the interaction between blade tip vortices and the subsequent blades.
  - The strength increases with increasing tip clearance.

- Rotating instability (RI) is a flow phenomenon that generates a narrow band with larger amplitude in the noise spectra below blade passing frequency.
  - The rotating instability is only observed at low flow rates and it is debated whether it really is a rotating stall, known from axial machines, that is observed.
  - It appears at the blade tips and can therefore also be called tip clearance noise.

- – The sound generation is due to the interaction between the rotating instability, which rotates relative to the rotor in the blade tip region, and the rotor blades.
- – The generated sound is radiated in both the up- and downstream directions. However if the compressor has a vaned diffuser it is efficiently damped in the downstream direction.
- Surge noise appears at very low mass flow rates when the compressor operation becomes unstable and the flow is governed by high amplitude pulsations.

Buzz-Saw Noise

Turbochargers rotate at very speeds and it is common with supersonic blade tip speeds. At these high rotational speeds there will be shock waves attached to the blades and they generate noise at harmonics of the rotation frequency. This noise, which normally is referred to as buzz-saw noise, became a problem in the 1970's when the modern high-bypass-ratio turbofan engines, which can operate at supersonic blade tip speeds, were developed.

Buzz-saw tones can, at high rotational speeds, be observed in Figure 3.2. As expected the buzz-saw tones start to appear when the leading edge tip diameter becomes supersonic (around 41.000 rpm) and the level of the tones increase with impeller speed. Due to the mechanism for generating buzz-saw noise, which will be described below, noise is only efficiently radiated in the upstream direction. The downstream noise measurements by Raitor & Neise (2008) showed that buzz-saw tones also are present at the downstream side for very high speeds, but only below blade passing frequency and with substantially lower levels.

McAlpine & Fisher (2001) and McAlpine *et al.* (2006) have performed investigations of the buzz-saw noise radiation from an axial fan. This included an extensive description of the sound generating and radiating mechanisms, which will be summarized below.

The principal source of buzz-saw noise is the rotor alone pressure field, which is steady in the rotor frame of reference. At supersonic tip speeds this pressure field is dominated by shock and expansion waves that extend upstream of the fan. The shocks are located at or close to the leading edge of the blades, while the expansion waves are attached to the blades, see Figure 3.3 for a two-dimensional model.

Shortly upstream of the blades, in the shock normal direction, the pressure signature resembles a sawtooth (or N-wave). In the case of an ideal fan, i.e. identical blades in a uniform flow, the sawtooth waveform will be regular. This means that the frequency spectra will consist of harmonics of the blade passing frequency. Further assuming weak shocks, all shocks propagate upstream at the undisturbed speed of sound relative to the incoming fluid, so the regular
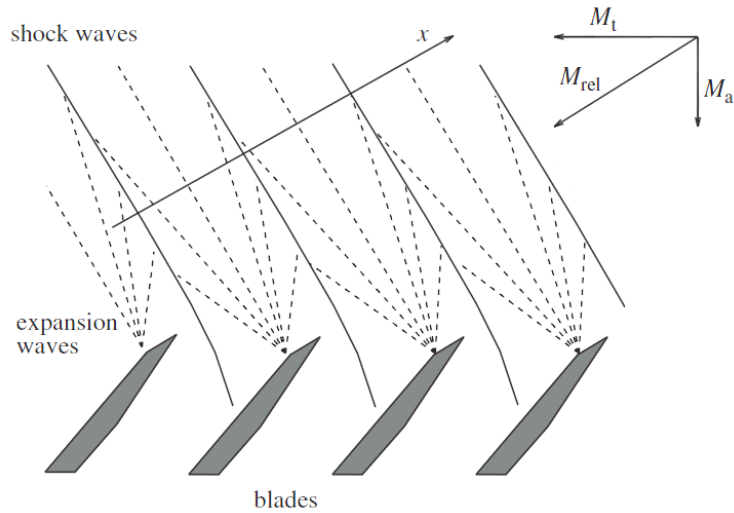
FIGURE 3.3. Shock and expansion waves attached to fan blades at supersonic blade tip speeds. Reprinted from McAlpine & Fisher (2001), with permission from Elsevier.

sawtooth shape is conserved and the radiated noise will consist of harmonics of the blade passing frequency. In reality no fan is perfect and there will be deviations in the shape of and distance between the blades. This results in an irregular sawtooth pressure signature, with features that repeat themselves only ones per fan revolution. Harmonics of the rotation frequency are then excited, even though the blade passing frequency harmonics are stronger. However, the shocks will propagate upstream at slightly different speeds and as the sawtooth propagate upstream along its helical path the blade to blade periodicity in the shape will be less pronounced. This gives a reduction in the amplitude of the blade passing frequency harmonics. At the same time non-linear effects will redistribute energy between the harmonics and attenuate the high amplitude sawtooth pressure wave, mainly at higher harmonics. An example of how an irregular sawtooth pressure wave is affected by the described mechanisms as it propagates a distance upstream in a duct can be seen in Figure 3.4.

The rotor alone pressure field can be described as a superposition of spinning duct modes, which will be steady in the rotor frame of reference. According to McAlpine & Fisher (2001) this results in modes that have a dependent frequency (f) and azimuthal (m) wavenumber, where for each rotational frequency harmonic the azimuthal wavenumber is equal to the order of the harmonic. McAlpine & Fisher (2001) further states that the radial modes of order ≥ 2 usually are cut-off at the operating points of an aero-engine fan and for
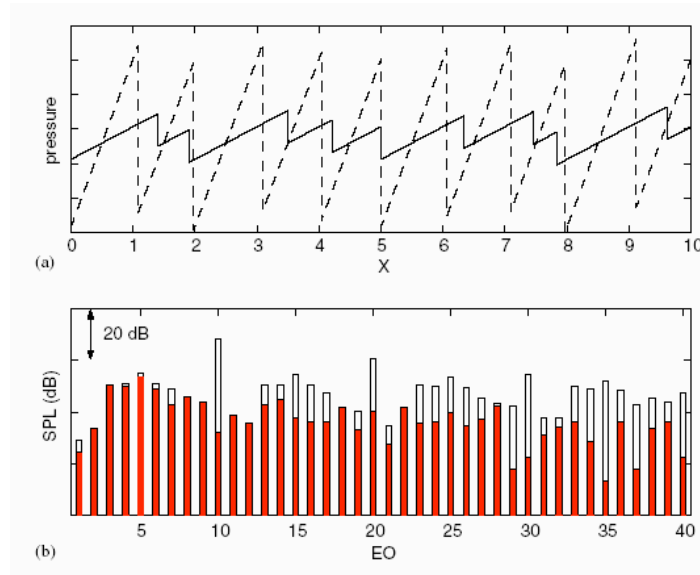
FIGURE 3.4. Example of a buzz-saw noise signature.   a) dashed line: pressure waveform close to fan, solid line: pressure waveform at the end of the inlet duct. b) Energy distribution among rotation harmonics (EO) close to the fan (white bars) and at the end of the inlet duct (red bars), for a ten bladed fan. Reprinted from McAlpine *et al.* (2006), with permission from Elsevier.

the low order harmonics the first radial mode is also frequently cut-off. It is therefore assumed that the radial modes can be neglected when buzz-saw noise is studied.

Raitor & Neise (2008) studied the azimuthal mode decomposition of the buzz-saw harmonics four, five and six and found that it agreed well with the above theory of mode - harmonic order dependence. They also found that for the 50 000 rpm case the first four harmonics consist of modes that are below the cut on frequency of the inlet duct, which can explain why the fifth harmonic is the strongest, see Figure 3.2. This is even more apparent when the pressure is measured further upstream in the duct.

It should be noted that when the rpm increases there will be supersonic speeds over larger parts of the blade span, which is anticipated to give significant three-dimensional effects, making the above 2D description of the rotor alone pressure field less realistic. Furthermore, there can be cut-on of the first radial modes at very high speeds.

Blade Passing Frequency Tones

There are several phenomena in a rotating fluid machine that can generate noise at the blade passing frequency and its harmonics. Except for the buzz-saw tones described above, all these phenomena have in common that they generate sound by influencing surface forces. The blade passing frequency (BPF) is defined as the rotation frequency times the number of rotor blades.

The rotation of the, in the rotor coordinate system, steady blade pressure field will give rise to a so called Gutin noise, which also is referred to as rotor alone tonal noise. This noise is most important for high rotational speeds and steady uniform inflows. It can however be difficult to distinguish this source from the buzz-saw noise. In applications there are normally inflow disturbances and this is the most important contribution to time varying blade pressures. When the blades rotate with high velocity through a non-uniform stationary flow field they will experience strong periodic pressure fluctuations and a tonal noise at harmonics of the blade passing frequency is generated. Another mechanism that generates BPF noise is rotor stator interactions.

Tyler & Sofrin (1962) developed a famous relationship for the acoustic azimuthal mode orders generated by rotor stator interaction:

$$m_{R\&S} = nZ - sV \qquad (3.29)$$

where Z and V are the number of rotor and stator blades, n is the order of the blade passing frequency harmonic and $s = ..., -2, -1, 0, 1, 2, ...$. In the case of a vaneless diffuser it is possible to set $V = 0$ and the above equation gives the modes generated by the rotor steady pressure field: $m_R = nZ$. This is the same azimuthal modes as the ones predicted to be radiated as buzz-saw noise at the same frequencies for supersonic blade tip speeds, which intuitively also should be the case since both sources are due to rotation of the rotor locked pressure field.

Tyler & Sofrin (1962) further studied the cut on of the modes generated by the rotor alone pressure field. They came to the conclusion that the BPF harmonics were cut on first at certain blade tip Mach numbers, which always are above one, but decrease with increasing number of blades and harmonic order. This means that for subsonic rotor speeds the rotor alone pressure field is cut off and decays exponentially as it propagates away from the rotor. However, in the case of sound generation by interaction between the blades and a non-uniform inflow other modes will also be generated, as stated by McAlpine *et al.* (2006), and they might be cut on and radiate BPF noise also at subsonic rotor speeds.

Raitor & Neise (2008) used the above theory together with measurements up- and downstream of three compressors, one with a vaned and two with vaneless diffusers, to estimate the contribution of the different sources to the radiated tones. Here it should be noted that the measurements were performed

on a test bench with a straight inlet duct, where non-uniform stationary inflow disturbances should be small. In reality turbochargers are mounted in duct systems, where other components (e.g. pipe bends) cause a non-uniform inflow. This is expected to increase the level of the blade passing frequency tones.

By decomposing the upstream blade passing frequency tones into their azimuthal mode spectra Raitor & Neise (2008) observed that for high rotational speeds the dominating mode was predicted by Equation 3.29 without guide vanes, both for the case of a vaned and a vaneless diffuser. For lower speeds the modes predicted by Equation (3.29) without guide vanes are cut off and the measurements of Raitor & Neise (2008) indicate that most of the energy is in the lower order modes that are not cut off. This implies that for high speeds the upstream radiated tones are mainly generated by the rotor locked pressure field and not by interference between the rotor and the surrounding flow field or rotor-stator interaction. However, it cannot be concluded how much of the rotor alone tonal noise that is buzz-saw noise, i.e. that is generated by the rotating shock waves that are attached to the blades at these speeds, especially since the measurements are performed close to the rotor where the BPF component of the buzz-saw noise still might be the strongest, as described above. For lower, subsonic rotor speeds the main noise source should be the interaction of the rotating blades with non-uniform stationary inflow disturbances, since the dominating mode generated by the rotor-locked pressure field is cut off.

The measurements by Raitor & Neise (2008) showed that adding guide vanes to the diffuser significantly increased the level of the downstream tones, especially at lower rotational speeds where they became stronger than at the upstream side. This implies that the rotor-stator interaction noise mainly propagates in the downstream direction and it is generated by interaction between the rotor and the guide vanes in the stator, so it is less important for compressors with vaneless diffusers. Furthermore, it was observed that adding guide vanes to the diffuser raised the overall sound pressure level with about 3.5 dB on average.

Tip Clearance Noise

Tip clearance noise refers to the sound produced by the unsteady flow around the blade tips. It can give a significant contribution to the broadband noise level, but can also give a drastic increase of the radiated sound within almost narrow frequency bands. The tip clearance flow is driven by the pressure difference between the pressure and suction sides of the blade. An important feature of this flow is a vortex that is formed at the tip of each blade and then is convected downstream with the mean flow.

If the blade tip vortex interacts with the subsequent blade a broadband noise is generated. To investigate this phenomenon Fukano & Jang (2004) performed hot wire measurements, using a rotating hot-wire, of the relative

velocity and velocity fluctuations close to the blade tips of an axial fan. They observed that for high flow rates the tip vortex was convected downstream without interfering with the next blade, but as the flow rate was decreased the vortex was convected in a more circumferential direction. When the flow rate had become significantly lower than the design flow rate the blade tip vortex started interfering with the next blade, giving significantly increased broadband noise levels. Decreasing the flow rate further resulted in larger movements of the tip vortex and thereby a further increase of the broadband noise level.

Fukano & Jang (2004) also studied the influence of tip clearance on the sound generation and the tip vortex. They came to the conclusion that increasing the tip clearance result in increased broadband noise levels, due to the generation of a larger vortical flow with higher velocity fluctuation levels. This increase of the broadband noise level with increased tip clearance is in good agreement with other studies, see e.g. Kameier & Neise (1997).

Rotating Instability Noise

At lower mass flows an almost narrow band hump can be observed in the noise frequency spectra below blade passing frequency. This hump is for low rotational speeds clearly visible in Figure 3.2, of the centrifugal compressor noise measurements by Raitor & Neise (2008). The source of this noise is believed to be a flow phenomena termed rotating instability (RI), which is thought to be present at the blade tips under these operating conditions. Since the source comes from a phenomena present at the blade tips this noise has been called tip clearance noise, but to avoid confusion it has here been chosen to call it rotating instability noise.

It should be noted we use the term rotating instability (RI) even though the phenomenon is quite similar to that of rotating stall (RS), which is a known flow effect occurring at low flow rates in axial compressors, see the discussion by Cumpsty of the paper by Mailach *et al.* (2001). The reason for using the term RI is that it is assumed to differ from RS in the way that the latter is a steady flow field within its own frame of reference, while the RI is an unsteady rotating source mechanism, as indicated by measurements in axial machines by e.g. Kameier & Neise (1997) and Mailach *et al.* (2001). Furthermore, Kameier & Neise (1997) claim to have observed both RI and RS in the same measurement, where the latter appeared as discrete very low frequency tones when the flow rate was decreased to very low levels and the fan operation became unstable. However, the low frequency peak in the spectra at an unsteady operating point could also indicate surge.

Kameier & Neise (1997) studied the appearance of this narrow band noise increase in an axial compressor. They found that it is always accompanied by an almost narrow band amplitude increase in the blade and casing wall pressure spectra close to the blade tips. This amplitude increase is mainly seen
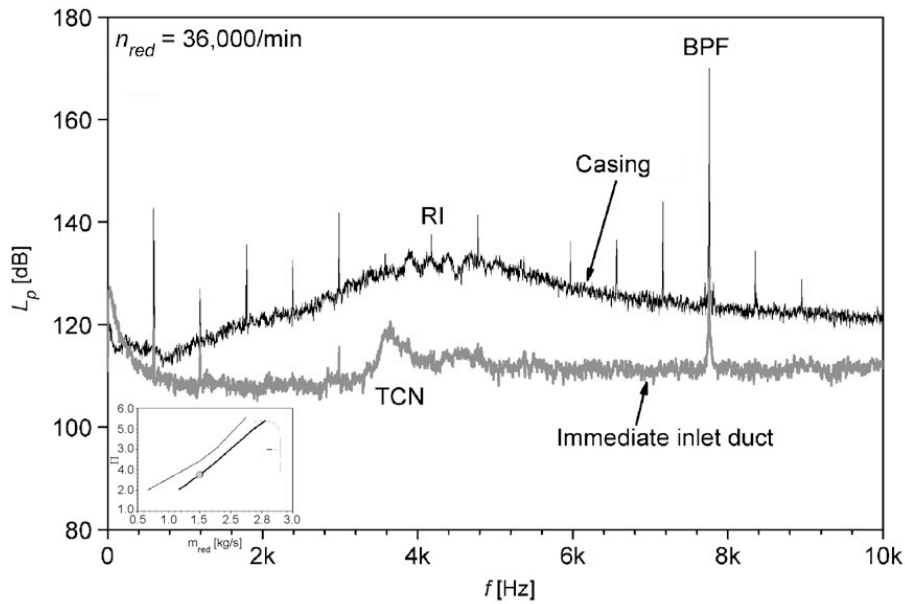
FIGURE 3.5. Pressure spectra at the casing wall showing rotating instability (RI) and the corresponding noise spectra in the inlet duct showing the generated tip clearance noise (TCN). Reprinted from Raitor & Neise (2008), with permission from Elsevier.

below blade passing frequency and often has superimposed peaks of constant frequency spacing, see Figure 3.5. This effect was ascribed to the phenomena of rotating instability. Just as the broadband tip clearance noise this phenomena is strongly dependent on tip clearance and flow rate. Kameier & Neise (1997) could only observe rotating instability in axial compressors for large tip clearances and lower flow rates. This effect was also seen by Mailach *et al.* (2001), who studied the effect of the tip vortex on rotating instability.

From their measurements of the pressure spectra at the casing wall and the blades Kameier & Neise (1997) came to the conclusion that the rotating instability can be interpreted as an unsteady source or vortex mechanism which rotates relative to the rotor at about half the impeller speed and interacts with the blades, thus generating narrow band noise. Kameier & Neise (1997) further concluded that rotating instability only occurs in combination with reversed flow conditions in the tip clearance gap and they came with the following explanation. When the flow rate is low enough the reversed flow can become strong enough to eliminate the axial component of the main flow near the blade tips. The oncoming flow as seen by the blade tip then only has an azimuthal

component. As a result the tip vortex move in the circumferential direction and if the wavelength of the shed vortex matches the blade spacing a strong interaction between the vortex separation on individual blades occur, resulting in a drastic increased noise radiation.

Mailach *et al.* (2001) studied the generation of rotating instability, using unsteady pressure measurements and 2D-LDA measurements in the blade tip region of the third stage of a four stage axial compressor, and they presented a similar explanation to that of Kameier & Neise (1997). At large tip clearances and low flow rates a strong blade tip vortex is formed at leading edge of blade 1. This vortex has a large reversed flow field that affects the flow in the front region of blade 2, moving the vortex generation at that blade further down on the blade, resulting in a much weaker vortex that does not influence blade 3. A new strong vortex, interfering with blade 4, is then formed at blade 3. This way the fluctuating blade tip vortices propagate around the rotor against the rotor turning direction at just over half the rotor velocity.

The circumferential distribution of this rotating instability source is not uniform and can be represented by a superposition of spatial Fourier components similar to the higher order azimuthal (acoustic) modes in circular ducts. Mailach *et al.* (2001) states that dominating mode orders of RI of about 1/3 up to the twice the number of rotor blades have been observed. This gives a circumferential wavelength of the disturbance of about 0.5 to 3 times the rotor blade pitch. In their own measurements Mailach *et al.* (2001) found the dominating mode order to be almost half of the number of blades (63), while Kameier & Neise (1997) found the dominating mode order to be approximately equal to the number of blades (24) in their experiment. This difference in the wavelength of the disturbance found can also be seen in their descriptions of the rotating instability phenomena summarized above.

Kameier & Neise (1997) assumes that the interaction of the rotating instability with the blade cascade is similar to the interaction between two rotors. The mode numbers and angular frequencies generated by two rotors of different angular speed and number of blades can be determined from the theory proposed by Holste & Neise (1997). This theory is based on the formula of Tyler & Sofrin (1962) for the interaction of a stator and a rotor, see Equation (3.29), and on introducing a coordinate system rotating with the second rotor. The azimuthal modes and frequencies generated are:

$$
\begin{aligned}
m &= h_1 B_1 - h_2 B_2 \\
\omega &= h_1 B_1 \Omega_1 - h_2 B_2 \Omega_2
\end{aligned}
\qquad h_1, h_2 = ..., -1, 0, 1, ..., \qquad (3.30)
$$

where the subscripts 1 and 2 stands for the two rotors, B is the number of blades, Ω is the rotor angular speeds and h is the harmonic number. Counter rotation is accounted for by opposite sign of the two speeds.

When the theory is applied to the interaction of the rotating instability with the rotor B is interpreted as the dominating azimuthal mode order α_{RI} of the rotating instability and Ω is the angular speed of the rotating instability in a fixed coordinate system. This result in the following equations for the generated modes and frequencies, where the subscripts have been changed to R for rotor and RI for rotating instability:

$$
\begin{aligned}
m &= h_R B - h_{RI}\alpha_{RI} \\
\omega &= h_R B \Omega_R - h_{RI}\alpha_{RI}\Omega_{RI}
\end{aligned}
\qquad h_R, h_{RI} = ..., -1, 0, 1, ..., \qquad (3.31)
$$

In the above equation it is possible to identify the following relations: $B\Omega_R = \omega_{BPF}$ and $\alpha_{RI}\Omega_{RI} = \omega_{RI}$, which gives the following estimation of the generated frequency by the interaction of the first harmonics ($h_R = h_{RI} = 1$):

$$
f_{TCN} = f_{BPF} - f_{RI} \qquad (3.32)
$$

Where all frequencies are with respect to a fixed coordinate system. It should be noted that studying the rotating instability spectra, each peak superimposed on the narrow band amplitude increase can be identified as a mode order α_{RI} and the spacing between the peaks then is the angular speed of the rotating instability (Ω_{RI}).

Kameier & Neise (1997) and Raitor & Neise (2008) compared their results from the measurements on an axial respectively centrifugal compressor with the above theory. The generated noise and the pressure fluctuations close to the blade tips matched the theory above in terms of the frequency relation, Equation (3.32), the generated mode orders and the angular velocity of the rotating instability. Due to this agreement with theory they came to the conclusion that the narrow band noise observed really is due to a rotating instability.

Raitor & Neise (2008) further studied the radiation of RI noise in the up- and downstream direction. They came to the conclusion that it is radiated in both directions, but if the compressor has a vaned diffuser it becomes very low at the outlet side.

Surge

As the mass flow is reduced to low levels the flow becomes unstable and the compressor goes into surge. The phenomena of surge is explained in Section 2.2.1 above. At such operating points the flow is dominated by very high pulsations at low frequency and it can be observed as strong peaks in the sound spectra far below the rotation frequency.

Broadband Noise

A non-stationary (turbulent) inflow will result in more random blade pressure
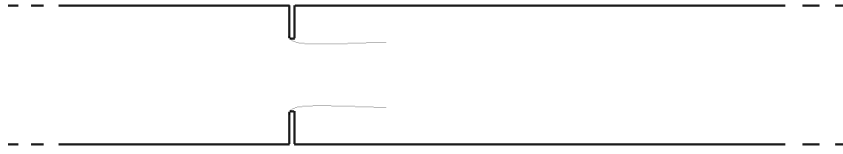
FIGURE 3.6. A ducted orifice plate, where the grey lines show the vena-contracta effect.

variations and thereby a broadband noise. The unsteady flow, which can consist of vortices, flow separations and turbulence, can also contribute to the broadband noise level. An example of this is the broadband tip clearance noise which increases with tip clearance and decreased flow rate as described above.

Raitor & Neise (2008) further observes that the broadband noise level decreases faster with frequency in the outlet duct, an effect that starts after the first BPF. However for the highest rpm the outlet broadband noise level is still higher until 28 kHz.

3.7. Acoustics of a Ducted Orifice Plate

The geometry studied is an induct plate with a circular orifice at the centre, see Figure 3.6. When there is flow through the duct an unsteady jet is formed downstream of the plate and there is vortex shedding from the orifice edges. The smallest diameter of the jet (vena contracta) is smaller than that of the orifice, which is referred to as the vena-contracta effect, shown in Figure 3.6. The origin of this effect is flow separation at the leading edge of the orifice plate and the strength of it will therefore depend on the shape of the orifice, e.g. how sharp the edges are, where sharper edges give a stronger effect.

3.7.1. *Passive Properties*

When an acoustic wave impinges on an orifice plate it is partly reflected and partly transmitted through the orifice. At the same time some of the acoustic energy is absorbed as it is converted to vorticity, which is created at the orifice edges due to the acoustic fluctuations. In the linear no-flow case there are only small amounts of vorticity created and this vorticity will stay in a thin boundary layer next to the plate inside the orifice. When the acoustic amplitude is increased and the problem becomes non-linear the absorption of acoustic energy increases, as subsequent vortex shedding starts to appear at the orifice edges. The shed vortices are then transported away from the orifice with the acoustic velocity before they are dissipated. For more information about the acoustic non-linearities of orifices, see e.g Ingard & Ising (1967). When flow is introduced in the duct the generated vorticity will be convected downstream with the flow and acoustically induced vortex shedding can be observed at the upstream edge also in the linear case.

To improve the understanding of the effect induct orifices have on incoming sound waves Leung *et al.* (2005) performed a 2D DNS study of the non-linear no flow case. By studying a single frequency they found the following cycle for the interaction between the sound wave and the orifice plate: At time zero a local upstream flow is created in the orifice and it generates a puff of vorticity at the upstream side of the orifice lip. At time $T/4$ (where T is one period of the wave) the vorticity puff takes its maximum strength. At time $T/2$ the flow through the orifice changes direction, the puff is completely shed as a vortex and a new puff is generated at the downstream side. A shed vortex is only convected a short distance before it is dissipated. Due to this the pressure field is only affected by the vortex shedding in the vicinity of the orifice. The vorticity production becomes weaker with higher frequencies. Larger orifice sizes also give weaker vorticity production, since the local velocity fluctuations are smaller.

The amplitude at which the scattering becomes non-linear depends on the mean flow rate. In general significant non-linear effects are said to appear when the amplitude of the acoustic velocity fluctuations is around 10 % of the mean velocity. Testud *et al.* (2009) e.g. reported seeing non-linear effects when the root mean square of the acoustic velocity fluctuations exceeded 10 % of the mean velocity (during measurements at low Mach numbers).

The effect of flow and acoustic amplitude on the reflection by an induct (6 mm thick) orifice plate has been studied experimentally by Rupp *et al.* (2010) for one frequency. Their results showed that the amplitude where the absorption process became non-linear increased significantly when flow was introduced and then increased successively as the flow rate was increased. The reflection also increased as the flow rate was increased. However, the results with flow showed no trend of approaching the no-flow characteristics as the flow rate was decreased. This could be due to the flow rate not being reduced enough for the flow to be laminar through the orifice, which would be required to get a uniform transition when flow is introduced.

Rupp *et al.* (2010) also performed a visualization of the acoustic part of the flow for a non-linear no-flow case and a linear case with flow. The visualization consisted of a Proper Orthogonal Decomposition (POD) of PIV measurements. The POD modes containing most of the energy at the excitation frequency were put together to represent the acoustic part of the field. The result for the non-linear, no-flow case showed the same phenomena as observed by Leung *et al.* (2005) in their 2D DNS. A vortex ring was generated at the orifice at the start of each period and it was then convected away from the plate by the acoustically induced velocity. For the linear case with flow vorticity production could still be observed at the initial part of the acoustic period, but no convected vortex structures could be observed. This result was interpreted as a confirmation that linear absorption is characterized by a cylindrical vorticity layer surrounding the aperture.

In the plane wave frequency range quasi-steady models have been proposed for the passive acoustic properties of thin ducted orifice plates. Here two models will be described, where the scattering is related to the Mach number and the vena-contracta coefficient, i.e. the jet area over the orifice area. The models have been presented in combination with measurements in Allam & Åbom (2005) and Durrieu *et al.* (2001).

Allam & Åbom (2005) suggests a model for low Mach numbers that is based on incompressible theory. Only the real part of the scattering matrix is considered and it becomes a frequency independent function of the inlet Mach number (M) and the pressure loss coefficient ($C_L = \Delta p/(\frac{1}{2}\rho U^2)$), where Δp is the pressure drop over the plate and ρ and U are the inlet density respectively velocity):

$$\mathbf{S} = \frac{1}{2 + MC_L} \begin{pmatrix} MC_L & 2 \\ 2 & MC_L \end{pmatrix} \tag{3.33}$$

The pressure loss coefficient can be found in handbooks for different geometries, but in this case it is related to the vena-contracta coefficient, which is assumed to be independent of Mach number. Equation 3.33 shows that theoretically the scattering matrix is symmetric for low Mach numbers and that the reflection increases while the transmission decreases when the Mach number is increased. The result for the upstream reflection and the down- to upstream transmission at Mach numbers 0.036 and 0.055 and the upstream reflection and the up- to downstream transmission at Mach number 0.081 have been compared to measurements with good results for the lower frequencies.

The measurements performed by Allam & Åbom (2005) to validate the theory described above were done with a thin orifice plate (2 mm), with sharp edges and an area contraction ratio of 0.28. The measurements were performed for three inlet (mean) flow speeds, $M = 0.036$, $M = 0.055$ and $M = 0.081$. The results shown (which only were for the real part of the elements) were frequency independent up to at least 1500 Hz and showed the Mach number dependence expected from theory. The data from these measurements has been used to validate the simulations performed in this work.

Linear 2D simulations of the scattering have been performed by Kierkegaard *et al.* (2008), for the geometry used in the measurements by Allam & Åbom (2005), at the inlet Mach number of 0.055. The linearized Navier-Stokes equations were solved in the frequency domain assuming an isentropic relation between pressure and density and using a mean flow field from a DNS. The two-dimensionality was compensated for by setting the diameter of the orifice to match the area contraction ratio of the physical geometry. Furthermore, the Helmholtz number was normalized with the Helmholtz number of the duct cut on frequency for higher order modes. The result was compared to the measurements with good agreement.

When it comes to the Mach number dependent scattering by an orifice Durrieu *et al.* (2001) have presented a theory, in combination of measurements, for the low frequency response of circular and slit orifices. Just as in the theory by Allam & Åbom (2005) the scattering is frequency independent. The large difference is that the vena contracta is allowed to be a function of the jet Mach number. The theory, using either a Mach dependent or constant (Mach independent) vena-contracta coefficient, for the amplitude of the scattering at slits was compared to an incompressible theory and measurements for inlet Mach numbers up to 0.15. All theories produced good results for the low Mach numbers, but as the Mach number was increased first the incompressible theory and then the theory with a constant vena-contracta coefficient started to deviate from the measurements, which showed a strong dependence on Mach number. The inlet Mach number dependence, and thereby also the deviation between the theories, became stronger when the open area ratio was decreased, i.e. for narrower slits, due to the higher jet Mach number. The trend shown by changing the Mach number was however the same as for the low Mach number approximation by Allam & Åbom (2005), where an increased Mach number resulted in an increased reflection and a decreased transmission.

For thicker plates the theory will become more complicated, since the scattering can depend on frequency. For most frequencies and flow configurations there will be an absorption of sound by vorticity production as described above, but for some special cases (with flow) there can be a net increase in acoustic energy. The exact phenomenon behind this effect is not known, but the general idea is that the vortices generated by the acoustic wave are amplified by extracting energy from the mean flow and then interact with the plate further downstream, e.g. at the downstream edge, generating more acoustic energy than originally absorbed by the vorticity. The generated sound will automatically have the same frequency as the incoming sound, but for a net amplification of acoustic energy it has to interfere constructively with the incoming wave. Furthermore, whistling can occur if the frequency of the amplified wave corresponds to a resonance in the system so a feedback loop is generated, where the amplitude increases up to very high levels where it is damped by non-linear effects.

The whistling potential of the orifice plate is a linear phenomena that can be investigated by studying the instability frequencies, where there is a net amplification of acoustic energy. Since the amplification of acoustic energy is a linear phenomenon it is possible to simulate with linear methods, as shown by Kierkegaard *et al.* (2010). They used a linearized Navier-Stokes solver to simulate the whistling potential of a thick orifice, with good results compared to measurements by Testud *et al.* (2009).

The measurements of the instability frequencies performed by Testud *et al.* (2009) were done for 10 sharp edged orifice plates, with different thicknesses and area contraction ratios. The results showed that, for higher Reynolds

numbers (where the pipe flow is expected to be fully turbulent), there was a maximum whistling potential for Strouhal numbers around 0.2-0.3, based on the plate thickness and the orifice jet velocity. For lower Reynolds numbers, the Strouhal number for the instability frequencies was increased. The instability frequencies were also shown to have a dependence on the area contraction ratio of the orifice. Furthermore, for the thicker orifices two frequency regions with whistling potential were found.

Due to non-linear effects as the amplitude grows in the feedback loop, it is not obvious that the whistling frequency matches the instability frequencies found in the linear case. Furthermore, there must be reflections at the duct ends to obtain a feedback system. To investigate this Testud *et al.* (2009) performed measurements of the whistling and compared the result to theory based on the frequency instability regions and the reflections at the duct ends. The result showed that the theoretical frequency agrees with the actual whistling frequency within the measurement uncertainty, confirming the validity of the model. To achieve whistling the model then states that there must be significant reflections at the end of both the inlet and the outlet ducts.

3.7.2. *Sound Generation*

There are several mechanisms that can generate sound when the fluid flowing in a duct passes an orifice. Vortices shed from the orifice edges and the unsteady downstream separation act as dipole sound sources when they interact with the plate. The interaction between the unsteady jet and the duct wall will however not radiate any low frequency plane waves along the duct, since the force is orthogonal to the only possible propagation direction for the wave. The jet itself and the large fluctuations as the jet breaks down will on the other hand act as quadrupole sources, which can become significant at higher Mach numbers. When the jet Mach number exceeds unity there will also be shock waves present in the jet and they act as monopole sound sources.

Allam & Åbom (2005) measured the radiated sound as well as the scattering from the thin circular orifice mentioned above. The source spectra was measured for three inlet Mach numbers, the highest being 0.1. The spectrum was then scaled using a scaling law based on the assumption that the sound was generated by pressure fluctuations at the plate, which therefore could be seen as a compact dipole. The resulting scaled source spectra collapsed well for the different Mach numbers when it was plotted as a function of Strouhal number, implying that the dipole force at the plate was the main noise source. The results further showed that more noise was radiated in the downstream direction, which can be expected since most of the unsteady flow is at this side of the plate.

Kierkegaard & Efraimsson (2007) performed a 2D DNS on a thin ducted orifice plate with a peak Mach number of 0.1 and extracted the generated

sound. The result showed that the generated sound was broadband at Strouhal numbers above 0.1. However at lower frequencies there were large discrepancies in the result due to the large vortex structures in the flow field.

Gloerfelt & Lafon (2008) performed a LES to study the noise generated by low Mach number flow through a slit shaped diaphragm in a square duct. A broad peak was found in the noise spectra at Strouhal numbers 0.26 - 0.51. The peak was further found to be correlated to the coherent jet-column structures and their deformation and acceleration, leading to the conclusion that the main source mechanism was the breakdown of these structures before the jet reattached to the wall.

Under special conditions the flow through the orifice can generate a strong tonal noise. This noise is due to whistling, which also is mentioned at the end of the previous section. It is mainly important for thick plates, since the whistling frequency increases when the plate thickness decreases, leading to very high theoretical frequencies for thin plates. The whistling is believed to be generated by the flow and resonances in the system in the following way. When the air flows through the orifice vortices are shed at the upstream edge. These vortices interact with the plate further downstream, possibly at the downstream orifice edge, and an acoustic pulse is triggered. If this pulse is reflected at boundaries of the system so that it reaches the upstream edge in or close to in phase with the shedding of a new vortex the shedding is triggered and strengthened. This way a feedback mechanism with a periodic vortex shedding that triggers acoustic pulses, which feeds energy into a duct resonance, is established, resulting in a high tonal noise. The mechanism only occurs at certain flow speeds compared to the plate thickness, which as shown by Testud *et al.* (2009) is for Strouhal numbers around 0.25, see the discussion at the end of the Section 3.7.1.

CHAPTER 4

3D Models and Methods

In the work presented here Direct Noise Computations (DNC) have been performed. The reason for using DNC is that the aim of the project is to find methods appropriate for the acoustic analysis of turbochargers, where nonlinear effects can be an issue both for the generation and scattering of sound. Furthermore, the sound is assumed to be radiated into straight ducts, so the generated sound can be extracted fairly close to the source (if it has reached linear levels) and then be propagated analytically.

4.1. Governing Equations

The equations governing the flow, including the acoustics, are the compressible equations for conservation of mass, momentum and energy, also called the compressible Navier-Stokes equations, together with an equation of state. A derivation of the conservation equations on different forms can be found in e.g. Anderson (1995). In conservation form the equations are:

$$\frac{\partial \rho}{\partial t} + \frac{\partial (\rho v_i)}{\partial x_i} = 0 \tag{4.1}$$

$$\frac{\partial (\rho v_i)}{\partial t} + \frac{\partial (\rho v_i v_j)}{\partial x_j} = -\frac{\partial p}{\partial x_i} + \frac{\partial \sigma_{ij}}{\partial x_j} + f_i \tag{4.2}$$

$$\frac{\partial}{\partial t}[\rho(e + \tfrac{1}{2}v^2)] + \frac{\partial}{\partial x_i}[\rho v_i(e + \tfrac{1}{2}v^2)] = -\frac{\partial (pv_i)}{\partial x_i} + \frac{\partial (\sigma_{ij} v_j)}{\partial x_i} - \frac{\partial q_i}{\partial x_i} + f_i v_i \tag{4.3}$$

where ρ is the density, v_i is the velocity component in i-direction, e is the internal energy per unit mass, p is the static pressure, σ_{ij} is the viscous stress tensor, f_i is a possible external force field (per unit volume) acting on the fluid (e.g. gravity) and q_i is the heat flux.

In order to close the conservation equations an equation of state is needed. Assuming that air is an ideal gas, we use:

$$p = \rho RT \tag{4.4}$$

where R is the specific gas constant and T is the temperature. The air is further assumed to be calorically perfect, i.e. the temperature is low enough so that the vibrational and electronic modes of the molecules are not excited. The internal energy will then be proportional to the temperature and is related to the pressure, velocity and density through the following equation:

$$p = (\gamma - 1) \left(\rho e + \frac{\rho u^2}{6} \right) \tag{4.5}$$

where γ is the ratio of specific heats at constant pressure (c_p) and volume (c_v).

Air is also assumed to be a Newtonian fluid, which means that the stress due to fluid motion is assumed to be a linear function of the strain, i.e. the gradients of the flow state variables. The viscous stress tensor represents the stress due to fluid motion and is then given by

$$\sigma_{ij} = 2\mu(S_{ij} - \tfrac{1}{3} S_{kk} \delta_{ij}) \tag{4.6}$$

where μ is the dynamic viscosity, which is a function of temperature, and S_{ij} is the rate of strain tensor, defined as:

$$S_{ij} = \frac{1}{2} \left(\frac{\partial v_i}{\partial x_j} + \frac{\partial v_j}{\partial x_i} \right) \tag{4.7}$$

The heat flux is assumed to obey with Fourier's law:

$$q_i = -K \frac{\partial T}{\partial x_i} \tag{4.8}$$

where T is the temperature and K is the heat conductivity, which is a function of the temperature.

4.2. Turbulence

In contrast to laminar flows that are smooth and deterministic in character, turbulent flows are chaotic and random and hence can be characterized only by their stochastic properties. They are characterized by a mean and a fluctuating part. The transition from laminar to turbulent flow occurs when the inertial forces (non-linear in terms of velocity) in the flow become strong enough as compared to the viscous forces. This is described in terms of the Reynolds number (Re), which is the ratio of the inertial to the viscous forces:

$$\text{Re} = \frac{UL}{\nu} \tag{4.9}$$

where U is a characteristic velocity for the flow, L is a characteristic length scale for the problem and ν is the kinematic viscosity. In pipe flows laminar
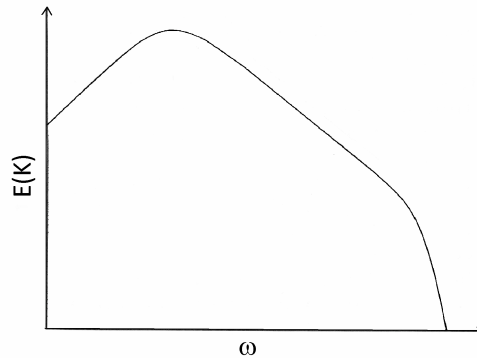
FIGURE 4.1. Turbulent kinetic energy spectra.

flow can be maintained up to Reynolds numbers of the order of a few thousands, depending on the experimental set-up (i.e. perturbation type and strength).

Turbulent flows contain a large number eddies of largely different sizes. The distribution of energy among the different scales of the turbulent fluctuations can be seen in the schematic plot, Figure 4.1. The large scale eddies contain most of the energy, which is supplied by the mean flow. The energy is then successively transferred to smaller and smaller eddies and eventually when the eddies become small enough they are dissipated to heat by viscosity. The characteristics and the size of the large scale eddies in the energy containing range are determined by the geometry and the particular (problem specific) flow field. The smallest scales in the dissipative range are universal and isotropic away from boundaries and their size scale as $\mathrm{Re}^{-3/4}L$ for high Reynolds numbers. In between the energy containing range and the dissipative range lies the inertial subrange, which contain intermediate sized eddies that are characterized by their inertia and the transfer of energy to successively smaller scales.

For deeper insight into the characteristics of turbulence and turbulent flows see a textbook like e.g. Pope.

4.2.1. *Turbulence Modeling*

The turbulent fluctuations are included if the equations governing the flow (Equation 4.1 to 4.3) are solved exactly with so called direct numerical simulation (DNS). To do this all scales of the turbulent flow have to be resolved and the computational effort increases as approximately Re^3. This means that as the Reynolds number is increased DNS becomes computationally very expensive and eventually impossible with the computer resources available today. The turbulence has therefore to be modelled.

The most commonly used turbulence models are Reynolds average Navier Stokes (RANS) models. In these models the flow variables are split into a mean and a fluctuating part. Inserting this decomposition into the governing equations leads to an equation for the mean variables that includes also terms (correlations of the fluctuating components) that cannot be explicitly expressed in terms of the mean variables. The average equations for the mean flow variables look similar to the basic governing equations, but with one additional term, the Reynolds stress tensor $\overline{u_i' u_j'}$, where u_i' is the velocity fluctuations. There is no analytical expression for the Reynolds stress tensor, so to solve the averaged equations for the mean quantities it has to be modelled. If the mean is computed as an ensemble average the mean flow may still be time dependent. However, the range of time-scales in such a case is much smaller than in fully turbulent flows.

Different RANS models have been suggested. The eddy viscosity models are the most simple and the most often used ones, especially in industrial applications. In these models the Reynolds stress is assumed to be proportional to the rate of strain (Equation 4.7) and a so called eddy viscosity ν_T. There exist several different methods for modelling the eddy viscosity, but they all have in common that they assume it to be isotropic and to only depend on the local flow field and they are calibrated against simple flow cases, like e.g. flow over a flat plate. The most well known and used eddy viscosity models are probably the Spalart-Allmara model, $k - \epsilon$ and $k - \omega$.

More complicated RANS models are the Reynolds stress models (RSM). In these models a transport equation is solved for the Reynolds stress tensor. This removes the assumption of the turbulence being isotropic and only dependent on the local flow variables, making the RSM models more general and better at capturing the effects of e.g. rotation, curvature and secondary motion. There are however still terms in the transport equation that need to be modelled and this is done using more or less realistic assumptions and calibration against simple flow cases.

RANS, especially the eddy viscosity models, is computationally very cheap, since the turbulent fluctuations do not have to be resolved and a coarse mesh can be used. The assumption that the turbulence is universal and that the dependence of the large scale fluctuations on the geometry can be neglected can however cause problems in more complicated flows. Furthermore, when acoustics is studied only low frequencies are resolved with RANS and the eddy viscosity models introduce extra viscosity that dissipate the acoustic waves.

When the geometry is more complex and RANS cannot capture the dynamics of the flow, Large Eddy Simulation (LES) is the main alternative. This model is computationally still much cheaper than DNS ($O(Re^2)$ instead of $O(Re^3)$), even though it is much more expensive than RANS. The idea of LES is that the large energy containing scales, which are coupled to the geometry,
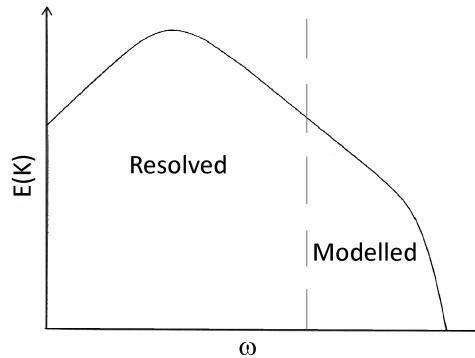
FIGURE 4.2. The turbulent kinetic energy spectra divided into
one resolved and one unresolved, modelled, part for LES.

are resolved in the simulation, while the small dissipative scales are modelled.
The turbulent kinetic energy spectra is then cut somewhere in the middle into
a resolved and an unresolved (modelled) part, see Figure 4.2.

In LES the Navier-Stokes Equations (4.1 - 4.3) are filtered with a spatial
low-pass filter, splitting the variables into a resolved and an unresolved part.
The filter length scale $(\overline{\Delta})$ is normally determined by the mesh and a common
expression is $\overline{\Delta} = V_{cell}^{1/3}$, where V_{cell} is the cell size. There are however other
formulations that can be more appropriate for less uniform grids and sometimes
the filter length scale is set to the size of a couple of cells in order to enable one
to better estimate the Sub-Grid-Scale (SGS) terms (as in the Scale Similarity
Model, SSM). Several types of explicit filters exist, but it is also common to
let the discretization scheme itself act as a low-pass filter. As the Navier-
Stokes equations are filtered additional terms are introduced in the equations.
In order to solve the filtered equations these so called SGS terms have to be
modelled. Since the small (unresolved) scales tend to be universal at high
Reynolds numbers it is easier to suggest appropriate SGS models than RANS
models.

An SGS model should account for the effects of the unresolved scales on the
resolved ones and for the most important physical properties of the unresolved
scales. The main effect at these scales is dissipation of kinetic energy at these
scales, which is one of the effects that one has to model. Instantaneously there
is also energy transfer from the smaller to the larger scales, a phenomenon
known as backscatter. This effect may be neglected if the spatial resolution
is fine enough (i.e. resolving a portion of the inertial subrange). Under such
conditions the separation of scales between the energy bearing eddies and the
unresolved scales is large enough to ensure small errors. A common way of

introducing the dissipation at the small scales is by introducing additional viscosity, for example as eddy viscosity in analogy to some RANS models:

$$\tau_{SGS} = -2\nu_t \overline{S} \tag{4.10}$$

where τ_{SGS} is the SGS stress tensor, ν_t is the eddy viscosity that can be modelled in different ways and $\overline{S}$ is the filtered rate of strain. In the compressible case the above expression is somewhat modified, but it is normally still only the eddy viscosity that is modelled and this is done as in the incompressible case. The downside of the eddy viscosity SGS models is that they can introduce too large dissipation, whereby the effective Reynolds number of the problem is reduced, as shown by Bogey & Bailly (2005). An alternative way of modelling the dissipative effect of the smallest scales is by filtering the solution, where e.g. an explicit filter is used to remove fluctuations with a length scale close to the cell size. This approach is used less often and mostly coupled with some explicit model (e.g. SSM).

The Smagorinsky model is the oldest SGS model and it is often used due to its simplicity. The model is obtained from dimensional analysis implying that the eddy viscosity is modelled as:

$$\nu_t = (C_s \overline{\Delta})^2 \sqrt{2\overline{S}_{ij}\overline{S}_{ij}} \tag{4.11}$$

where C_s is a model constant. In the original Smagorinsky model C_s is a constant that has been calibrated for isotropic turbulence. By allowing this modelling constant to vary the modelling error can be reduced and this is done in the so called dynamic Smagorinsky model, where the constant is adapted to the local flow in every node at every time-step. The dynamic model has the advantages that it vanishes in the near wall region and in fully resolved flow regions and it is better able to capture transition processes. The drawback of the model is that it is more complicated and the constant may become too negative, leading to numerical stability problems.

An alternative to using an explicit modelling of the sub-grid scales is to use implicit LES. With this approach the numerical dissipation present from the discretization is assumed to take care of the dissipation at small scales and thereby accounting for the most important role of the SGS terms. A variant of implicit LES is termed MILES - Monotone Integrated Large Eddy Simulation, which is a special version introduced by Boris *et al.* (1992), where monotone numerical methods are used to solve the equations for the filtered variables.

The idea of implicit LES can be described by studying the modified incompressible momentum equation that is satisfied by the numerical filtered solution, which contains numerical errors (e.g. truncation errors):

$$\frac{\partial \overline{v}_i}{\partial t} + \overline{v}_j \frac{\partial \overline{v}_i}{\partial x_j} = -\frac{1}{\rho}\frac{\partial \overline{p}}{\partial x_i} + \nu \frac{\partial^2 \overline{v}_j}{\partial x_i \partial x_j} - \frac{\partial}{\partial x_i}(\tau_{ij}^{SGS} + \tau_{ij}^{num}) \qquad (4.12)$$

where over-lined variables are filtered and τ_{ij}^{num} is additional numerical stresses, which represent the numerical error and is of the order $(\Delta x)^p$ for a p:th order accurate scheme. From the above equation it can easily be seen that the dissipation from the SGS stresses and the numerical discretization are additive. This imply that by using an appropriate numerical method the numerical scheme can act as an SGS model and no explicit model is needed.

The problem is that the numerical dissipation is difficult to control, i.e. the amount of dissipation is not a function of the flow. Therefore it is often argued that it is more physical to use an explicit model together with a low dissipation numerical scheme. At the same time it can be argued that if numerical dissipation already is present in the LES solver, which is the case in all general CFD codes where lower order accurate schemes often are used, it is not desirable to add any additional dissipation in the form of an explicit SGS model. However, if implicit LES is used it is important to be aware of the fact that the result is strongly dependent on the grid resolution and the numerical scheme if the spatial resolution is not adequate (i.e. not well within the inertial sub-range). As the grid is refined and the resolved range is extended towards the Kolmogorov scale, which can be attained nowadays for relatively low Re, LES tends to DNS and thereby the implicit SGS (as well as most explicit SGS) models are in fact *approximations* rather than models in a strict meaning. For more information on implicit LES see Grinstein *et al.* (2007).

The numerical computations presented in this work have been performed with implicit LES. The reason for this is that the numerical dissipation is large enough and does not require any further enhancement. We also make sure that the spatial resolution is such that a proportion of the inertial sub-range is resolved

4.3. Numerical Methods

The Navier-Stokes equations are a system of non-linear partial differential equations and no general analytical solution exist. Instead, numerical techniques are used and the result depends on the specified boundary conditions and for some cases also on the initial condition. To solve the problem numerically the equations are discretized, giving a set of coupled non-linear algebraic equations that are solved. There are three common discretization methods for fluid dynamic problems, finite volume (FV), finite difference (FD) and finite elements (FE). For all numerical 3D simulations presented in this thesis the general compressible CFD code Edge has been used, see Eliasson (2001). This code is based on the finite volume discretization method.

4.3.1. *Temporal Discretization*

There are two main types of temporal discretization, explicit and implicit. Explicit methods are more simple than implicit methods and require less computational effort for each time-step, since the flow field at the new time is calculated using the flow field only at the old time-step. The drawback with explicit schemes is that very small time-steps can be required for stability reasons. In implicit methods an iterative, steady-state like, procedure is used to calculate the flow field at the subsequent time, allowing for significantly larger time steps. This can significantly reduce the computational time for some problems, making the implicit methods the most commonly used.

In LES it is desirable to make sure that no physical information can propagate further than one grid cell at one time step. This gives a coupling between the temporal and the spatial discretization of the problem. This condition is expressed in terms the Courant Friedrichs Lewy (CFL) condition, which states that the Courant number must be less than one

$$\text{CFL} = \frac{U\Delta t}{\Delta x} \leq 1 \qquad (4.13)$$

where Δt is the time step, Δx is the cell size and $U = |u| + c$ is the maximum physical propagation speed, where u is the convection velocity and c is the speed of sound. This is the same condition that theoretically is required for stability of explicit schemes, even though an even lower value often is required in reality depending on the exact discretization scheme and the implementation. However, since a small time-step is required also for physical reasons an explicit temporal discretization has been used.

For the explicit time marching a low storage Runge-Kutta scheme has been used. The advantage of this scheme is that it requires the lowest possible storage for a Runge-Kutta scheme. The disadvantage is that it can formally not be of more than second order accuracy for non-linear problems. In the 3D computations presented in this theses two versions of this Runge-Kutta scheme have been used. The main scheme used is a four stage scheme of fourth order accuracy for steady linear problems. In addition, some of the computations have been performed with a three stage scheme of formally first order accuracy. To only have a first, or even a second, order accurate scheme can be considered low especially for acoustic problems. However, to ensure stability the maximum Courant number was around 0.6, ensuring a very small time-step compared to the spatial discretization size. This implies that in the spatial discretization is the most important parameter for the total accuracy of the problem.

4.3.2. *Spatial Discretization*

The spatial discretization uses a formally second order accurate central scheme. Central schemes have the advantage of having very low numerical dissipation,

which is desirable in LES. The disadvantage is that they can introduce spurious oscillations and unphysical dispersion, which is when the speed of sound becomes frequency dependent. To ensure stability the unphysical oscillations must be damped numerically, which commonly is done by adding some type of artificial, numerical, dissipation to the equations. In the CFD code used in this work a Jameson type of artificial dissipation is added to the central scheme for the inviscid terms, see Jameson *et al.* (1981). The dissipation is a blend of second and fourth order differences, where the former is active in the neighborhood of shocks and is small in smooth flow regions and the latter is switched off in the vicinity of shocks. The implementation of the artificial dissipation in the equations is by adding an extra, dissipative, flux to the inviscid fluxes.

As a comparison a second order blended upwind - central scheme has been tested. The advantage with upwind schemes is that they are less dispersive and do not introduce unphysical oscillations. The disadvantage is that they are dissipative. The blended scheme used is of Roe flux difference splitting type. The convective term is then computed as a central part with additional upwind dissipation.

4.3.3. *Boundary Conditions*

The walls in the domain are specified as adiabatic, i.e. no heat transfer to or from the walls, and either slip or no-slip boundary conditions have been used. The no-slip boundary condition is the physical one (for viscous flows) where all velocity components are forced to zero at the wall. The slip boundary condition only forces the normal velocity to zero, which is compatible with inviscid flows. For the plate walls the choice of boundary condition has been shown not to influence the result and therefore the slip and no-slip boundary conditions have been used for different simulations. At the duct walls the slip boundary condition is used in all presented computations except one. The reason for using this boundary condition is that it gives significantly lower dissipation of propagating waves and it preserves the validity of Equation (3.8) by keeping the theoretical mode shapes, which are destroyed close to the wall with the no-slip boundary condition as the acoustic velocity is forced to zero. The slip boundary condition also decreases the mesh size, since in the absence of the boundary layer, a coarser mesh can be used next to the duct wall.

At external boundaries the theory of characteristics determines the number of boundary conditions that need to be specified. There are in total five characteristics, which correspond to up- and downstream propagating acoustic waves (which in the supersonic case both propagate downstream), entropy waves that are convected downstream with the flow and the downstream advection of the two in-plane velocities. The number of conditions specified at a boundary should be the same as the number of characteristics entering the domain at that boundary. In the subsonic case there are four characteristics that enter the domain at the inlet and one that enters the domain at the outlet.

At the outlet boundary the static pressure has been specified. At the inlet the three velocity components and the density have been specified. When acoustic waves are excited downstream a time varying pressure is used, where an oscillating part is added to the mean value. When acoustic waves are excited upstream time varying normal velocity and density are used, where oscillations are added to the mean values. The velocity and density oscillations are in phase and the amplitudes are related with the acoustic relation in Equation (3.8)

4.3.4. *Computational Grid*

Four different grids have been used in this work, but the basic structure is the same for all of them. To ensure a good mesh in the circular geometry a structured hex grid, based on an o-grid, has been used. The grid looks the same at each cross-section of the duct, with finer cells at the radius of the plate edges and at the duct wall for the simulation with a no-slip boundary condition. In the axial direction the cells are finest at the plate and then successively stretched towards the inlet and the outlet.

One of the grids is for a geometry with longer ducts, where the upstream duct is 15 duct diameter and the downstream duct is 35 duct diameters. At the plate the cell size is one tenth of the plate thickness in the axial direction and there are coarse cells at the duct wall. In the axial direction the cells are stretched with 2.2 % to a maximum cell length of 6.5 mm, which means that for an acoustic wave of 1500 Hz there are a minimum of 30 cells per wavelength. This resulted in a grid with 4.9 million nodes.

The three other grids are for a geometry with shorter ducts, where the upstream duct is 5 duct diameter and the downstream duct is 15 duct diameters. The first of these grids is the longer duct grid, where the ends of the ducts have been cut away, resulting in a grid with 2.4 million nodes. In the second grid the first one has been refined at the duct wall, in order to use a no-slip boundary condition, resulting in a grid with 3.3 million nodes. In the third grid the resolution at duct cross sections and at the plate has been improved compared to the first grid. This gave an axial cell length at the plate that is one twentieth of the plate width. The stretching in the axial direction has at the same time been increased to 4 %, but with the same maximum cell length, resulting in a grid with 5.5 million nodes.

4.4. Determining the Acoustic Two-Port

In this work an acoustic two-port model is used to characterize the acoustics of the studied objects. The two-port used is the scattering matrix, for which the theory is presented in Section 3.3. The plane wave decomposition is performed using both the acoustic pressure and velocity fluctuations, Equation (3.22), since both variables are easily accessible in a simulation. The scattering matrix is at the end moved to the object, since flow fluctuations and acoustic near fields

prevent data from being sampled next to it. The passive part of the two-port is determined using the two-source method. Two simulations are then performed, where acoustic waves are excited at the outlet and inlet boundaries respectively. A harmonic excitation signal is used to ensure a good signal to noise ratio and since the boundaries are reflective, which for broadband excitations can lead to resonances that completely dominate over other frequencies. However, to reduce the computational time a sum of sine waves with different frequencies is excited simultaneously.

4.4.1. *Flow Noise Suppression*

In turbulent flows the generated acoustic waves are accompanied by turbulent fluctuations. In order to get accurate results this so called flow noise has to be suppressed. The properties that separate the acoustic fluctuations from the non-acoustic flow fluctuations is that they have a harmonic time dependence, they propagate with the speed of sound plus / minus the mean flow velocity in the up- and downstream directions, respectively, and at each cross section they can be projected on specific mode shapes depending on frequency. For low frequencies only the plane wave mode, where the acoustic variables are constant at a cross-section, can propagate through the duct. Furthermore, in the case of externally excited incoming waves, these have to be separated from the flow generated sound. This, in combination with the fact that the interesting frequencies are known for incoming waves, but not for generated, leads to some differences in the procedure used to extract the waves. To extract externally excited waves the following methods have been used in the prescribed order:

- The excited waves have higher amplitude than the generated noise.
- The variables are averaged over cross-sections when plane waves are studied.
- The characteristics based filtering method proposed by Kopitz *et al.* (2005) is used to suppress non-acoustic fluctuations.
- Phase averaging is used to suppress fluctuations at other frequencies and with a time varying phase shift.
- Fourier transform of data is performed to extract the excited frequencies.
- The sampled data was as a test correlated with the excitation frequencies, to eliminate uncorrelated fluctuations, but this was not used in the final evaluation.

To extract generated waves different methods should be used depending on whether the sound is broadband or consists of discrete tones. Here is the general procedure for extracting the two types of sound:

- The variables are averaged over cross-sections when plane waves are studied. For higher frequencies the fluctuations have to be projected also on other possible modes.

- The characteristics based filtering method proposed by Kopitz *et al.* (2005) is used to suppress non-acoustic fluctuations.
- For discrete noise the time signal is split into segments that are multiplied with a window function before Fourier transformation and averaging of them.
- For broadband noise the power spectral density (PSD) is calculated using Welch's method, where the data is Fourier transformed and averaged with overlapping time segments.

The most efficient way to suppress flow noise is averaging with many averages, but this requires long time series, which are not available in LES due to the high computational cost. It is however easy to save data at many positions and this is used to improve the results. Below the different methods used and / or tried for suppressing flow noise are described.

Excitation Amplitude

It is important that excited sound waves have higher amplitude than possible flow generated sound waves, because generated sound at the excitation frequencies is neglected. At the same time the amplitude has to be low enough to avoid non-linear effects. It has been evaluated how the amplitude of the excited waves influence the final result of the scattering matrix both analytically and by running simulations with different excitation amplitudes.

Cross-Section Average

In the plane wave frequency range the acoustic pressure and velocity are constant over cross-sections of the duct. Turbulent fluctuations can then be reduced by calculating the cross-section average fluctuations:

$$p_{ac} = \frac{1}{A} \int_A p \, dA, \qquad u_{ac} = \frac{1}{A} \int_A u \, dA \qquad (4.14)$$

An easier alternative is to just calculate the average of the nodes values in the cross-section ($p_{ac} = \frac{1}{N} \sum_{i=1}^{N} p_i$, where N is the number of nodes), since the acoustic pressure and velocity should be the same in all nodes in one cross-section (assuming plane waves). This easier method was used in earlier simulations, but it did not seem to significantly influence the result.

Characteristics Based Filtering

To suppress possible non-acoustic fluctuations the characteristics based filtering (CBF) method proposed by Kopitz *et al.* (2005) has been used. By using the known acoustic propagation speed ($c \pm u$), the acoustic fluctuations at successive planes can be related to each other through:

$$p_+(x,t) = p_+(x + \Delta x, t + \Delta x/(c + u)) \tag{4.15}$$
$$p_-(x,t) = p_-(x + \Delta x, t - \Delta x/(c - u)) \tag{4.16}$$

where Δx is the distance between the planes. This is used to calculate the mean of the fluctuations at several successive planes:

$$p_+(x,t) = \frac{1}{n} \sum_{i=1}^{n} p_+(x + \Delta x_i, t + \Delta x_i/(c + u)_i) \tag{4.17}$$

$$p_-(x,t) = \frac{1}{n} \sum_{i=1}^{n} p_-(x + \Delta x_i, t - \Delta x_i/(c - u)_i) \tag{4.18}$$

Phase Averaging

To suppress noise phase averaging, also called synchronized time domain averaging, is performed. The signal is divided into several segments, with one period of the investigated frequency in each segment. In the case of several excited waves that are harmonics of a lower common frequency the time series is split into segments consisting of one period of this frequency. The average of the time segments is then calculated. This way fluctuations at other frequencies than the studied or its harmonics and with a time varying phase shift will be eliminated. Theoretically the amplitude of the background noise is expected to be reduced as $1/\sqrt{N}$, where N is the number of averages.

The averaging can also be performed in the frequency domain, where each time segment is Fourier transformed before it is averaged, but this gives exactly the same result as performing the averaging in the time domain. The success of the flow noise elimination depends strongly on the number of averages performed.

Fourier Transform

Finally, a Fourier transformation is performed to get the complex wave amplitudes needed to calculate the scattering matrix through Equation (3.15). Here only fluctuations at the excited frequencies are extracted.

Cross-Correlation with the Excitation Signal

A common method to extract externally excited sound waves is to correlate the sampled signals with the excitation signal, which is assumed to be uncorrelated with the generated sound. With this method the phase averaging has to be performed in the frequency domain and each time segment is correlated with the excitation signal in the frequency domain before averaging. The correlation is performed by calculating:

$$\hat{H}_+ = \hat{p}_+ \hat{e}^*, \qquad \hat{H}_- = \hat{p}_- \hat{e}^* \tag{4.19}$$

where $\hat{H}_\pm$ are the correlated variables that are averaged and used to calculate the scattering matrix, $\hat{p}_\pm$ are the Fourier transformed waves and $\hat{e}^*$ is the complex conjugate of the Fourier transform of the excitation signal.

This method of correlating the sampled signals with the excitation signal has been tested and did as expected not have a significant influence on the results. The method has therefore not been used for the final data evaluation.

Fourier Transform and Averaging of Generated Discrete Noise

When sound generation is considered the exact frequencies of the tones are seldom known, or there might be several tones that are not harmonics of each other. If a time segment, containing a non-integer number of periods of a discrete tone, is Fourier transformed the energy at that frequency will leak out in the frequency domain. This phenomenon is called leakage and it is due to the Fourier transform assuming a periodic repetition of the time segment, which in this case gives a discontinuous signal. To reduce the leakage the time segment can be multiplied with a window function, which smoothly forces the signal to zero at the start and end of the segment.

To extract generated discrete tones flow noise has to be suppressed by averaging and leakage has to be avoided. To achieve this the time series is split into smaller segments, which are multiplied with a Hanning window and Fourier transformed before being averaged. However, even though the problem with leakage is reduced it is still important to have a fine enough frequency resolution to evaluate the tones.

PSD of Generated Broadband Noise

When broadband sound is investigated it more appropriate to study the Power Spectral Density (PSD) than the direct Fourier Transform, since it gives a spectra that is less sensitive to the length of the time series used. To suppress flow noise and errors averaging is performed with Welch's method. The time-series is then split into shorter segments and to avoid leakage each segment is multiplied with a Hanning window, which smoothly forces the time series to zero at the start and end of the segments. The PSD of the segments is then calculated and averaged to give the sound spectra. When a broadband signal is studied it is possible to split the signal into overlapping segments. The optimal amount of overlap depends on the window function used. For the Hanning window it is 50 %. So to reduce the error, the time series is split into segments with this overlap.

4.5. Extracting Acoustic Sources

When sound generation is considered it is usually not only of interest to study the generated sound spectra, but also to investigate the sound generating mechanisms. There is no straight forward universal method for identifying the acoustic sources, as discussed in Section 3.5. Instead a good understanding of possible source mechanisms is required to choose an appropriate method for identifying them. For the orifice plate geometry the low frequency sound generation is believed to be connected to the axial force on the plate. As a first step in investigating the sound generation the total axial force on the plate should therefore be studied and compared to the radiated sound.

4.6. Proper Orthogonal Decomposition

Proper Orthogonal Decomposition (POD) is a decomposition method that decomposes the flow field into a set of orthogonal modes, according to Equation (4.20). These modes are optimal in the sense that the truncated reconstruction captures the kinetic energy of the flow field with a minimal number of terms. The coefficients of the modes in the expansion are often used to assess how fast the expansion converges. The different energetic modes often describe coherent structures, which characterize important features of the flow. Reconstructing the flow field with a limited number of POD modes allows studying coherent structures independent of the turbulent part of the flow. For a flow where the coherent structures have a high energy content the POD will decompose the flow field into a mean part, a second component of coherent structures that evolve in time and a turbulent (incoherent) part:

$$u(x, t_k) = \underbrace{a_0 \varphi_0(x)}_{\overline{u}(x)} + \underbrace{\underbrace{\sum_{j=1}^{J} a_j(t_k)\varphi_j(x)}_{coherent} + \underbrace{\sum_{j=J+1}^{\infty} a_j(t_k)\varphi_j(x)}_{incoherent}}_{fluctuations} \qquad (4.20)$$

where j denotes mode number, k the time step, $a(t)$ the POD coefficients and $\varphi(x)$ the POD modes. Once these modes are determined one may express the dependent variables in terms of the POD expansion, Equation 4.20.

In this work the velocity field has been decomposed into POD modes in order to study coherent structures in the jet formed downstream of the plate.

4.7. Numerical Accuracy and Uncertainties

When a numerical computation is performed there are several sources of error that could affect the accuracy of the result. First of all there can be modelling errors, which means that the governing Equations (4.1 - 4.8) are not correctly describing the flow. These equations have however with good results been used

for a long time for this type of flows and should not introduce any significant error. The error would instead be in the implicit LES assumption, that the equations are still correctly describing the flow when the small scales are not resolved.

The largest error source in LES is probably the discretization error, which comes from the discretization of the equations and the flow variables. This error depends on the numerical schemes used to solve the problem and on the spatial and temporal resolution. In the study presented in this work formally second order accurate schemes have been used both in time and space. Furthermore, it is assumed that it is the spatial resolution that is limiting the accuracy, since the explicit temporal scheme used requires a very small time-step compared to the corresponding spatial discretization. As a computer performs computations with a limited number of significant digits there can also be round off errors. However in this work the computations have been performed with double precision, which practically eliminates the round off error.

Additional possible errors can come from short simulation times. When a new simulation is started it takes some time before the flow field reaches statistical steady state. So unless this startup transient is to be studied, it should be avoided to include it in the data analysis. Furthermore, when unsteady flow is studied it is the statistics that are of interest, so averaging has to be performed to avoid errors from too few number of samples. One then has to make sure that the sampling time is long enough. In this work the effect on the scattering matrix from varying the number of averages has been studied for one case to ensure an acceptable level of the error, see Section 6.4.

An uncertainty, which is not exactly an error, but significantly can affect the result in some cases is the boundary conditions. Some problems are very sensitive to changes in the boundary conditions and a few percent change in e.g. the inlet velocity can have a significant effect on the result. This is of importance to know, since it normally is assumed that the result is valid even if the conditions are not exactly the same as those in the simulation.

To verify the results one can do a numerical accuracy study, where the discretization errors are investigated by computing the flow on successively finer grids. Numerical accuracy studies are used both to get the apparent order of accuracy of the numerical schemes, as compared to the formal order of accuracy, and to investigate the numerical uncertainty in the results. In this work no systematic numerical accuracy study has been performed. However, a grid refinement has been performed in the region of the plate and it did not show a significant effect on the scattering matrix, which is the interesting parameter.

To validate the computational results they can be compared to experimental or DNS results, where the latter only can be used for low Reynolds number

flows and therefore not for the problems presented in this work. When simulations are compared to measurements the resulting error is the sum of all errors and uncertainties and it is difficult to say where the discrepancies come from. Furthermore, the accuracy of the measurements and possible differences between the real and the specified boundary conditions have to be considered. The exact boundary conditions are often not given for the experiment, especially if the flow is non-stationary. It may also be difficult to numerically specify the physical boundary condition. This can give discrepancies in the flow field between the simulations and measurements that are not due to errors.

The result of the 3D computations performed in this work were compared to measurements performed by Allam & Åbom (2005) with reasonable agreement. The comparison was performed for the scattering matrix, since there were no adequate measurements of the flow field. The main uncertainty in the comparison is the inlet conditions, which were not measured exactly. Because of this, the influence of the inlet Mach number has been studied in the simulations, showing that it does influence the result. Another uncertainty is the exact geometry of the orifice plate, where the sharpness of the edges can influence the result.

CHAPTER 5

1D Models and Methods

The 1D simulations were carried out with GT-Power, a commercial quasi 1D CFD tool for engine simulations. The equations governing the flow (Equation (4.1- 4.3)) are averaged over duct cross-sections, keeping the cross-sectional area of the ducts as an input variable. The viscous term is modelled via a pressure loss term and a friction term in the momentum equation, while it is neglected in the energy equation. Both the pressure loss term and the friction term are proportional to the kinetic energy of the flow and a pressure loss and a friction coefficient, respectively. These coefficients can be specified by the user.

A problem is set up by connecting components that model different physical objects, such as straight and bend pipes, junctions, orifices, compressors, engine cylinders etc. The 1D flow equations are solved for flow objects like e.g. pipes or flow connections. Various objects have different specific functions and act as boundary conditions between the flow objects.

5.1. Numerical Methods

Just as the 3D flow equations the set of 1D equations is a system of non-linear partial differential equations without a general analytical solution. The system is solved using numerical techniques and the result depends on the specified boundary conditions and object input data and model coefficients. To solve the problem numerically the equations are discretized, giving a set of coupled non-linear algebraic equations that can be found in GT-Power (2004).

The discretization is performed such that the ducts are split into smaller volume (control) elements with connecting boundaries. The basic conservation laws are satisfied in each volume element. Flow connections, like orifices, are boundary planes between neighbouring elements.

The temporal discretization uses an explicit formally first order accurate Euler scheme. This is the recommended scheme for accurately capturing pressure pulsations and the alternative would be an implicit scheme. The disadvantage with the explicit scheme is that small time-steps have to be used to fulfil the CFL condition, Equation (4.13), which results in longer simulation times.

5.1.1. *Boundary Conditions*

The wall boundaries are considered to be adiabatic and for pipe components a skin friction coefficient, or a surface roughness, has to be specified. In the present work the friction has been set to zero in some pipes and very large in other to either minimize the dissipation or get dissipation of acoustic waves, see Section 5.2.

At external boundaries the theory of characteristics allows one to determine the number of boundary conditions that have to be specified. The number of conditions should be the same as the number of characteristics entering the computational domain at that boundary. In the 1D case there are in total three characteristics, where for subsonic flows two propagate downstream and one upstream. This means that two conditions have to be specified at the subsonic inlet and one at the subsonic outlet of the domain. In the present work, temperature and mass flow or velocity are specified at the inlet and at the outlet the static pressure is specified with a non-reflecting boundary condition.

Acoustic waves are excited by so called end flow loudspeakers, which are connected to the system through t-junctions. With this object a constant temperature and an oscillating velocity are imposed in the side branch of the t-junction. The oscillations imposed consist of a sum of sine waves, with 21 equally spaced frequencies from 50 Hz to 1050 Hz.

5.2. General Model Setup

The setup of the general model for the 1D simulations can be seen in Figure 5.1, where the component is either the model for the orifice plate or for the compressor. The component is connected to one upstream and one downstream duct. These ducts have a fine mesh and the skin friction coefficient is set to zero to minimize the dissipation of acoustic waves. After the ducts there are optional t-junctions with loudspeakers connected to the side branches. These elements are present in the model when acoustic waves are excited at that side of the component. After the t-junctions there are additional pipes before the domain boundaries, where the downstream pipe only is present in combination with the downstream speaker. These ducts have a coarse mesh and a high skin friction coefficient to minimize reflections from the boundaries by dissipating the acoustic waves.

5.3. Orifice Plate Model

The orifice plate is modelled with an orifice element, which numerically is modelled as a plane where the momentum equation is solved to compute the mass flow through the orifice. The orifice plate is given its physical diameter and thickness, with the exception of one simulation in which the effect of neglecting the thickness is investigated.
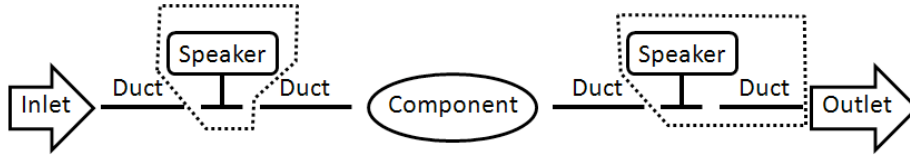
FIGURE 5.1. General model setup, where the components is either an orifice model or an compressor model.

FIGURE 5.2. Compressor model setup, where C is the compressor and the circles are the two volumes.

The vena contracta at the orifice is characterized by a discharge coefficient, which is defined as the effective flow area over the reference flow area, i.e. the orifice area. A discharge coefficient of unity indicates an orifice with softly rounded edges that do not give rise to a vena contracta effect, while a lower value has to be used for sharper edges that give a stronger vena contracta effect. In the computations presented in this thesis the recommended discharge coefficient for sharp edges has been used. The exception is a couple of simulations where the effect of varying it has been studied.

5.4. Compressor Model

The standard way of modelling the compressor is using experimental data, which is summarized in a compressor map. Such data is determined for steady flow through the compressor. The map, which is supplied by the turbocharger manufacturer, relates the compressor speed, pressure ratio, mass flow and efficiency. It consists of a table of operating points measured under steady state conditions and data is interpolated from the measuring points to other parts of the map.

To start with the compressor was modelled with just the map connected directly to two pipes. Then two volumes, corresponding to the rotor volume and the volume of the volute, were added to the model between the map and the pipes, see Figure 5.2. This setup follows that of Rämmal & Galindo (2010), who successfully simulated the passive acoustics of a compressor using a 1D CFD code.

The compressor map object uses the rotational speed, which is specified, and the pressures at the connected volumes look up the mass flow in the map and impose it on the boundaries of the adjacent volumes. In some regions of a map the speed lines can be flat, which means that a small pressure change can

result in a large mass flow change. So to avoid problems with large mass flow variations the fluctuations can be damped. The damping is per default on, but it has been tested to run both with and without it. (GT-Power 2004)

The compressor volumes are represented by either straight pipes or by spherical or general flow split objects. Straight pipes are given the same cross-sectional area as the connecting pipes, a length that gives the required volume and zero friction and a fine mesh to avoid dissipation (since this is already included in the map). When flow splits are used default orifice objects are automatically inserted between the map and the flow splits. The flow splits are numerically seen as one cell, where the scalar equations are solved in the middle and the momentum equation at all boundaries. The spherical flow split can be seen as a spherical cavity to which several pipes are connected and with only one connecting pipe it is said to behave as a Helmholtz resonator. In the present work it is connected to two pipes at opposite sides. The general flow split can be seen as a volume of general shape, to which several pipes (in this work two) are connected.

5.5. Determining the Acoustic Two-Port

The acoustic waves are extracted and the two-port, in form of the scattering matrix, is determined as described in Section 4.4, for the evaluation of the LES results. The difference is that no area averaging can be performed in 1D. Furthermore, since the code has proven to be dissipative it is desirable to sample data as close to the object as possible and since there are no turbulent fluctuations in 1D and the elements studied do not introduce any disturbances it is also possible to sample data very close to the object. Data is then sampled at six positions in the upstream pipe and at eight positions in the downstream pipe.

For the compressor simulations the scattering matrix results are used to calculate the transmission loss, which gives information about how much acoustic power that is lost as the wave passes the compressor and therefore is an interesting parameter in engine contexts. The transmission loss is calculated according to the procedure presented in Section 3.4.

5.6. Numerical Accuracy and Uncertainties

The main uncertainty in 1D simulations is the modelling. In commercial programs the implementation details are not always known exactly. In general, it can be said that the models for the different objects are based on steady state measurements and are developed with the aim of getting the mean engine performance in agreement with experimental results. The extrapolation of the model to unsteady flows is not self-evident, since the interaction between unsteadiness and inertia is important. The basic assumption of quasi-steadiness introduces large uncertainties in the ability of the code to capture acoustic

waves correctly. In addition to the modelling issue of the separate objects, the coupling between the objects is an uncertainty that can cause problems. For the compressor modelling there are also additional uncertainties from the interpolation of the map (from measured to simulated operating points) and from the damping of mass flow fluctuations.

In 1D engine simulations, low order accuracy schemes are used in combination with coarse meshes. This can give rise to discretization errors, which come from the discretization of the equations and the flow variables. In this work grid refinements have been performed in the pipes next to the investigated object to ensure a grid independent result for the scattering matrix, which is the interesting parameter. This resulted in cells much smaller than those recommended for engine simulations and a significantly reduced wave propagation distance from the object to the data extraction positions, due to high dissipation.

To check the validity of the results presented in this work they have been compared to measurements performed at KTH for the same geometries. The scattering matrix of the orifice plate was compared to measurements performed by Allam & Åbom (2005). The compressor transfer matrix was compared to measurements performed by Tiikoja *et al.* (2010).

CHAPTER 6

3D LES Results

Here, the result from simulations of the scattering of acoustic waves by an induct orifice plate are presented. The aim is to investigate the possibility of studying passive acoustic properties of duct components with LES and a common CFD solver. The geometry is a circular duct with a diameter of 57 mm and a 2 mm thick orifice plate with an area contraction ratio of 0.28. The simulations have been performed with the inlet Mach numbers 0.08 and 0.1 and several frequencies are studied simultaneously to reduce the computational time. First, the flow field in the duct and its characteristics has been studied. Thereafter, the sensitivity to numerical parameters (mesh spacing, spatial discretization scheme, duct wall boundary condition) and inlet Mach number are investigated. This is followed by a study of the effect of the flow noise suppression methods presented in Section 4.4.1. Finally, the computed scattering matrix is compared to measurements and theory.

In the following the term upstream coefficients correspond to the upstream reflection and the up- to downstream transmission, i.e. the scattering matrix elements that affect waves coming from the upstream side. Similarly, the term downstream coefficients correspond to the downstream reflection and the down- to upstream transmission, i.e. the scattering matrix elements that affect waves coming from the downstream side.

6.1. Flow Characteristics

The flow through the constricted duct is computed with an inlet Mach number of 0.8 and with slip boundary conditions at the walls. The mean flow is shown in Figure 6.1. It can be observed that a jet is formed as the air is forced through the small opening and a large pressure drop occurs, with some pressure recovery further downstream. The density field further shows significant compressibility effects, as is also reflected in the high Mach number of the jet. Figure 6.2 shows snapshots of the instantaneous flow field. Here it can be observed that the instantaneous flow is highly unsteady, with vortex shedding at the plate and recirculation regions behind the plate. The shear layer that is formed by the constriction is a strong source for turbulence and noise.

The theory by Allam & Åbom (2005), which is presented in Section 3.7.1, predicts that the acoustic scattering by the plate depends on the pressure loss
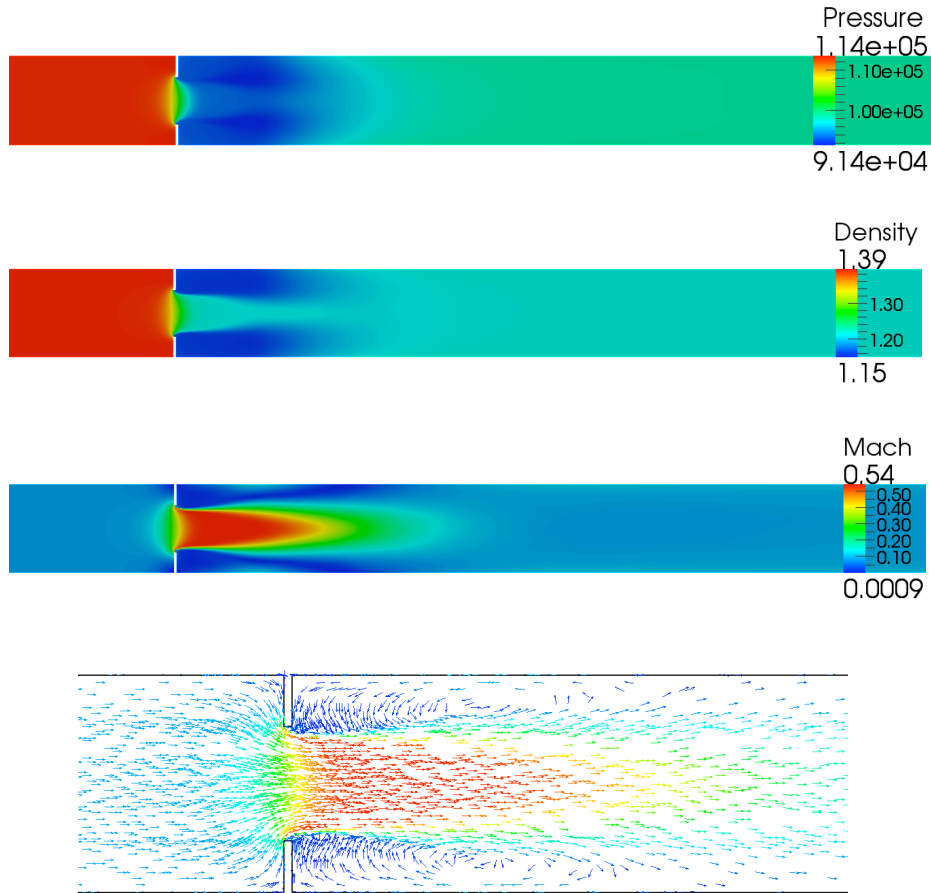
FIGURE 6.1. Zoom in on the flow through the orifice plate. The top three figures show the mean field and the bottom figure shows the normalized in-plane mean velocity vectors coloured by Mach number.

coefficient (C_L), which is derived assuming incompressible flow. In Table 1 the simulated pressure loss coefficient, at two inlet Mach numbers, is compared to the theory. It can be observed that the simulated pressure loss is slightly Mach number dependent and there is a discrepancy compared to the theoretical value. This indicates that the theory might have deficiencies due to the incompressibility assumption, which is clearly not valid at these flow speeds, see Figure 6.1. Another parameter that could influence the result is the sharpness of the orifice edges, where more rounded edges yield a lower C_L value.
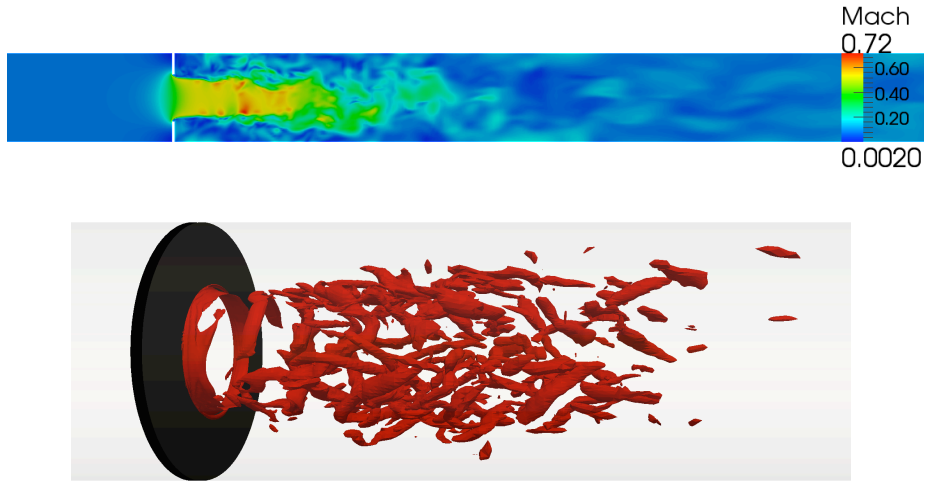
FIGURE 6.2. Zoom in on the instantaneous flow through the orifice plate. The top figure shows the Mach number and the bottom figure shows vortex cores.

TABLE 1. Comparison of the simulated, theoretical and measured pressure loss coefficients over the plate, where the last is from Allam & Åbom (2005).

	C_L
Simulation $M = 0.08$	26.7
Simulation $M = 0.1$	28.0
Theory	22.2

However, the simulated geometry has very sharp edges, which also is the assumption in the theory. There might also be accuracy issues in the simulations. An insufficient grid resolution of the plate could e.g. result in a discrepancy. However, a grid refinement study has shown not to give a significant change in the pressure loss. A parameter that turned out to have some effect on the pressure loss is the spatial discretization scheme. Changing from the central scheme to the more dissipative blended (upwind and central) scheme lowered the pressure loss coefficient from 28.0 to 25.7 for the $M = 0.1$ case, see Section 6.2.2.
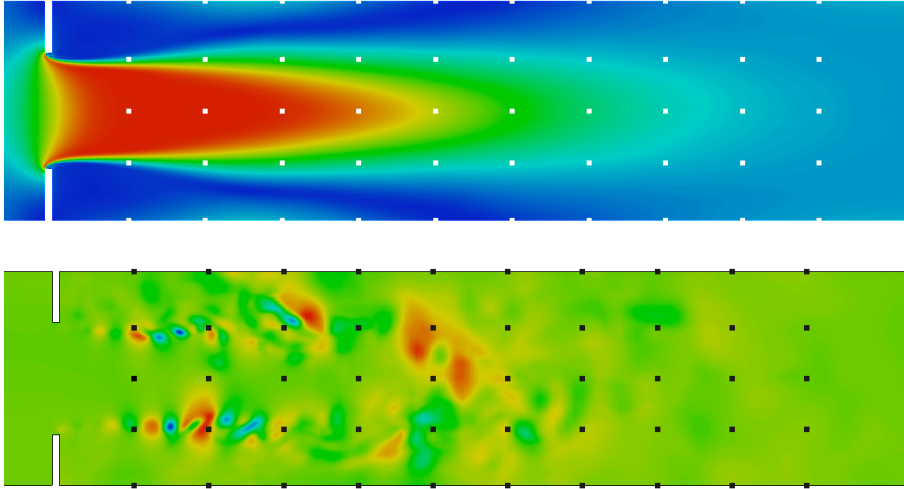
FIGURE 6.3. Data sampling positions in the jet. In the top figure with the mean Mach number and in the bottom figure with instantaneous pressure fluctuations. The axial distance between the probes is 2 cm and the first probes are 2 cm downstream of the plate.

6.1.1. *Flow Statistics*

As can be observed in Figure 6.2 the flow is highly unsteady downstream of the plate. To study the flow fluctuations data is sampled at 50 positions downstream of the plate. The data sampling points (probes) are distributed along five lines at different radial positions: the centreline, the jet shear layer and the wall, where the two latter are at two circumferential positions separated by 180°, see Figure 6.3.

The largest flow fluctuations are in the shear layer where the jet breaks down, which can be observed in Figure 6.4 of the Reynolds stresses, i.e. the r.m.s. velocity fluctuations. In the figure it can further be observed that the axial velocity has the highest fluctuation level and the fluctuations fast decrease downstream of the jet breakdown. The axial and radial fluctuations can be seen to be correlated, where an instantaneous increase in the axial velocity is accompanied by an increase in the radial velocity. The instantaneous circumferential velocity is however uncorrelated with both the axial and the radial fluctuations, where only the former Reynolds stress (uw) is shown in Figure 6.4. The fact that the axial velocity fluctuations are positively correlated with the radial fluctuations in the shear layer, while the circumferential velocity fluctuations are relatively uncorrelated with both the axial and radial velocity fluctuations, can further be seen in Figure 6.5 of the correlation between the
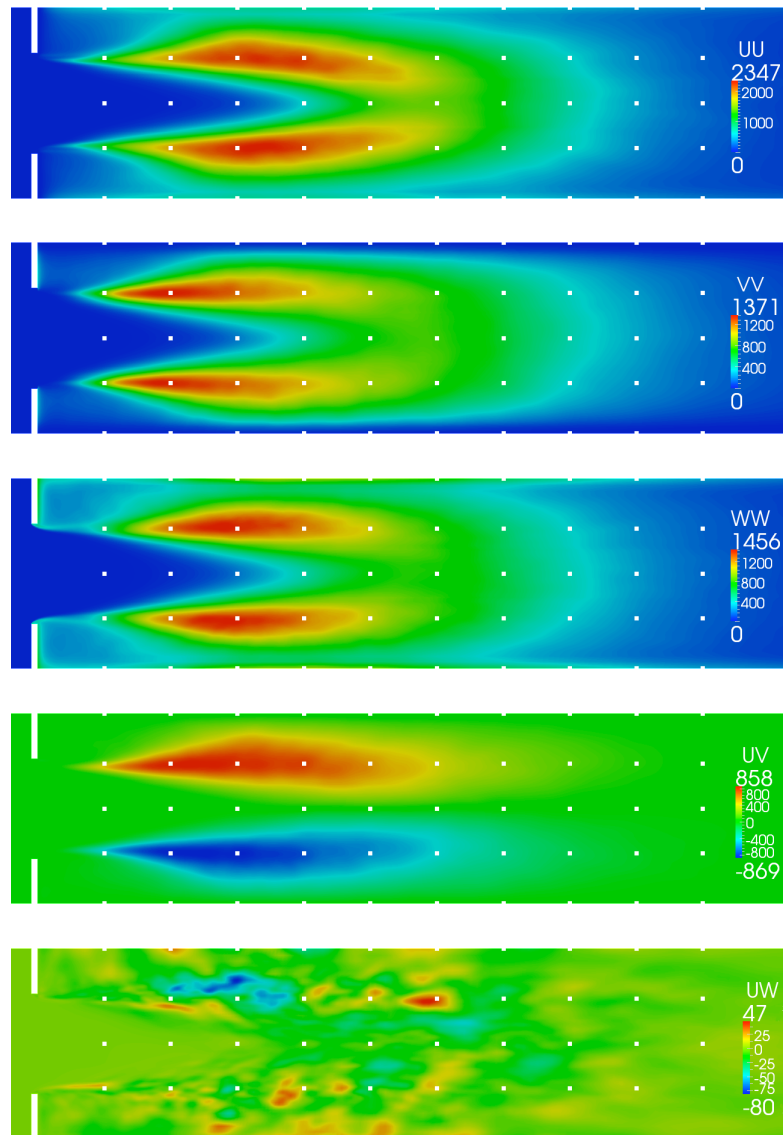
Figure 6.4. Reynolds stresses in the jet downstream of the plate. The figure is such that u is the axial velocity, v is in the plane positive in the upward direction and w is the velocity out of the plane. The white dots are the data sampling positions used to study the statistics of the flow.
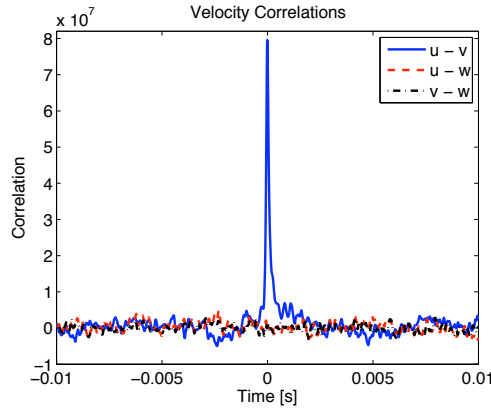
FIGURE 6.5. Correlation between the velocity components in the shear layer, third probe from the plate.

different velocity components. Here it can also be observed that the correlation between the axial and radial velocity fluctuations is very high instantaneously, but decreases fast if a time shift is introduced between the two components.

The development of the fluctuation amplitude along the duct centreline and the shear layer can be studied in Figure 6.6, of the Probability Density Function (PDF) of the pressure fluctuations. A broad low peak indicates that there is a high probability of the pressure instantaneously deviating significantly from its mean value, while a narrow high peak indicates that there only are small fluctuations around the mean pressure. For periodic fluctuations two peaks are usually observed in the PDF, one at each side of the zero fluctuation line. However, when the periodic fluctuations are accompanied by high levels of random fluctuations this phenomenon might not be visible. In general it can be said that Figure 6.6 shows large fluctuations in regions where the Reynolds stresses were found to be large, see Figure 6.9. The largest fluctuations are found in the shear layer a short distance downstream of the plate. At the centreline the fluctuations are smaller and the largest fluctuations are found significantly further downstream than in the shear layer. However, a couple of duct diameters downstream the centreline and shear layer PDFs become very similar.

In order to find coherent structures in the flow field a Proper Orthogonal Decomposition (POD) of the velocity has been performed. The velocity has been decomposed into 10 modes using 480 snapshots. The zeroth mode represents the mean flow as it should, see Figure 6.7. To study vortex structures in the flow, the vortex cores of the modes are studied through λ-2 in Figure 6.8. For some of the modes and when all modes are added together ring vortices
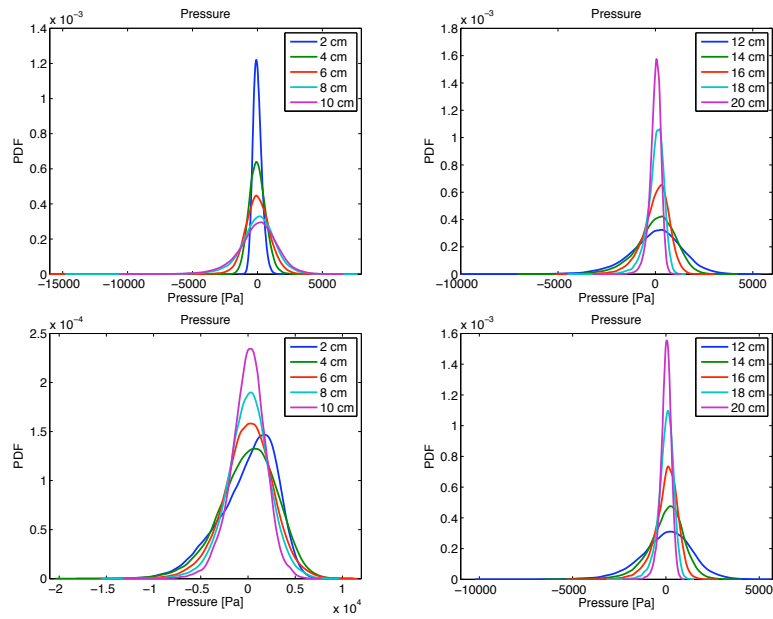
FIGURE 6.6. Probability density function of the pressure at different downstream positions of the jet centerline at the top and of the shear layer at the bottom.

can be observed to be shed at the plate and break down around one duct diameter downstream. Studying individual modes these ring structures are however clearly seen first in higher modes (mode 6, 8 and 9). The other modes seem to contain fluctuations from the jet breakdown.
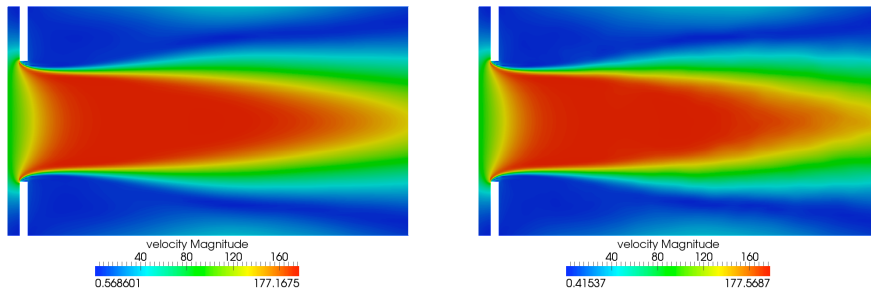
FIGURE 6.7. The mean velocity to the left and the zeroth POD mode to the right.
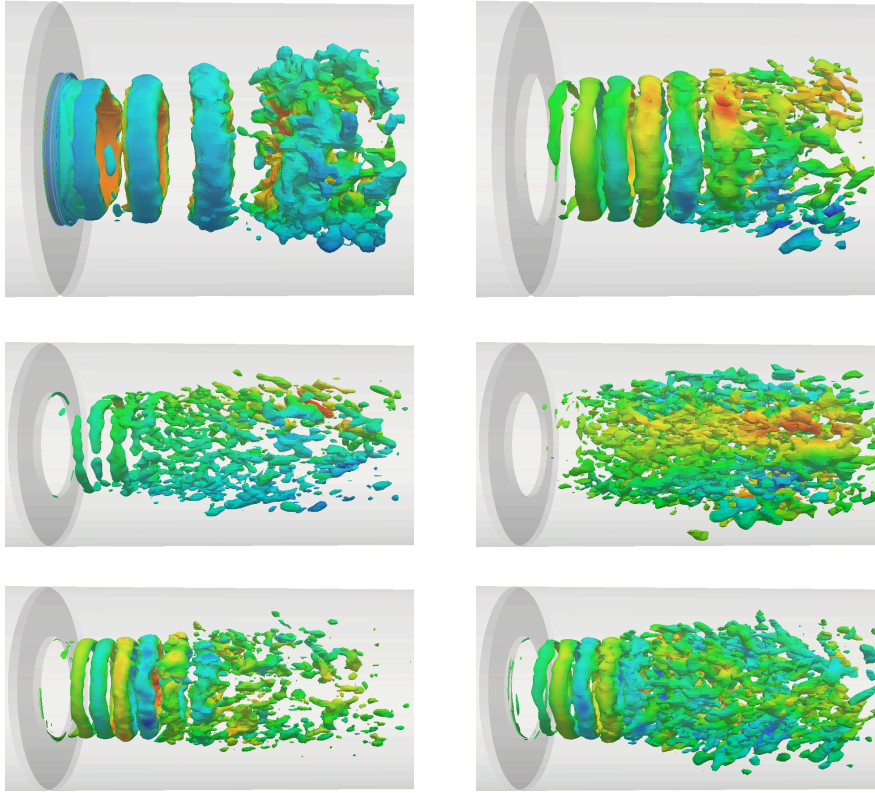
FIGURE 6.8. Contours of λ-2 for the POD modes (coloured by axial velocity). Top left: mode 0-9 (λ-2= $-2 \cdot 10^7$). Top right: mode 1-9 (λ-2= $-2 \cdot 10^7$). Middle left: mode 1 (λ-2= $-5 \cdot 10^6$). Middle right: mode 5 (λ-2= $-2 \cdot 10^5$). Bottom left: mode 6 (λ-2= $-2 \cdot 10^6$). Bottom right: mode 8 (λ-2= $-2 \cdot 10^6$).

The Power Spectral Density (PSD) of the pressure and velocity fluctuations downstream of the plate are shown in Figure 6.9 - 6.11. Figure 6.9 shows the pressure spectra, the axial velocity spectra and the y-velocity spectra in the 10 probes along the duct centreline. The z-velocity spectrum has been left out due to it being very similar to that for the y-velocity. Figure 6.10 shows the spectra for the pressure and the three velocity components in the first five probes positioned along the shear layer. Further downstream, i.e. in the last five probes, the velocity spectra are similar to those along the centreline and the pressure spectra are similar to the wall pressure spectra, shown in Figure 6.11.
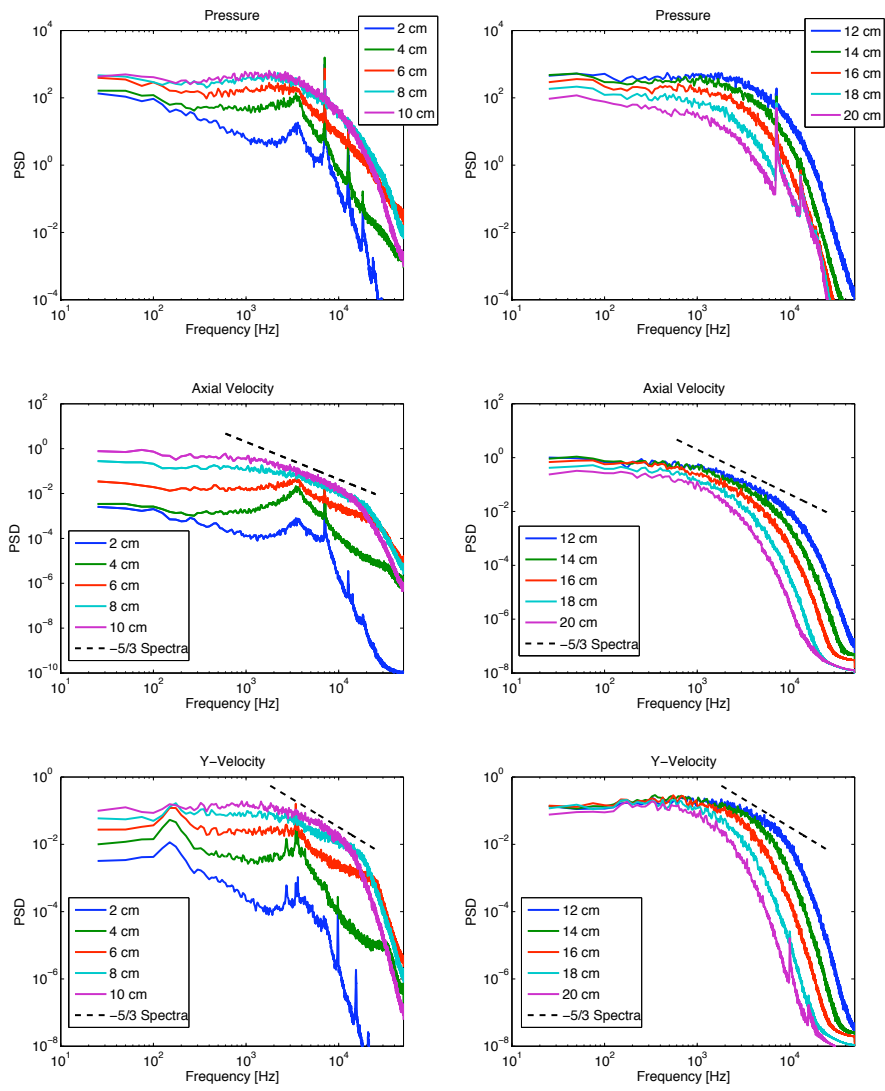
FIGURE 6.9. Spectra of the flow fluctuations at the jet centerline for ten positions downstream of the plate.
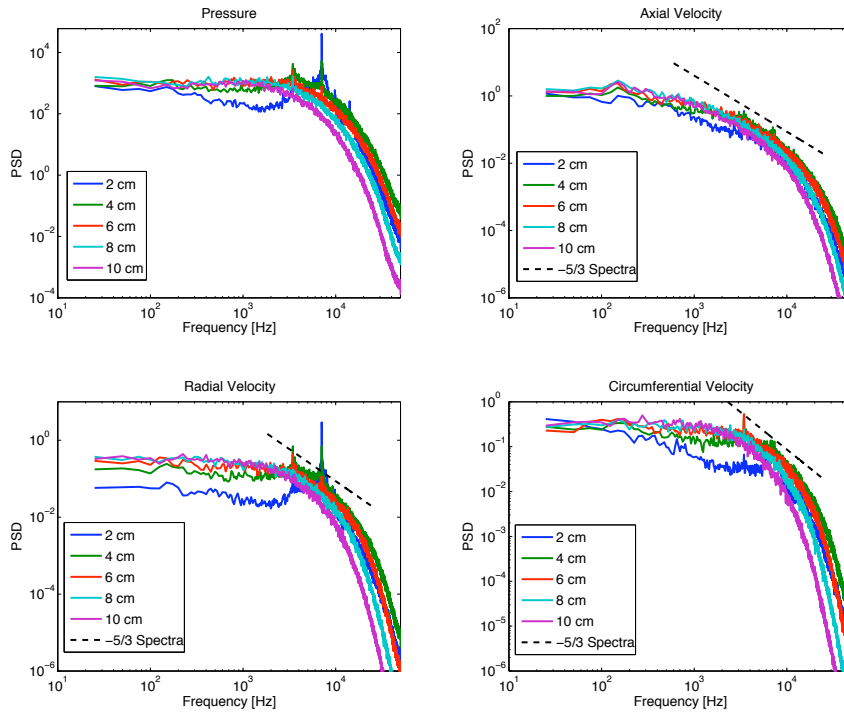
FIGURE 6.10. Spectra of the flow fluctuations in the shear layer at five positions downstream of the plate.
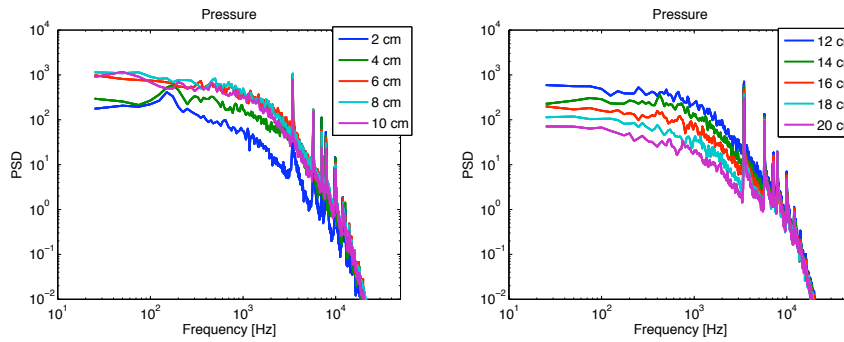
FIGURE 6.11. Wall pressure spectra at different positions downstream of the plate.

Figure 6.9 - 6.11 show, in accordance with Figure 6.4 and 6.6, that the amplitude of the fluctuations first increase downstream, becoming largest where the jet breaks down and thereafter starts to decrease. At around one duct diameter (5.7 cm) downstream of the plate the spectra resemble a Kolmogorov spectrum, with a -5/3 slope of the velocity fluctuations. Further upstream the spectra have a different character due to the fluctuations not being those of homogeneous, isentropic turbulence that the -5/3 slope represents. The spectra downstream the mesh stretching is deviating from the -5/3 slope due to the decreasing resolution and hence the energy in the resolved fluctuations decreases. This is however desired since the only aim is to resolve the low frequency, acoustic waves in the duct downstream of the jet.

Studying the PSD in Figure 6.9 - 6.11 in more detail some characteristics can be observed. One is a low frequency peak at around 150 Hz. The peak is strongest close to the plate and dies out downstream. Furthermore, it is only visible in the y-velocity at the centreline, the axial and radial velocities in the shear layer and in the wall pressure spectra. The low frequency could suggest an acoustic resonance, but the corresponding wavelength is approximately 2.6 upstream duct lengths and 1.1 downstream duct lengths. Furthermore, a low frequency acoustic resonance should be most clearly seen in the pressure and axial velocity spectra and should not die out downstream. The fact that it is strongest in the radial direction instead suggests that it is some sort of oscillation of the jet, but the origin of it is unknown at this point.

An important observation that can be made in Figure 6.11, of the wall pressure spectra, is peaks at the cut on frequencies of the first higher order non-plane duct modes, which are 3500 Hz, 5700 Hz, 7200 Hz, 7900 Hz and 10000 Hz. The peak at 3500 Hz is also clearly visible in both the pressure and velocity spectra at the duct centreline close to the plate, but there it is more of a narrow band peak, see Figure 6.9. The peak can also be observed in the shear layer spectras in Figure 6.10, but there it is significantly weaker.

At around 7000 Hz a strong peak can be observed for the pressure and axial velocity fluctuations at the centreline (Figure 6.9), as well as for the pressure and radial velocity fluctuation in the shear layer (Figure 6.10). With the exception of the centreline pressure, the peak is only visible close to the plate, as the fluctuations seem to decrease downstream. The peak is believed to correspond to the vortex shedding frequency at the plate. When the POD modes of the velocity field are added together the ring vortices shed at the plate are clearly visible, see Figure 6.8. By studying the distance between these vortices and their convection velocity it is possible to get an estimate of the shedding frequency. The exact convection velocity is not known, but it can be estimated from the data sampled in the first and second shear layer probes, see Figure 6.3. The mean velocity in these points is 47 m/s and 83 m/s, respectively. The pressure correlation between the probes has a maximum for a time shift of $\Delta t = 2.1 \cdot 10^{-4}$ s, see Figure 6.12, indicating a convection velocity
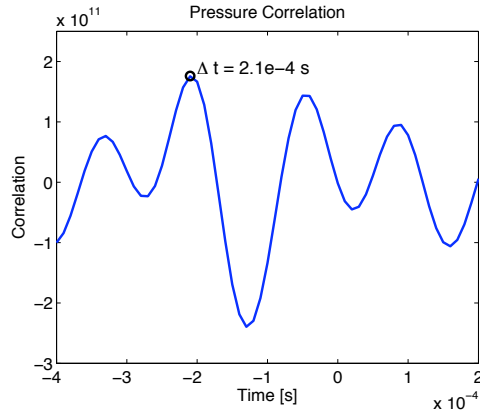
FIGURE 6.12. Correlation of the pressure in the first and second shear layer probe points.

of 95 m/s. Assuming that the peak at 7000 Hz is the vortex shedding frequency the convection velocity would be around 77 m/s. This is likely to be the case, based on the mean velocity at the probe points and the convection velocity between them, where the second probe is located some distance downstream of the studied vortices. Furthermore, the Strouhal number ($St = fD/U$) based on the shear layer thickness and a convection velocity of 77 m/s is $St = 0.27$.

An additional observation that can be made in Figure 6.9 is that the velocity fluctuations perpendicular to the flow direction (only y-velocity shown) at the centreline have a peak at around 9800 Hz instead of 7000 Hz. This corresponds to Strouhal numbers of 0.27 and 0.18 based on the shear layer thickness and the plate thickness, respectively. Furthermore, the centreline pressure and axial velocity spectra have a second peak at around 12600 Hz, while the centreline y-velocity spectra have a second peak at around 15400 Hz, none of them being harmonics of the first peak. An explanation for why the in plane velocity fluctuations have different frequencies at the centreline has not yet been resolved.

The correlation of the flow fluctuations at two opposite sides of the jet shear layer can be studied in Figure 6.13. The correlations have been normalized by the r.m.s. value of the fluctuations at one side of the shear layer, meaning that a correlation of 1 would indicate identical fluctuations. It can be observed that close to the plate the pressure and radial velocity fluctuations at the two sides of the shear layer are strongly correlated for small time shifts, while the axial velocity fluctuations are significantly less correlated. The correlation of the circumferential velocity fluctuations, which is not shown, is similar to that of the axial velocity fluctuations. The strong oscillating correlation, which is high and positive at zero time shift, is due to the vortex rings that are shed at
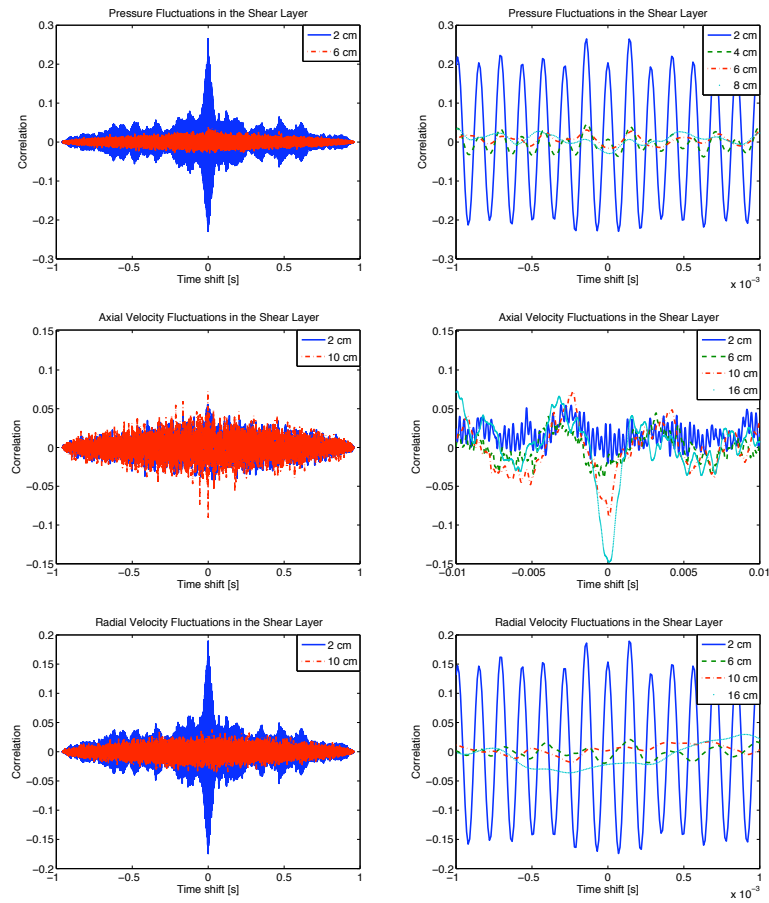
FIGURE 6.13. Correlation of the fluctuations at two positions in the jet shear layer separated by 180°, for different axial positions. The figures to the right are a zoom in on the figures to the left.

the plate. These rings keep their structure only a short distance downstream before they break up, see Figure 6.8, which causes the decrease in the correlation. A phenomena that can be observed for the axial and circumferential velocity fluctuations is a negative correlation at zero time-shift some distance downstream of the plate. This indicates that a positive velocity at one side of the shear layer is accompanied by a negative velocity at the opposite side.
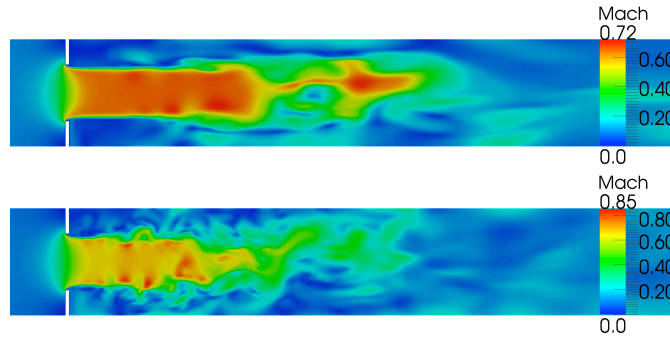
FIGURE 6.14. Instantaneous Mach number computed with a blended (upwind and central) scheme at the top and with a central scheme at the bottom.

6.2. Sensitivity to Numerical Methods

6.2.1. *Grid Dependence*

The original grid was refined around the plate and the scattering matrix was computed for an inlet Mach number of 0.1. The result is compared to the scattering matrix computed with the original Mesh in Figure 6.15. It can be observed that refining the mesh does not significantly influence the result, implying that the original mesh is fine enough to capture the scattering. This was also observed in Section 6.1, where refining the mesh did not significantly change the pressure loss over the plate. The small differences that can be observed are within the uncertainty in the results, due to a small difference in the inlet Mach number and a shorter simulation time for the finer Mesh. Most difference can also be observed in the downstream reflection and the up-to downstream transmission, which are the most sensitive to flow disturbances and thereby the simulation time, see Section 6.4.1.

6.2.2. *Spatial Discretization Scheme*

The sensitivity to the spatial discretization scheme has been investigated by changing from the central scheme otherwise used to a blended (upwind and central) scheme. Figure 6.14 of the instantaneous flow field shows that the blended scheme, as expected, is much more dissipative. Studying the mean pressure drop over the orifice it is reduced from 23000 Pa to 21000 Pa when changing to the blended scheme. This results in a change of the pressure loss coefficient from 28.0 to 25.7.

The scattering matrix has also been computed with the blended scheme and the result can be compared to that with a central scheme in Figure 6.16. No clear influence on the result can however be observed, except for in the phase of the downstream reflection, where there is some noise in the results.
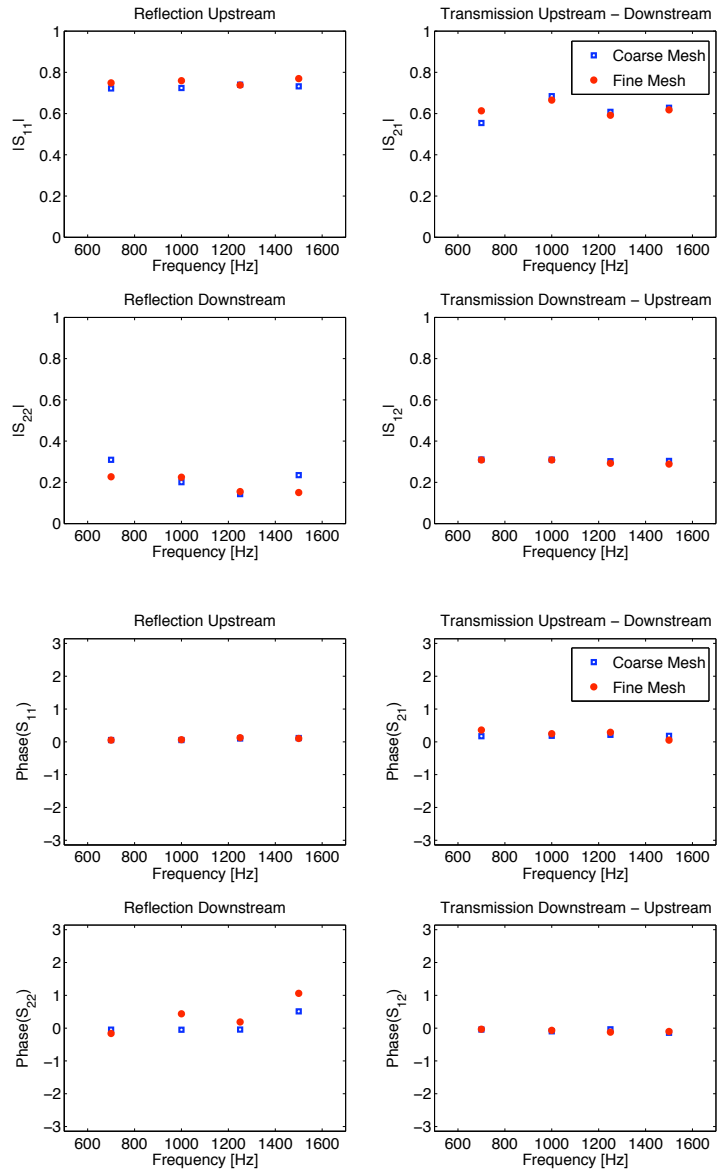
FIGURE 6.15. The scattering matrix computed with two different grids around the plate. The top four figures are the amplitude and the bottom four are the phase.
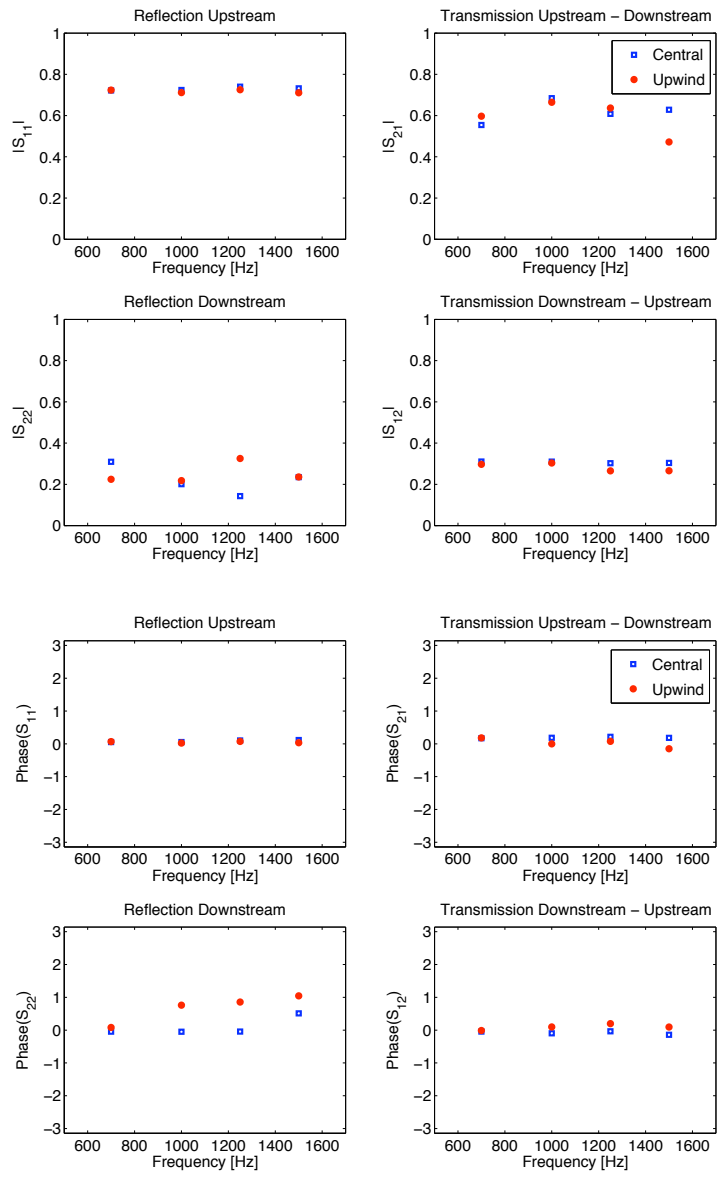
FIGURE 6.16. The scattering matrix computed with a blended (upwind and central) or a central discretization scheme. The top four figures are the amplitude and the bottom four are the phase.

6.3. Sensitivity to Boundary Conditions

6.3.1. *Slip vs No-Slip Duct Walls*

When the acoustic velocity is averaged over a duct cross-section it is assumed that it is constant, i.e. that there are no effects from the wall where it physically is zero. For acoustic calculations it is therefore preferable to use a slip boundary condition at the duct wall. Using slip walls also reduces the required mesh size, since no boundary layer has to be resolved, whereby a substantial reduction of the computational time is attained.

In Figure 6.17 and 6.18 it can be observed that having a slip, instead of a no-slip, boundary condition on the duct wall has some influence on the flow field next to the wall and close to the orifice. With a no-slip duct the flow turns to the orifice a bit earlier, so a small circulation zone appears in the corners in front of the plate. Downstream of the plate the duct wall boundary condition affects the characteristics of the recirculation zone.

The scattering matrix has been computed with slip and no-slip duct walls and the results are compared in Figure 6.19. It shows that using slip walls seems to reduce some of the noise in the result, but it does not change the average level of the reflection and transmission coefficients. This effect could be due to the averaging over cross-sections that is performed, but there can also be an effect from the shorter simulation time in the no-slip simulation. The result does however show that the scattering by the considered object is not sensitive to the duct wall boundary condition.

The influence of the plate wall boundary condition has been investigated by simulating the scattering with slip and no-slip plate walls, respectively. The result, shown in Figure 6.20, indicates that enforcing a zero velocity at the wall does not significantly change the scattering compared to using slip plate walls. The difference that can be observed between the two results is due to noise. The explanation for the observed insensitivity to the plate boundary condition is the sharp plate edges.

6.3.2. *Influence of Inlet Mach Number*

The scattering by an object is influenced by the flow around it and therefore by the Mach number. The scattering matrix has been computed for two different inlet Mach numbers, 0.1 and 0.08, with the short duct. The result is shown in Figure 6.21, where it can be observed that the Mach number significantly influences the amplitude of the scattering, while there is no clear effect on the phase. The different noise levels in the results are within the uncertainty due to a shorter simulation time for the lower Mach number. The results show that increasing the inlet Mach number increases the reflection and decreases the transmission, in accordance with the measurements and the model presented in Allam & Åbom (2005).
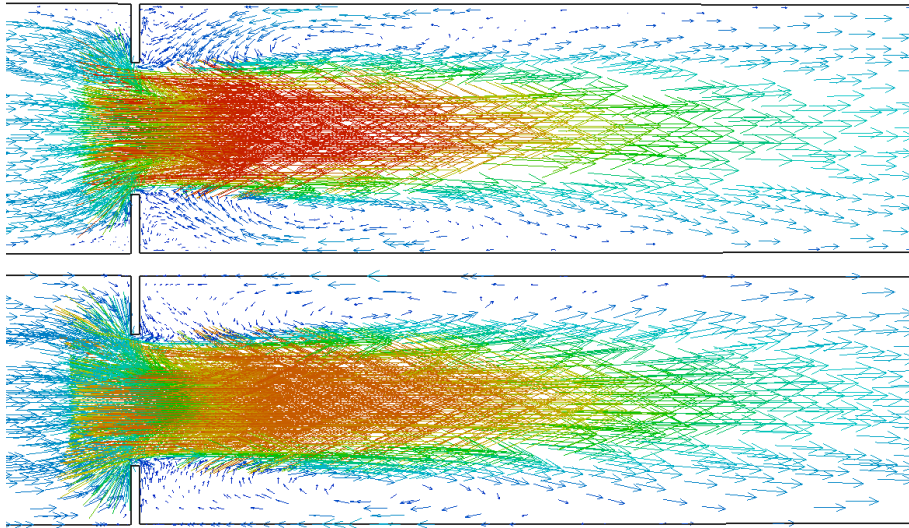
FIGURE 6.17. In-plane velocity vectors with no-slip duct walls at the top and with slip duct walls at the bottom.
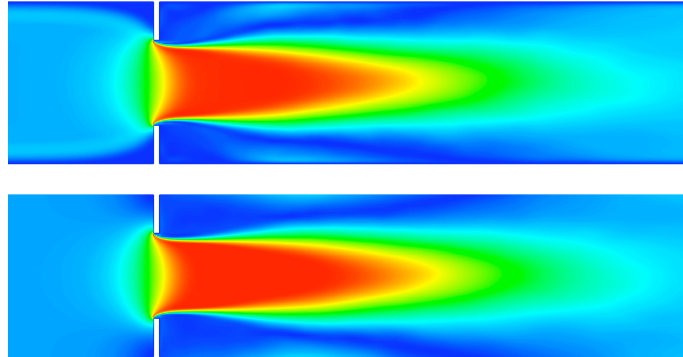
FIGURE 6.18. Mean velocity with no-slip duct walls at the top and with slip duct walls at the bottom.
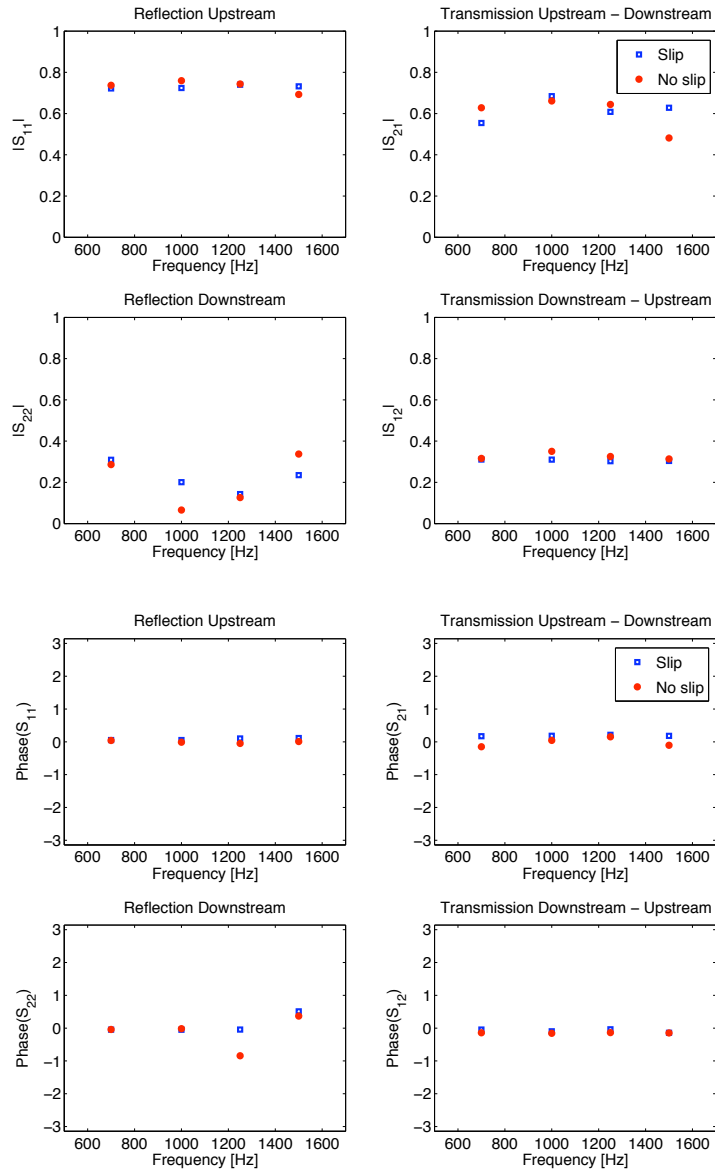
FIGURE 6.19. The scattering matrix computed with a slip or no-slip duct wall boundary condition. The top four figures are the amplitude and the bottom four are the phase.
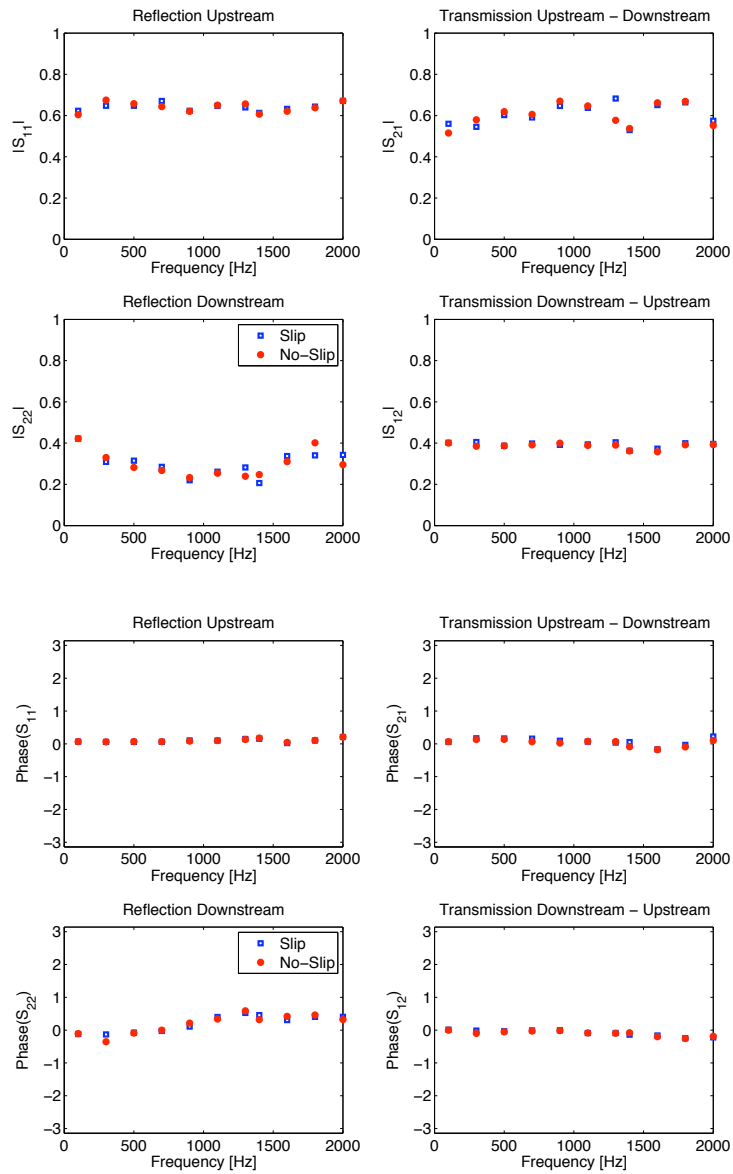
FIGURE 6.20. The scattering matrix computed with a slip or no-slip plate wall boundary condition. The top four figures are the amplitude and the bottom four are the phase.
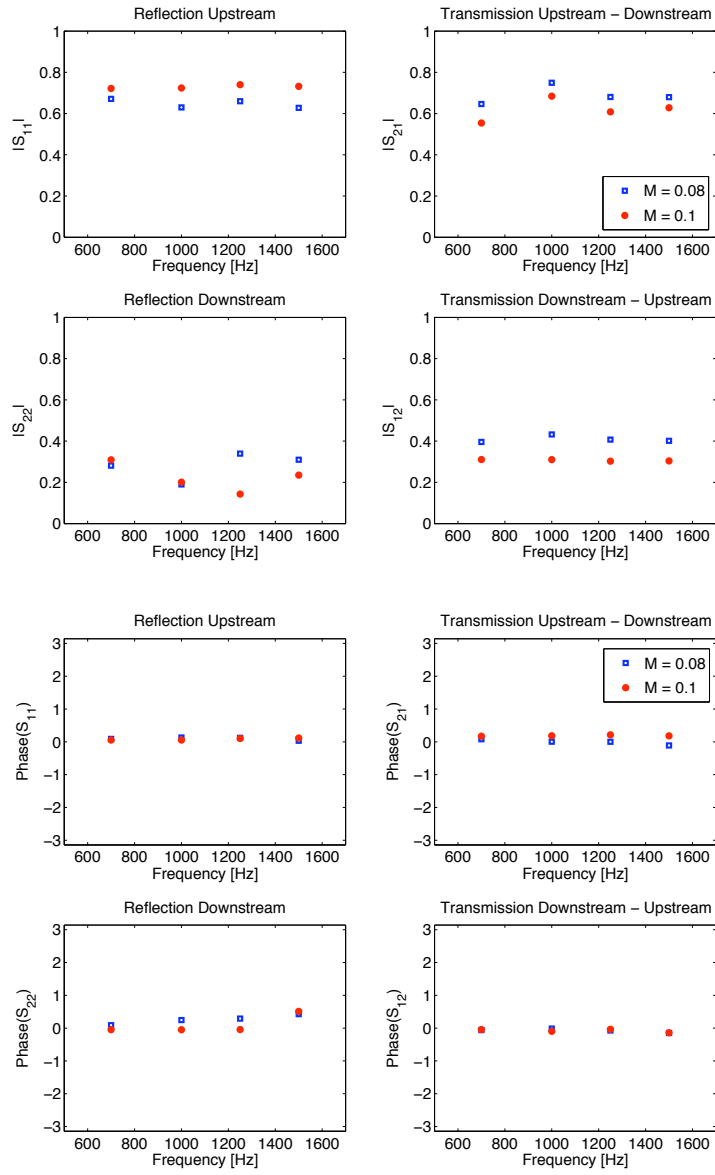
FIGURE 6.21. The scattering matrix computed with two different inlet Mach numbers. The top four figures are the amplitude and the bottom four are the phase.

FIGURE 6.22. Position of the planes used for evaluating the
post-processing methods. The distance between two planes is
either 5 cm or 10 cm, depending on the position. The planes
are numbered in successive order, i.e. the first upstream plane
is number 1 and the first downstream plane is number 11. The
figure is not to scale.

6.4. Effect of Flow Noise Suppression Methods

The flow will contain both acoustic and turbulent fluctuations and when the
acoustics is studied it is important to be able to accurately suppress the flow
noise and extract the acoustic waves. When waves are excited externally it is
also important to distinguish them from the flow generated sound. In LES this
is further complicated by short time series due to long simulation times. The
methods used and tried for extracting the acoustic waves have been described in
Section 4.4. Here the result of an evaluation of the different methods used and
their influence on the signal and the resulting scattering matrix is presented.

The evaluation of some of the noise suppression methods has been per-
formed with fluctuations corresponding to an analytical wave added to the
flow fluctuations from a LES of the flow through the orifice plate at an inlet
Mach number of 0.08. The analytical wave is created as a sum of sine waves
for first the case of an upstream and then a downstream excitation. For each
sine wave the up- and downstream wave components are calculated at each
evaluation cross-section, using a defined excitation amplitude and scattering
matrix, the sound and flow speeds from the simulation, the cross-section po-
sitions and assuming non-reflecting in- and outlet boundaries. At each plane
the sum of the fluctuations corresponding to each sound wave is calculated
and used to determine the acoustic pressure and velocity fluctuations using the
inverse of Equation (3.22). Finally these acoustic fluctuations are added to
the flow fluctuations from the simulation and the evaluation of the scattering
matrix is performed using all steps described in Section 4.4.

The position of the planes used for this evaluation, compared to the position
of the orifice and the domain boundaries, can be seen in Figure 6.22. The
distance between two adjacent planes is either around 5 cm or 10 cm depending
on the position of the planes. The inlet is situated 0.87 m upstream of the
orifice, the first upstream plane is 0.8 m from the orifice and the last upstream
plane is 0.1 m from the orifice. The first downstream plane is situated 0.2 m
downstream of the orifice, the last downstream plane is 1.6 m from the orifice

and the outlet is 2 m from the orifice. The planes are numbered in successive order, which means that the first upstream plane is number 1 and the first downstream plane is number 11.

6.4.1. *Excitation Amplitude*

The theoretical lower limit for the excitation amplitude, when extracting externally excited waves, has been investigated with the analytical waves. The full evaluation of the scattering matrix has been performed with different amplitudes of the analytical waves. The result can be seen in Figure 6.23, which shows that as the amplitude is decreased the random error increases. It can further be observed that the biggest problem occur for the transmission from up- to downstream and for the downstream reflection.

In reality the amplitude cannot be set arbitrarily high, since it will lead to non-linear effects, where the result is dependent on the excitation amplitude and the method used no longer is valid. However, in Figure 6.23 it was shown that rather high amplitudes are required for each frequency component, which can result in high total amplitudes for the acoustic variables when the component are added together. To check for non-linear effects the scattering matrix has been simulated in the long duct with three different total excitation amplitudes. The highest total amplitude has the highest amplitude for each frequency component and all frequencies are in phase. The cases with lower total amplitudes have a lower amplitude per frequency component and the components are randomly phase shifted. The case with the lowest total amplitude also has fewer simulated frequencies. The results, which can be seen in Figure 6.24, show that non-linear effects are a problem, since the result depends on the excitation amplitude and a higher excitation amplitude gives a ”noisy” frequency dependence. This is due to energy being transferred between different harmonics and all excited frequencies are harmonics of the lowest frequency, which is 100 Hz. That the amplitude dependent noise is not flow noise is clear for two reasons. The first is that a higher amplitude should reduce the flow noise, which also was seen for the analytical waves. The other one is that it is strong in the upstream reflection, which is insensitive to flow noise, due to the smooth upstream flow. As the amplitude is reduced the non-linear effects are reduced and since the present non-linearities do not seem to significantly influence the level of the elements it is assumed that the lowest excitation level used can be considered linear.
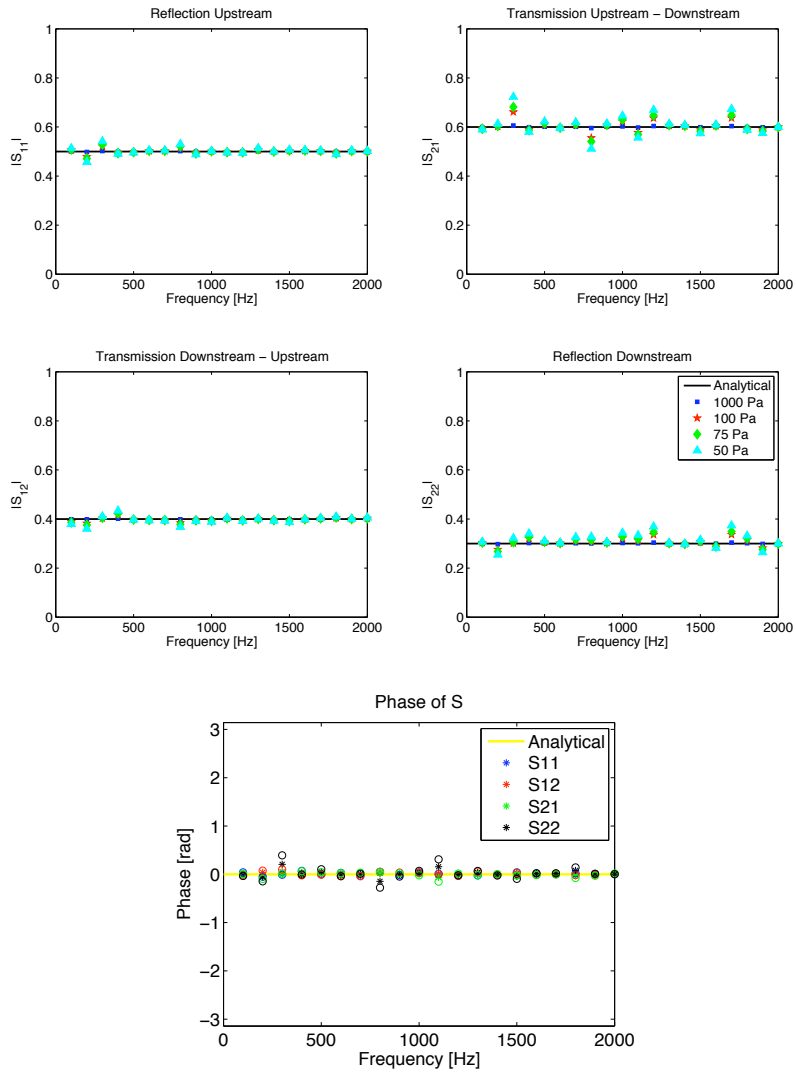
FIGURE 6.23. The scattering matrix of analytical waves added to a flow field for different wave amplitudes. The amplitudes given are per frequency component. The amplitude is shown in the top four figures. The bottom figure shows the phase, where star symbols are for a 100 Pa amplitude and circles are for a 50 Pa amplitude.
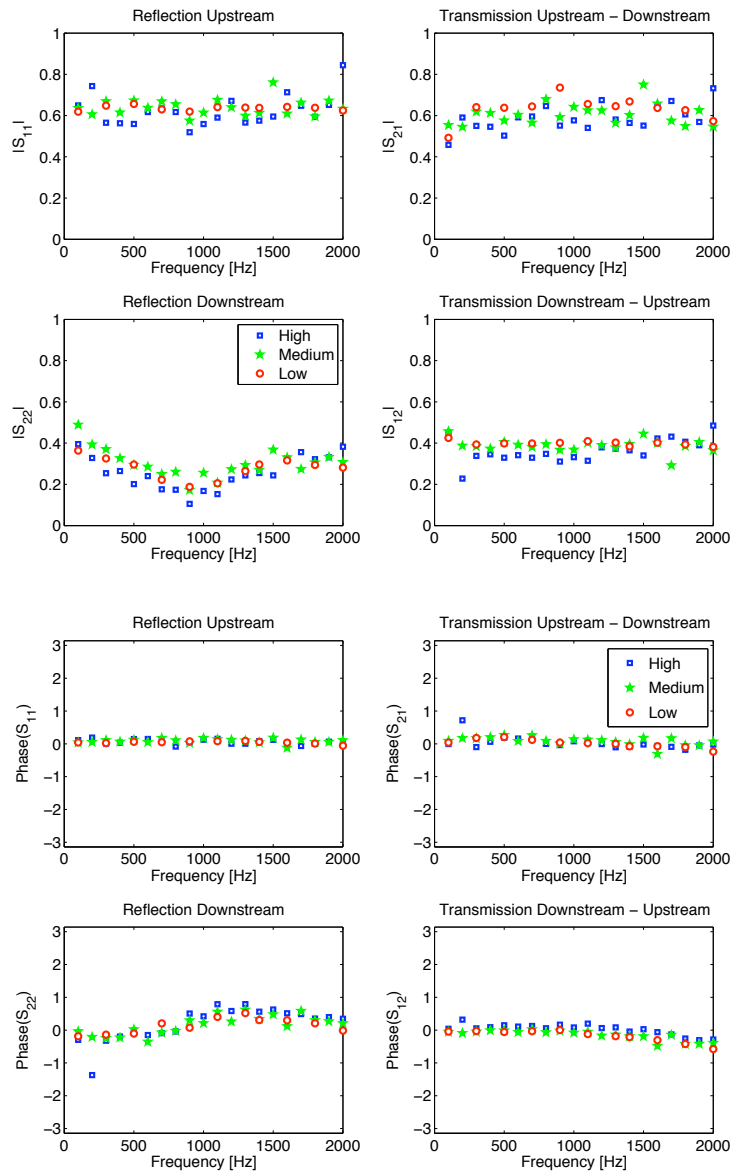
FIGURE 6.24. The scattering matrix from three simulations with different excitation amplitudes. The top four figures are the amplitude and the bottom four are the phase.

A measure for non-linear effects can be expressed in terms of the amplitude of the velocity fluctuations relative to the mean velocity in the orifice. The mean velocity in the orifice is 122 m/s and without excited waves the maximum amplitude of the velocity fluctuations is around 1.5 m/s. The velocity fluctuations from the highest excitation amplitude can be seen in Figure 6.25. It can be observed that the maximum acoustic velocity is above 15 m/s, which means that it is at least 12 % of the mean velocity at the orifice. For the medium amplitude case the maximum velocity fluctuations are around 7 m/s, which is just below 6 % of the mean velocity. For the lowest amplitude case the maximum velocity fluctuations are below 4 m/s, which is around 3 % of the mean velocity. These results indicate that non-linear effects start to appear when the amplitude of the acoustic velocity fluctuations becomes higher than around 1 % of the mean velocity. This can be compared with the low Mach number measurements performed by Testud *et al.* (2009), for which non-linear effects did not appear until the r.m.s. acoustic fluctuations became around 10 % of the mean velocity.
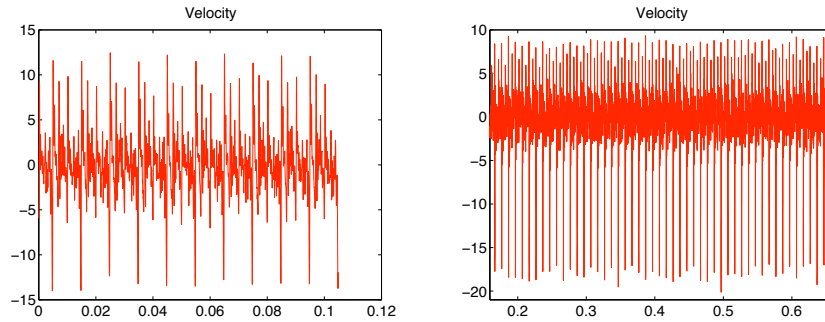
FIGURE 6.25. Axial velocity fluctuations in the middle of the orifice for the highest amplitude case. The left figure shows the result for upstream excited waves and the right figure shows the result for downstream excited waves.
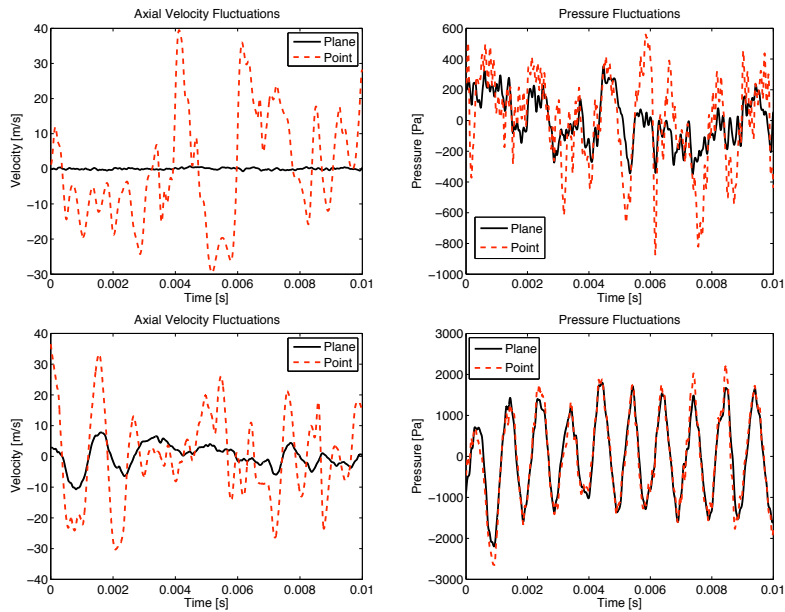
FIGURE 6.26. Comparison of the fluctuations at a point in the middle of the duct and the cross-section average fluctuations 2 dm downstream of the plate. From a simulation without externally excited waves at the top and with an externally excited 1000 Hz wave at the bottom.

6.4.2. *Cross-Section Average*

In the plane wave frequency range the acoustic pressure and velocity are constant at cross-sections of the duct. Turbulent fluctuations can then be reduced by calculating the cross-section average fluctuations. In Figure 6.26 the fluctuations at a point in the middle of the duct can be compared to the cross-section average fluctuations for the case of just a flow field and the case of an externally excited wave. It can be observed that much of the unwanted flow fluctuations are averaged away, especially for the velocity.

6.4.3. *Characteristics Based Filtering*

Fluctuations that do not propagate with the speed of sound are suppressed using the characteristics based filtering (CBF) method proposed by Kopitz *et al.* (2005). By averaging over a number of planes (duct cross-sections), using the acoustic propagation speed, non-acoustic disturbances, e.g. turbulence, are averaged away.

The evaluation of the CBF has been performed by calculating the scattering matrix for the analytical waves using different planes. The reason for using the analytical waves is that in the simulations the result might be influenced by other effects then flow disturbances, e.g. non-linear propagation or near field effects close to the orifice or boundaries. The resulting scattering matrix can be seen in Figure 6.27 for the variation of upstream planes, in Figure 6.28 for different downstream planes and in Figure 6.29 for different downstream plane combinations. The position of the planes in the duct can be seen in Figure 6.22.

Figure 6.27 show that varying the upstream planes does not affect the result, which is as expected since there is a uniform inflow and therefore no flow disturbances upstream of the plate. This means that the error compared to the analytical solution is due to flow generated noise at the studied frequencies, which is much more difficult to filter away. Figure 6.28 and 6.29 further show that except for at the plane closest to the orifice (approximately 2 dm downstream) there are no significant non-acoustic fluctuations at the downstream side either. This is probably due to the fact that the planes are situated downstream of the breakup of the jet, where the mesh is stretched implying that turbulent fluctuations are dissipated. Furthermore, the cross-section average has significantly reduced the turbulent fluctuations that are left. These results imply that as long as the plane is situated far enough downstream, where there are no significant non-acoustic (turbulent) fluctuations left in the simulation, the CBF method does not improve the result. However, if there are planes closer to the object, or if higher frequencies that require a finer grid spacing are studied, the CBF method will suppressing non-acoustic fluctuations.
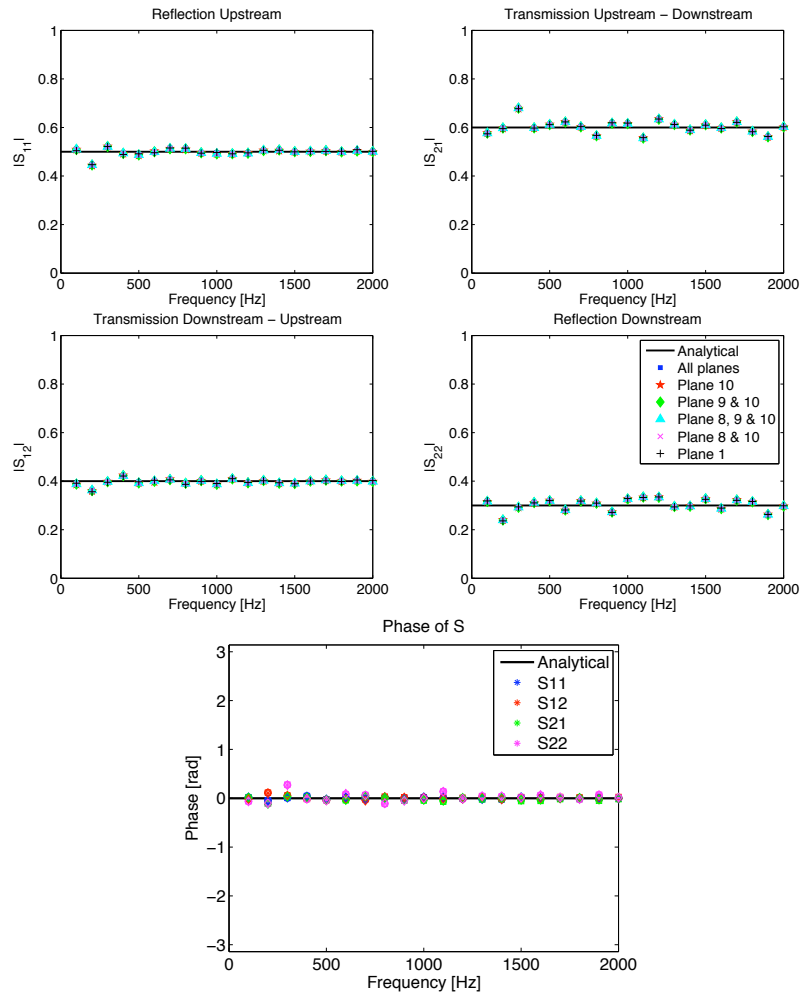
FIGURE 6.27. The scattering matrix for the analytical waves computed with different or averages of different upstream planes (and all downstream planes). The top four figures are the amplitude and the bottom is the phase, where star is all planes, circle is plane 10, square is plane 9 & 10 and diamond is plane 1
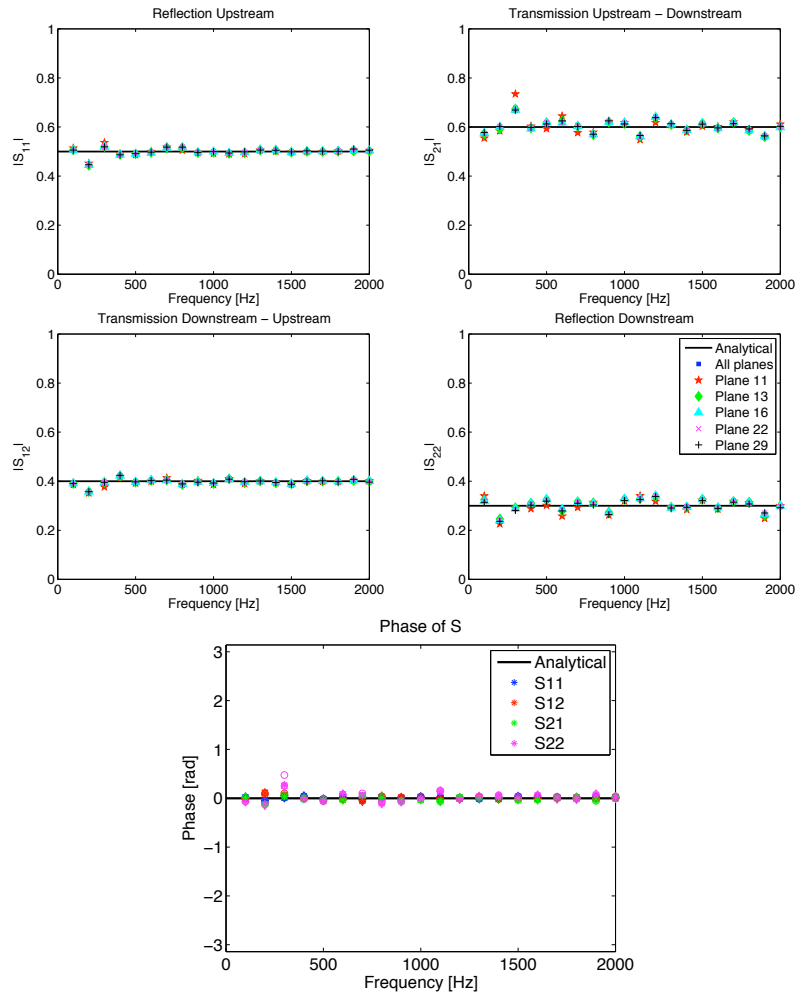
FIGURE 6.28. The scattering matrix for the analytical waves computed with different downstream planes (and all upstream planes). The top four figures are the amplitude and the bottom is the phase, where star is all planes, circle is plane 11, square is plane 13 and diamond is plane 29
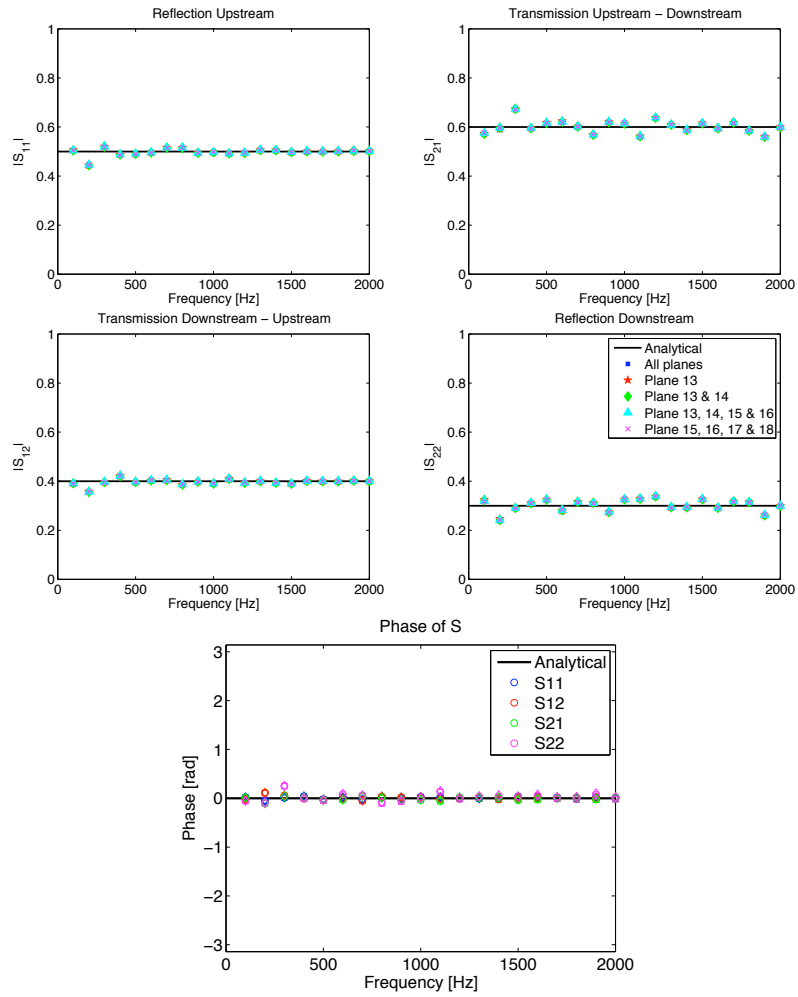
FIGURE 6.29. The scattering matrix for the analytical waves computed with different or averages of different downstream planes (and all upstream planes). The top four figures are the amplitude and the bottom is the phase, where star is all planes, circle is plane 13, square is plane 13 to 16 and diamond is plane 15 to 18.

6.4.4. *Phase Averaging*

Phase averaging, also called synchronized time domain averaging, is an efficient way to suppress noise when discrete frequencies are studied. By averaging over one period of the wave, fluctuations that are not at that frequency or harmonics of it, or that have a non-constant phase, are eliminated. How good this elimination becomes depends on the number of periods used for the averaging. An example of the effect of phase averaging on the time signal can be seen in Figure 6.30 for different number of averages of a 1000 Hz analytical wave. It can clearly be observed that increasing the number of averages gives a time signal that looks more and more like a sine wave.

The scattering matrix calculated with different number of averages of the analytical waves can be seen in Figure 6.31. It can be observed that increasing the number of averages has a strong effect to start with, especially for the amplitude of the elements, but as the number of averages increase the visible effect decreases. It can further be observed that it is the downstream reflection and the transmission from up- to downstream that are most effected by the number of average used.

6.4.5. *Cross-Correlation with Excitation Signal*

The incoming, reflected and transmitted sound waves are correlated with the excitation signal, while the flow generated sound is assumed to be uncorrelated with it. It was therefore tested if calculating the cross-correlation between the sampled signals and the excitation signal improved the result compared to only using phase averaging, which has the same effect. Figure 6.32 shows a comparison between using the cross spectra or only synchronized time domain averaging for two different numbers of averages. It can clearly be seen that using the cross spectra does not influence the result.
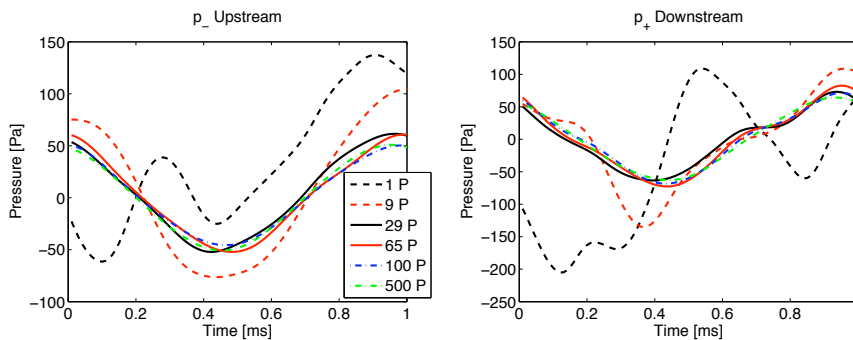
FIGURE 6.30. Phase averaging of an analytical 1000 Hz wave using different number of periods for the averaging.
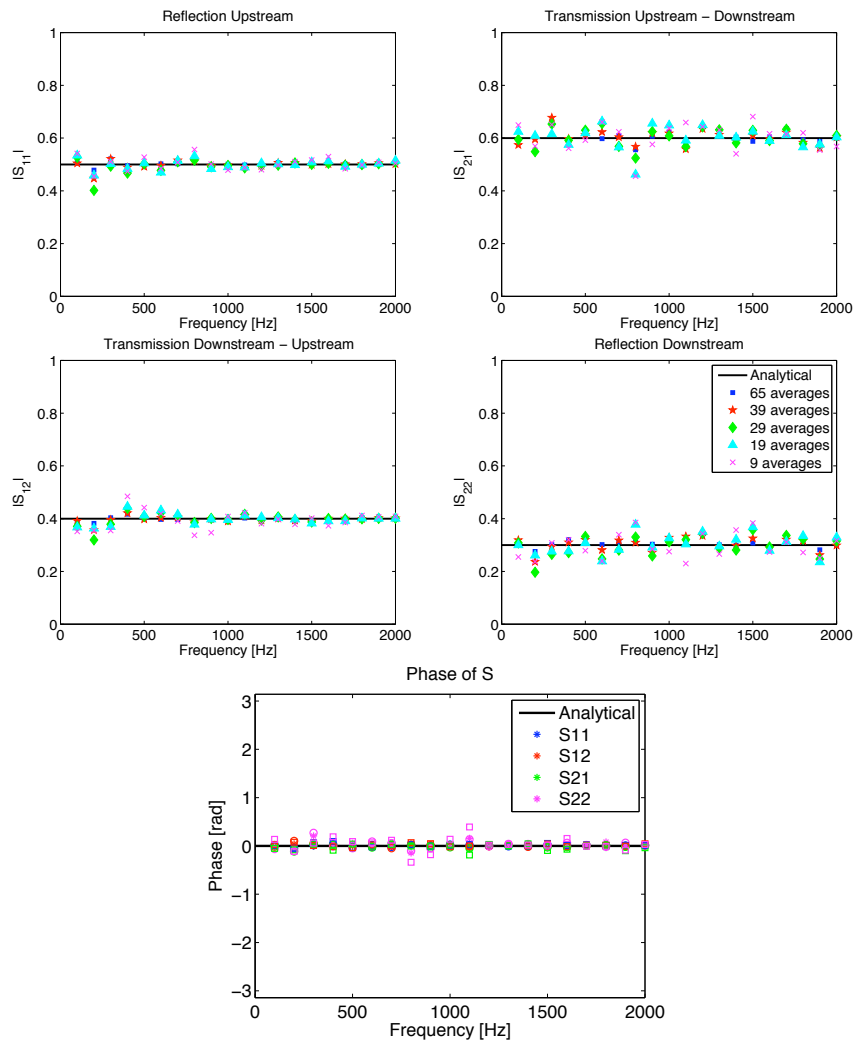
FIGURE 6.31. The scattering matrix calculated with different number of averages of the analytical wave. The top four figures are the amplitude and the bottom is the phase, where star is 65 averages, circle is 39 averages and square is 19 averages.
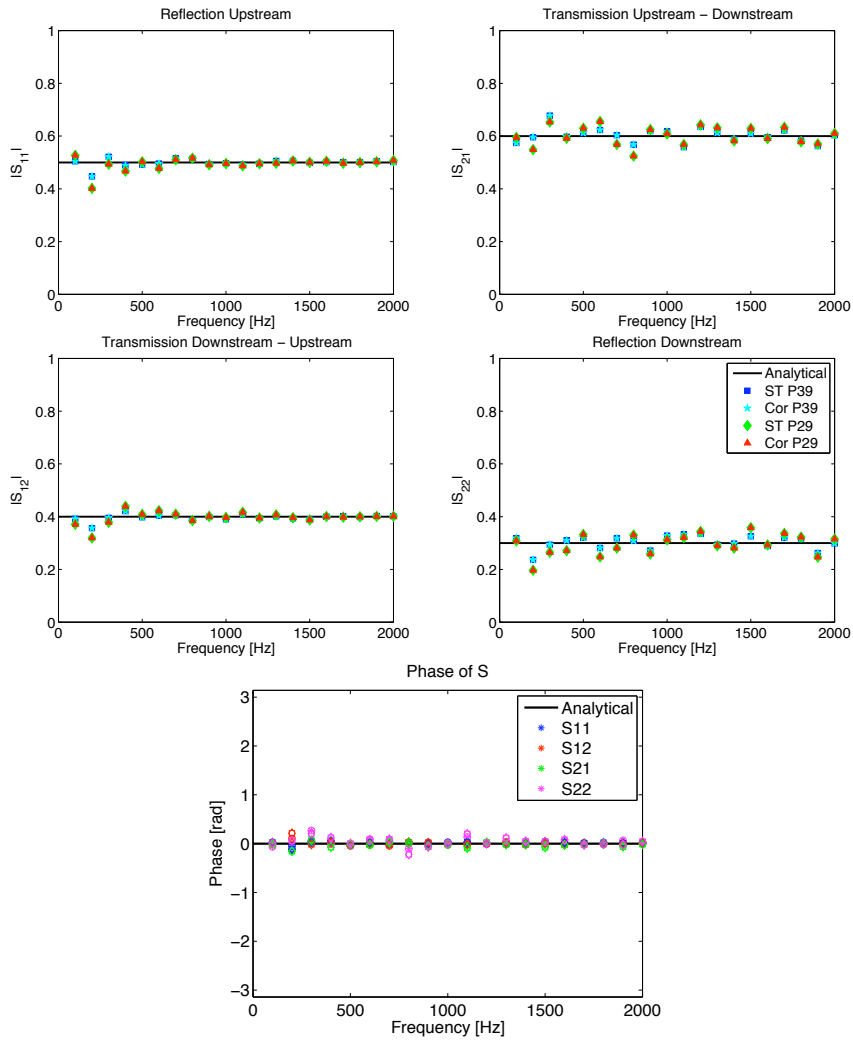
FIGURE 6.32. The scattering matrix calculated with the cross-spectra (Cor) between the sampled signals and the excitation signal or only synchronized time domain averaging (ST), for 39 or 29 averages. The top four figures are the amplitude and the bottom figure is the phase, where star is ST P39, circle is Cor P39, square is ST P29 and diamond is Cor P29.

6.5. Comparison with Measurements and Theory

The computed scattering has, for an inlet Mach number of 0.08, been compared to measurements and theory by Allam & Åbom (2005), which is summarized in Section 3.7.1. To reduce flow noise the scattering matrix has been computed in the longer duct and with thirty phase averages. Figure 6.33 shows the amplitude and the phase and Figure 6.34 shows the real and the imaginary parts of the elements compared to measurements and theory, where the latter only gives the real part.

The simulations show reasonable agreement with the measurements for the amplitude of the scattering matrix elements and for the phase of some of the elements, see Figure 6.33. However, while the amplitude of the downstream coefficients agree very well with measurements, the upstream reflection and partly also the up- to downstream transmission become slightly higher than in the measurements. Possible explanations for this discrepancy are discussed below.

The discrepancy observed for the phase in Figure 6.33 is due to the measurements having a phase dependency not seen in the simulations. Studying the real and imaginary parts of the elements, Figure 6.34, also show a phase variation in the measurements that is not observed in either the simulations or the theory, where the latter is completely frequency independent. This indicates that there is a problem with the phase in the measurements. The phase is however the most difficult parameter to determine accurately, since it involves moving the elements from the measuring position to the object. This procedure has been shown to be sensitive to the Mach number (Holmberg 2010), which is easier to retrieve from a simulation than a measurement, and a small error could result in the observed frequency dependence.

If the amplitudes of the scattering matrix elements are studied in Figure 6.33 it is clear that there is a very good agreement between simulations and measurements for the downstream coefficients, while the upstream coefficients are moderately higher in the simulations. Studying the theory, shown in Figure 6.34, it is observed to agree well with the measured upstream coefficients, while it proposes slightly higher values for the downstream coefficients. This discrepancy could be due to compressibility effects that are neglected in the theory, but clearly are present in the flow due to the high jet Mach number, see Section 6.1. The compressibility could also influence the elements connected with upstream excited waves, but it is not likely to explain the discrepancy between the simulations and the measurements.

Even though the theory has some problems due to neglecting compressible effects, it might be used to get an idea of what could cause a discrepancy between the computed and measured results. According to the theory the reflection and the transmission coefficients are the same from both directions and depend on the parameter MC_L, where M is the inlet Mach number and

C_L is the pressure loss coefficient over the plate. When the parameter MC_L is decreased the reflection is also decreased, while the transmission is increased. The discrepancy in the amplitude can therefore not be explained directly by the trends predicted by the theory. The Mach number was in Section 6.3.2 shown to affect the solution in accordance with the theory, so an error in the Mach number would not explain the observed discrepancy. The pressure loss over the plate was in Section 6.1 shown to be slightly higher in the simulations than the theoretical value, but not enough to bring the theoretical reflection up to the simulated one. Furthermore, it has not been possible to test the effect of changing the pressure loss without changing the Mach number, since it would involve moderately rounding the corners of the orifice.

The fact that both the reflection and the transmission of waves coming from the upstream direction become too high indicates that less of the acoustic energy is converted to vorticity in the simulations and/or that there is less dissipation. The dissipation in the duct should however be small at least for the lowest frequencies, which implies that it is the dissipation at the plate that is interesting. Furthermore, the conversion of acoustic energy is better captured for waves coming from the downstream direction. This dependency on propagation direction could be explained by the acoustic wave seeing the geometry differently from the two directions due to the flow field. A wave coming from the upstream side clearly impinges on the upstream edge of the orifice, while the jet, with the vena contracta effect, partly hides the downstream edge from downstream excited waves. Errors in the prediction of the interaction between the wave and the sharp edge could therefore give a larger effect for waves coming from the upstream direction. An insufficient grid resolution at the plate could account for this effect, but since a grid refinement of this area did not significantly affect the result, see Section 6.2.1, it does not seem to be the cause for the discrepancy. It can further be considered that both the conversion of acoustic energy to vorticity and the dissipation of acoustic energy are governed by viscous effects. The physical viscosity should be the same in the measurements and the simulations, but if the artificial dissipation that is added to the LES is too low it might influence the result. However, a simulation with the more dissipative blended (upwind and central) discretization scheme did not seem to significantly influence the result, see Section 6.2.2.

There are also other possible effects that could influence the result. One is non-linearities, which were shown to be a problem in Section 6.4.1, but decreasing the amplitude did not show a trend that would explain the too high upstream coefficients. Startup effects can also influence the result, since it is difficult to ensure a totally statistically steady state case with short simulation times and totally reflecting boundaries, but it has been tested to vary the amount of data neglected at the start without a significant effect. It is also possible that the data extraction is too close to the orifice and therefore still in

the near field. However, this effect should be frequency dependent and varying the planes used for the post processing did not indicate that this factor is significant. Another possibility is that the lack of disturbances in the simulated upstream flow affected the result. However, Kierkegaard *et al.* (2008) performed linear 2D simulations of the scattering by the same geometry (using the mean flow from another simulation) with very good results compared to the measurements at a lower Mach number ($M = 0.054$). The difference in the scattering matrix could then come from differences in the mean flow, but they should be smaller than the differences due to slip or no-slip duct walls that were shown not to be important in Section 6.3.1. The fact that the linear 2D simulations by Kierkegaard *et al.* (2008) gave good results then imply that the discrepancy has to do with the interaction between the wave and the orifice plate.
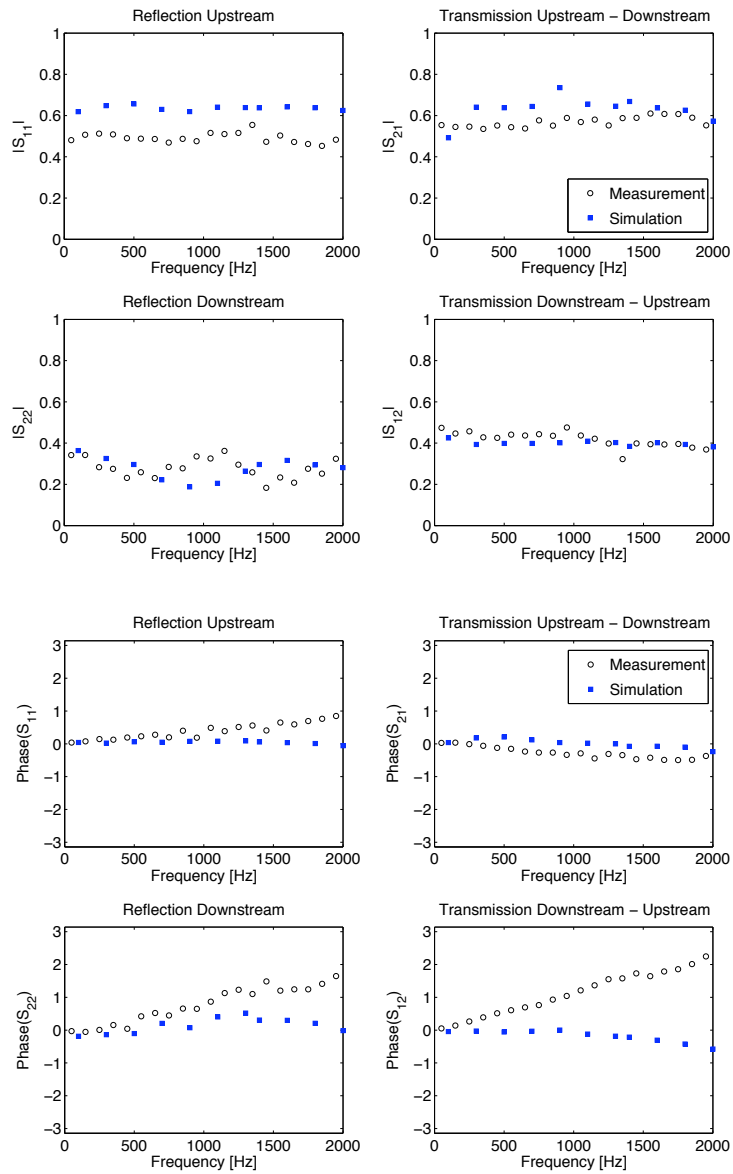
FIGURE 6.33. The scattering matrix compared with measurements. The top four figures are the amplitude and the bottom four are the phase.
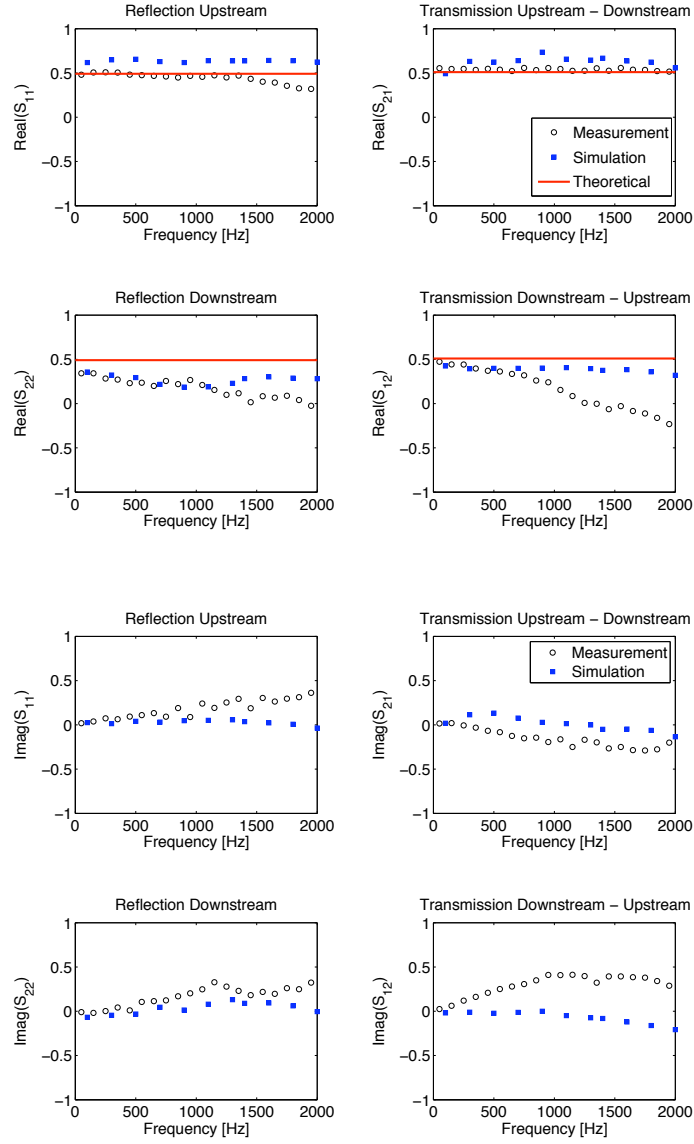
FIGURE 6.34. The scattering matrix compared with measurements and theory. The top four figures are the real parts and the bottom four are the imaginary parts of the elements.

CHAPTER 7

1D Results

In this chapter the results of 1D CFD simulations with the commercial software GT-Power are presented. The aim is to investigate the limitations in computing the scattering of acoustic waves with a 1D CFD tool for engine simulations. The scattering has been computed both for the orifice plate studied with LES and for a turbocharger compressor.

7.1. Orifice Simulations

Here the results from the 1D simulations of the scattering by an orifice plate are presented. The geometry is the same as in the 3D simulations presented in chapter 6, i.e. it is a circular duct with a diameter of 57 mm and a 2 mm thick orifice plate with an area contraction ratio of 0.28. The simulations have been performed with the inlet Mach numbers 0.080 and 0.054. The results are presented in form of the scattering matrix, where the upstream coefficients correspond to the upstream reflection and the up- to downstream transmission and the downstream coefficients correspond to the downstream reflection and the down- to upstream transmission.

The results from the 1D simulation with specified orifice thickness and recommended discharge coefficient are compared to measurements in Figure 7.1 and 7.2, for the inlet Mach numbers 0.08 and 0.054, respectively. For the phase of the scattering matrix the 1D simulations agree well with the measurements, with the exception of the downstream transmission at the higher Mach number. This discrepancy has also been found for the 3D LES, where it has been argued that the phase is the most difficult parameter to determine accurately, since it involves moving the elements from the measuring position to the object. This procedure is sensitive to the Mach number, which is easier to retrieve from a simulation than from a measurement, and a small error could result in the observed frequency dependence. For the amplitude of the reflection there is a poor agreement with the measurements, except for at very low frequencies at the higher Mach number. For the amplitude of the transmission coefficients the agreement is somewhat better. A clear frequency dependence, which is stronger for the lower Mach number case, can be observed in the simulations, while the measurements are frequency independent. The 3D LES results presented in Chapter 6 and theory by Allam & Åbom (2005), which is summarized

in Section 3.7.1, also suggests that the scattering should be frequency independent, indicating a problem with the 1D simulations. In an attempt to find a cause for the observed discrepancy some parameters have been varied in the simulations, for the inlet Mach number 0.08, as described below.

To make sure that the problem setup is linear, simulations have been performed for two excitation amplitudes. The result, which can be seen in Figure 7.3, show that the problem is linear for the used excitation amplitude.

A parameter that can influence the result is the discharge coefficient, which is connected to the vena contracta of the orifice. In Figure 7.4 the result from slightly varying the discharge coefficient around its recommended value of 0.8 can be seen. It can be observed that the discharge coefficient only has an influence on the amplitude of the elements and that the effect is slightly larger for lower frequencies. It can also be observed that an error in the discharge coefficient would not explain the discrepancy compared to the measurements. Furthermore, the effect of varying the discharge coefficient is as expected, where a higher value gives a lower reflection and a higher transmission, since it indicates that the orifice edges are more rounded.

Another parameter that can influence the result is the orifice thickness. In the above simulations it has been set to the physical thickness of 2 mm. However, in the software used it is recommended to neglect the thickness for thin orifices. A simulation with neglected orifice thickness was therefore performed. The discharge coefficient was in this case set to default, which is the recommended option for 0 thickness orifices. The result, shown in Figure 7.5, indicates that neglecting the thickness might be better than specifying it, since it removes most of the frequency dependence seen in the amplitude, while it does not significantly change the phase of the elements. However, the level of the amplitudes becomes wrong, with too large reflections and too low transmissions, indicating that the discharge coefficient has to be specified to a higher value than the default. At the same time, the discharge coefficient affect the mean pressure drop over the orifice and it might not be desirable to change this.
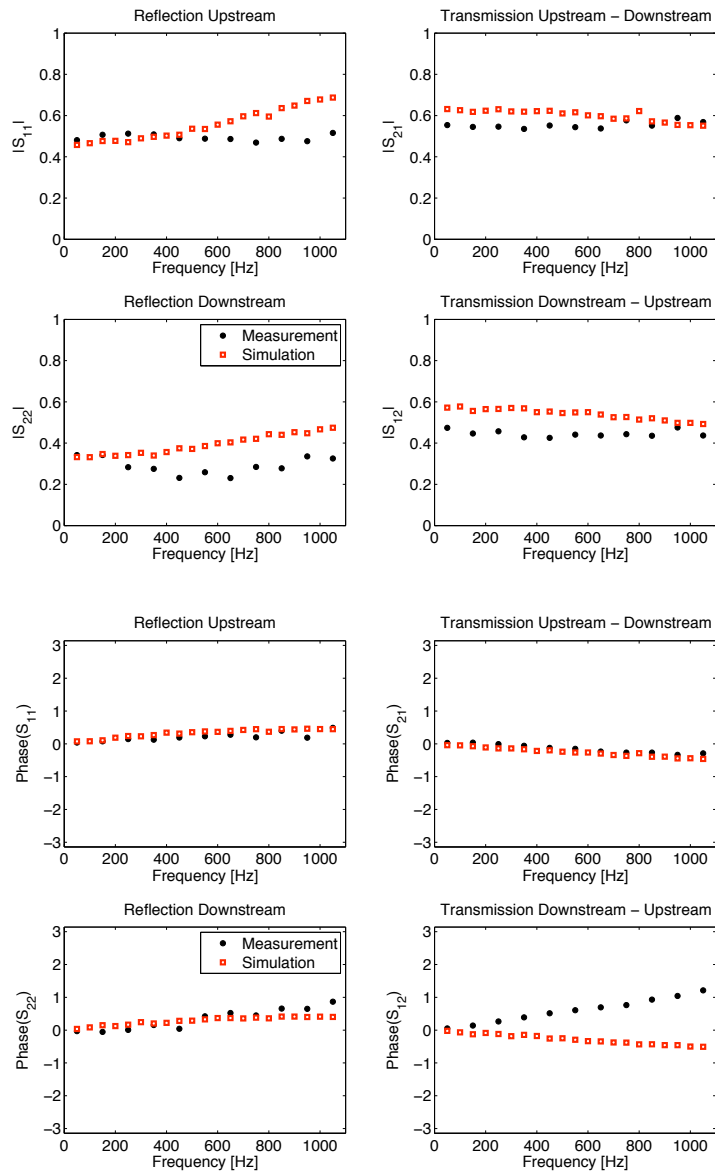
FIGURE 7.1. The orifice scattering matrix at an inlet Mach number of 0.08, computed with 1D simulations, compared to measurements. The top four figures are the amplitude and the bottom four are the phase.
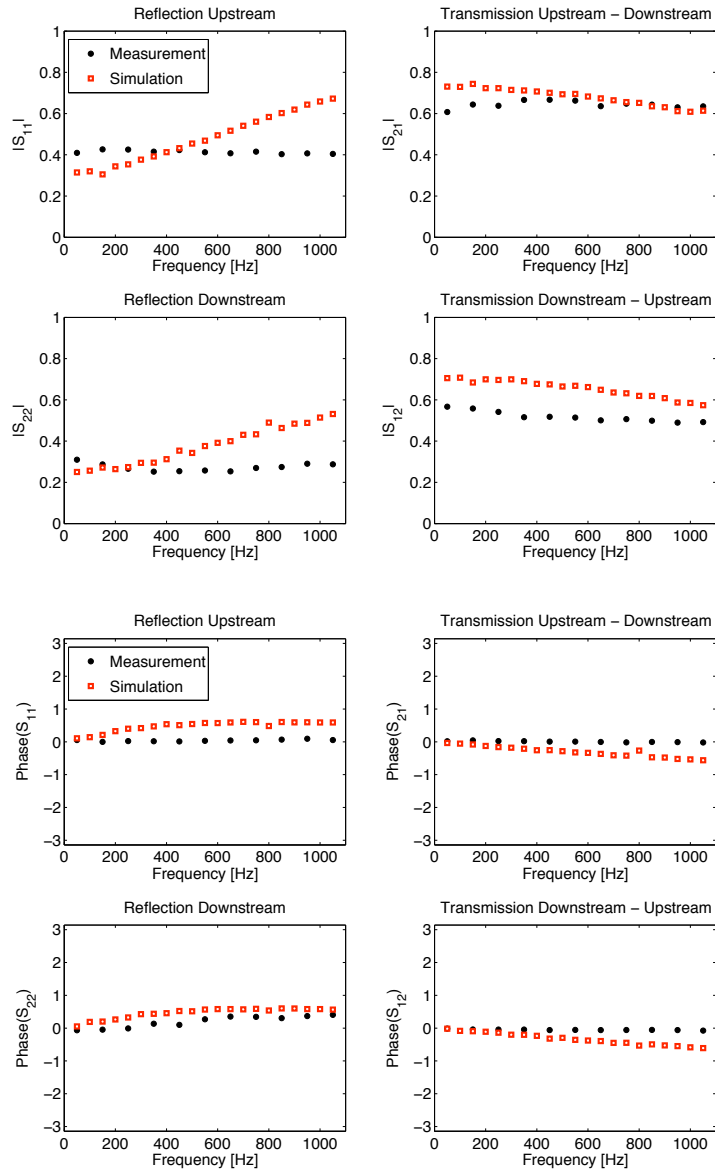
FIGURE 7.2. The orifice scattering matrix at an inlet Mach number of 0.054, computed with 1D simulations, compared to measurements. The top four figures are the amplitude and the bottom four are the phase.
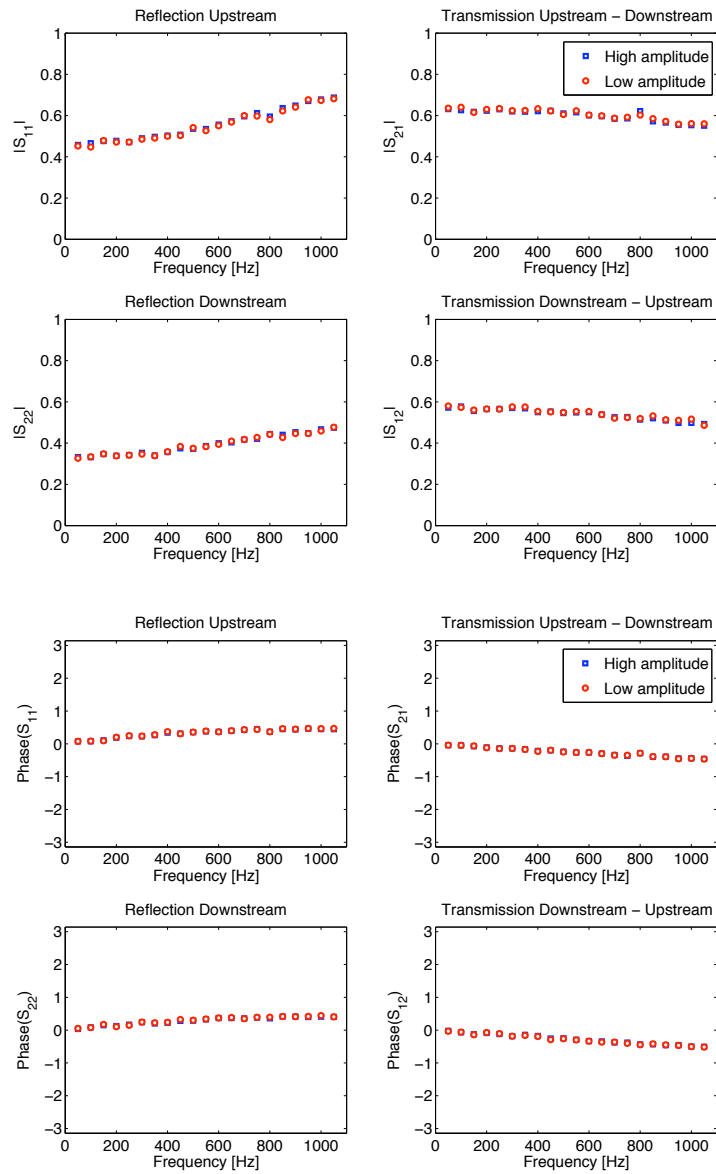
FIGURE 7.3. The orifice scattering matrix computed with 1D simulations and two different excitation amplitudes at an inlet Mach number of 0.08. The top four figures are the amplitude and the bottom four are the phase.
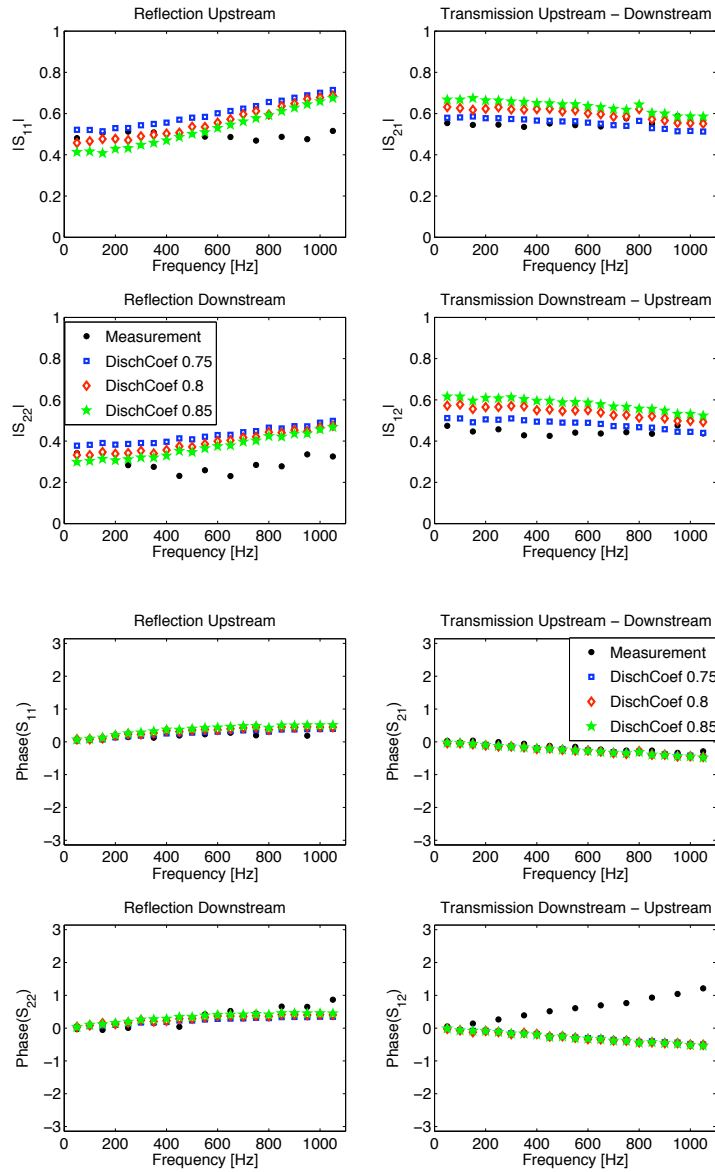
FIGURE 7.4. The orifice scattering matrix computed with 1D simulations with different discharge coefficients (where 0.8 is the recommended) at an inlet Mach number of 0.08, compared to measurements. The top four figures are the amplitude and the bottom four are the phase.
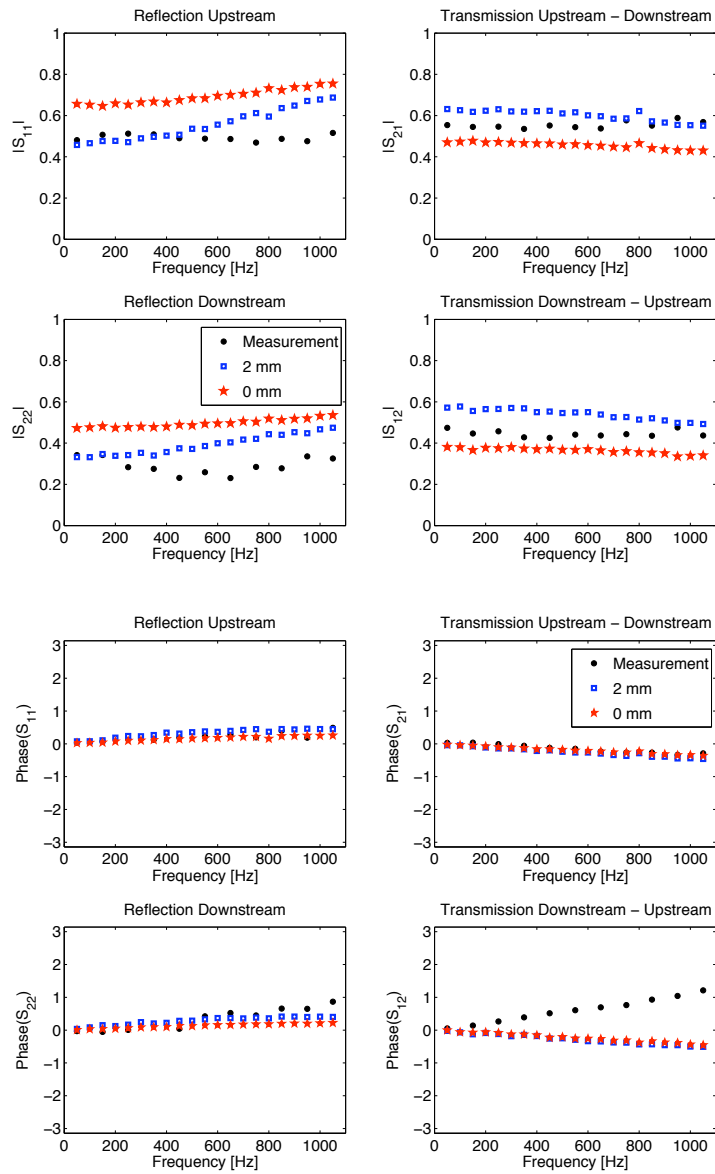
FIGURE 7.5. The orifice scattering matrix computed with 1D simulations with the plate thickness either neglected or set to the true 2 mm, compared to measurements. The top four figures are the amplitude and the bottom four are the phase.
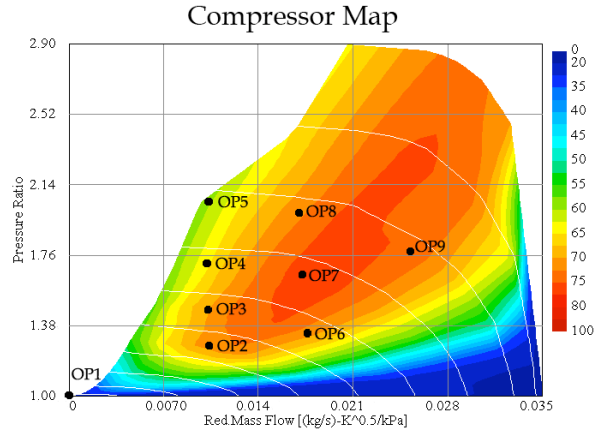
FIGURE 7.6. Compressor map for the Garret compressor, with the simulated operating points marked with black circles.

7.2. Compressor Simulations

Here the results from the 1D simulations of the scattering by a turbocharger compressor are presented in form of the transmission loss over the compressor. From an engine point of view the upstream transmission loss is the most interesting, since it gives the loss of acoustic power in the direction of propagation of the engine pulses generated at the cylinders. The downstream transmission loss is however interesting from an academical point of view and will also be considered.

To investigate the limitations of the 1D compressor model simulations have been performed at nine operating points of a Garret compressor, for which Tiikoja *et al.* (2010) have measured the scattering of acoustic waves. The simulated operating points can be seen together with the map of the Garret compressor in Figure 7.6. Simulations have been performed with the different model setups described in Section 5.4 and with a damped or un-damped map, i.e. the mass flow fluctuations in the map are either damped or not (using a built in damping function).

The first operating point is that for the compressor standing still without any mass flow. This is not a realistic operating point from an engine point of view, but it is interesting from an academic perspective. However, the code is not capable of handling this region of the map and the incoming waves are almost completely reflected, resulting in a very high transmission loss (over 100 dB). Therefore only the operating points two to nine are shown and discussed in the results presented below.
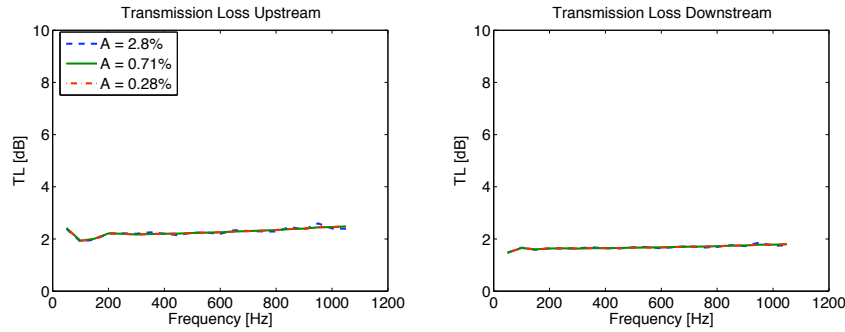
FIGURE 7.7. The transmission loss of the un-damped map computed with different excitation amplitudes, measured in per cent of the mean inlet velocity. Operating point four.

7.2.1. *Excitation Amplitude*

To make sure that the problem is in the linear regime the excitation amplitude has been varied. This was done for three different setups: the un-damped map, the damped map and the un-damped map with added volumes, since the linearity might be different for different elements and settings. The result for the un-damped map can be seen in Figure 7.7, which shows that map gives a linear response to the fluctuations at all tested excitation amplitudes. The result for the damped map can be seen in Figure 7.8, which shows that the damping introduces non-linearities that require a lower excitation amplitude than the un-damped map. The shown operating points (two and four) had the largest influence of the excitation amplitude, but the difference for the two lower amplitudes is assumed to be small enough to be neglected. Furthermore, the implementation of the added damping might be such that the problem never becomes completely linear. The results for the un-damped map with added volumes can be seen in Figure 7.9, for the two operating points (two and five) that were most affected by the excitation amplitude. It can be observed that the two lower amplitudes give the same result at operating point five, while it is the two higher amplitudes that give the same result at operating point two. This indicates that the highest excitation amplitude is too high for some operating points, while the lowest is too low (drowned by noise). However, the results indicate that the simulations with the medium amplitude can be considered linear.
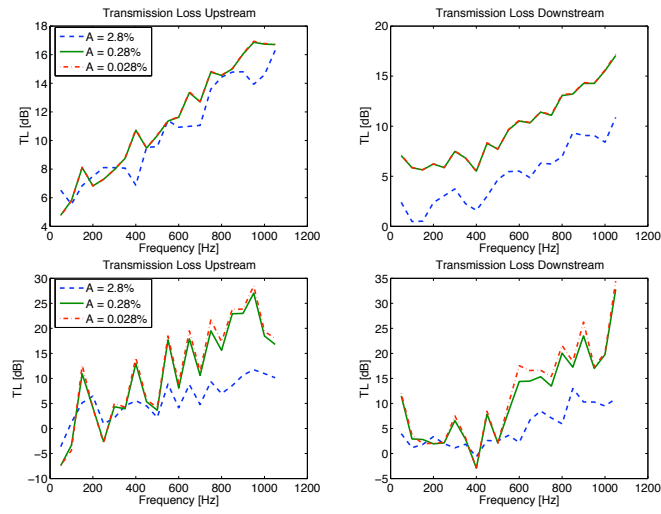
FIGURE 7.8. The transmission loss of the damped map computed with different excitation amplitudes, measured in per cent of the mean inlet velocity. The top and bottom figures are for the operating points two and four, respectively.
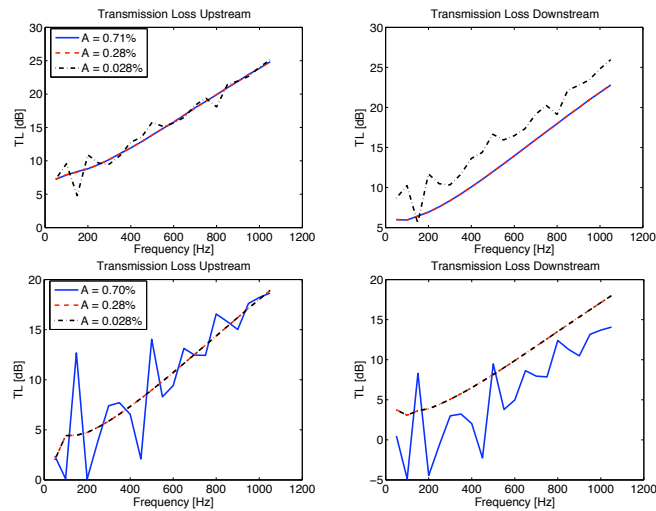
FIGURE 7.9. The transmission loss of the un-damped map with spherical volumes computed with different excitation amplitudes, measured in per cent of the mean inlet velocity. The top and bottom figures are for the operating points two and five, respectively.

7.2.2. *Transmission Loss of the Un-damped Map*

To investigate the effect of the operating point on the transmission loss, it has been compared to measurements for the setup with an un-damped map. The results, see Figure 7.10, show that the un-damped map gives a frequency independent transmission loss. In the measurements this is also the case for lower frequencies (up to around 500 Hz). However, there is a large discrepancy in the level of the transmission loss for most operating points. The exception is some operating points that show a reasonable agreement for either the up- or downstream transmission loss (never both), but there is no clear trend as to where in the map these points are located.

It is also of interest to study the trends of the simulation results, shown in Figure 7.10, due to changes in mass flow or pressure ratio. Increasing the mass flow results in an increased transmission loss, which is in agreement with the measurements. Increasing the pressure ratio, at constant mass flow, results in a decreased transmission loss, with the exception of operating point five. In the measurements this trend is only observed for the higher mass flow operating points (six to eight) and the effect is weaker. A reason for operating point five not following the trend has not been found, but it could be due to the point being so close to the surge line that it is crossed during part of the acoustic period. This means that the code has to extrapolate data to a region where no input data is available from the map.

7.2.3. *Effect of Model Setup*

As was observed in Figure 7.10, of the transmission loss of the un-damped map, the map is not capable of capturing the influence the compressor has on incoming pulsations. Simulations with different model setups, described in Section 5.4, where therefore performed. In these setups volumes (in the form of different type of elements) are added up- and downstream of the map, to take into account the volumes inside the compressor, as proposed by Rämmal & Galindo (2010), who successfully simulated the passive acoustic properties of a compressor using a 1D CFD code.

The effect of changing the model setup is presented in Figure 7.11 and 7.12 for simulations with the un-damped map. It can be observed that adding extra ducts to compensate for the volumes increases the transmission loss for operating point four and five, while it does not significantly affect the result for the other operating points. An increased transmission loss could be due to dissipation in the ducts, since the code has proven dissipative even when the wall friction is set to zero, but then it should be visible for all operating points. However, no other explanation has been found for the effect of the extra ducts. Adding volumes in the form of flow split elements results in an increased transmission loss with increasing frequency, but the level for the lowest frequencies is relatively unchanged compared to the results with only the map.
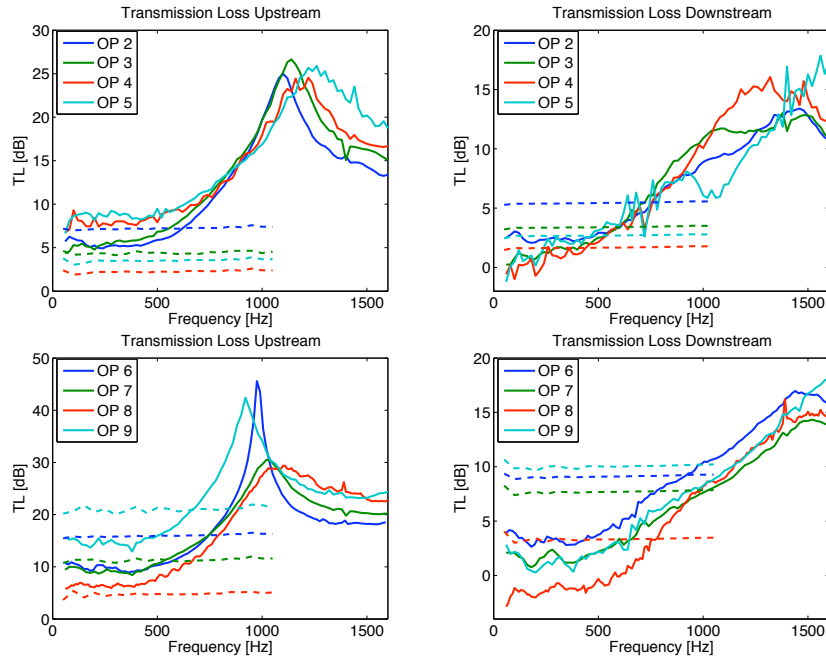
FIGURE 7.10. Comparison of the measured transmission loss and that computed with the un-damped map for the different operating points, which can be seen in Figure 7.6. Solid lines are measurements and dashed lines are simulations.

The general flow split element (FSplit) gives a slightly higher transmission loss than the spherical, but in general they produce the same result. Compared to the measurements the added volumes improve the result, but there is still a large discrepancy. This is due to the map giving the wrong level of the transmission loss and the frequency dependence introduced by the volumes being different than that observed in the measurements, especially for the upstream transmission loss.

7.2.4. *Effect of Damping Mass Flow Fluctuations in the Map*

To investigate the effect of damping the mass flow fluctuations in the map simulations with a damped map have been performed for the setup with only a map and for the setup with spherical flow split volumes. The results can be compared to measurements and simulations with an un-damped map in Figure 7.13 and 7.14, for the eight operating points. It can be observed that the damping increases the transmission loss for higher frequencies and that the effect is stronger for operating points in map regions with flat speed lines, which is as expected. The damping also introduces significant scattering in
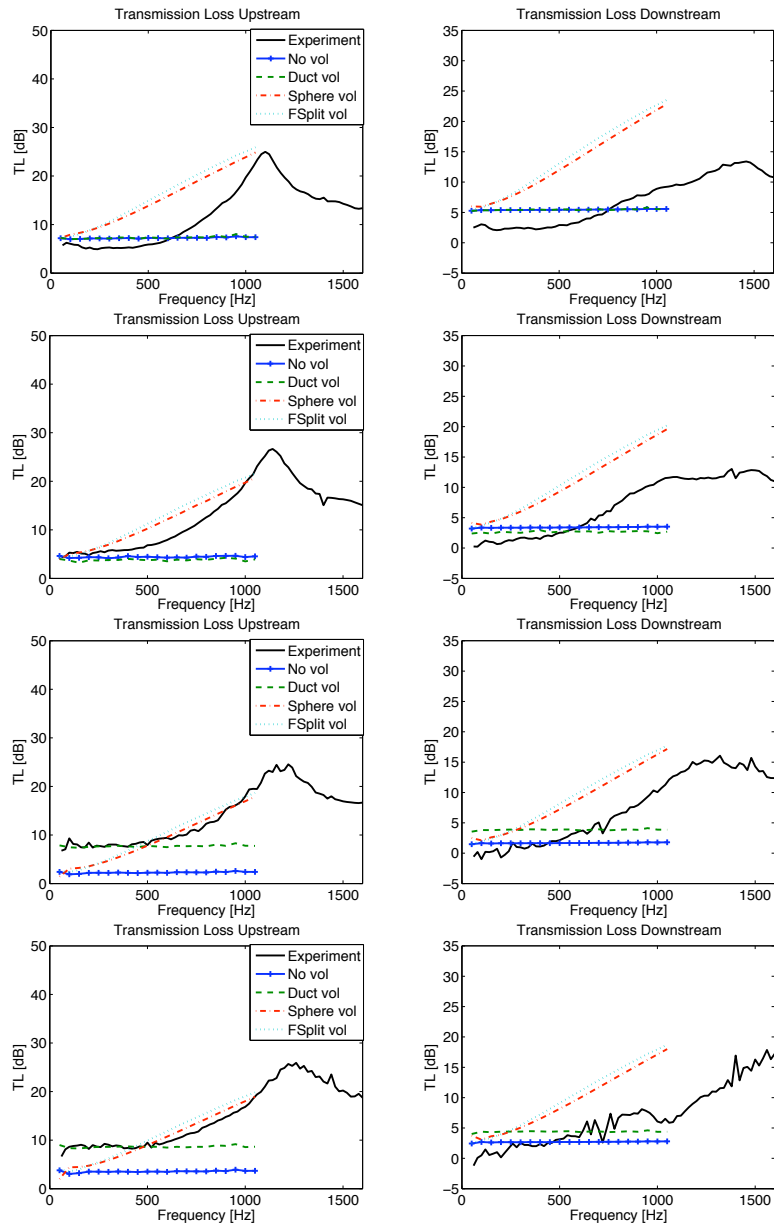
FIGURE 7.11. Comparison of the measured transmission loss and that computed with different setups and the un-damped map. For the operating points two to five, starting with two at the top, where the positions of the operating points in the map can be seen in Figure 7.6.
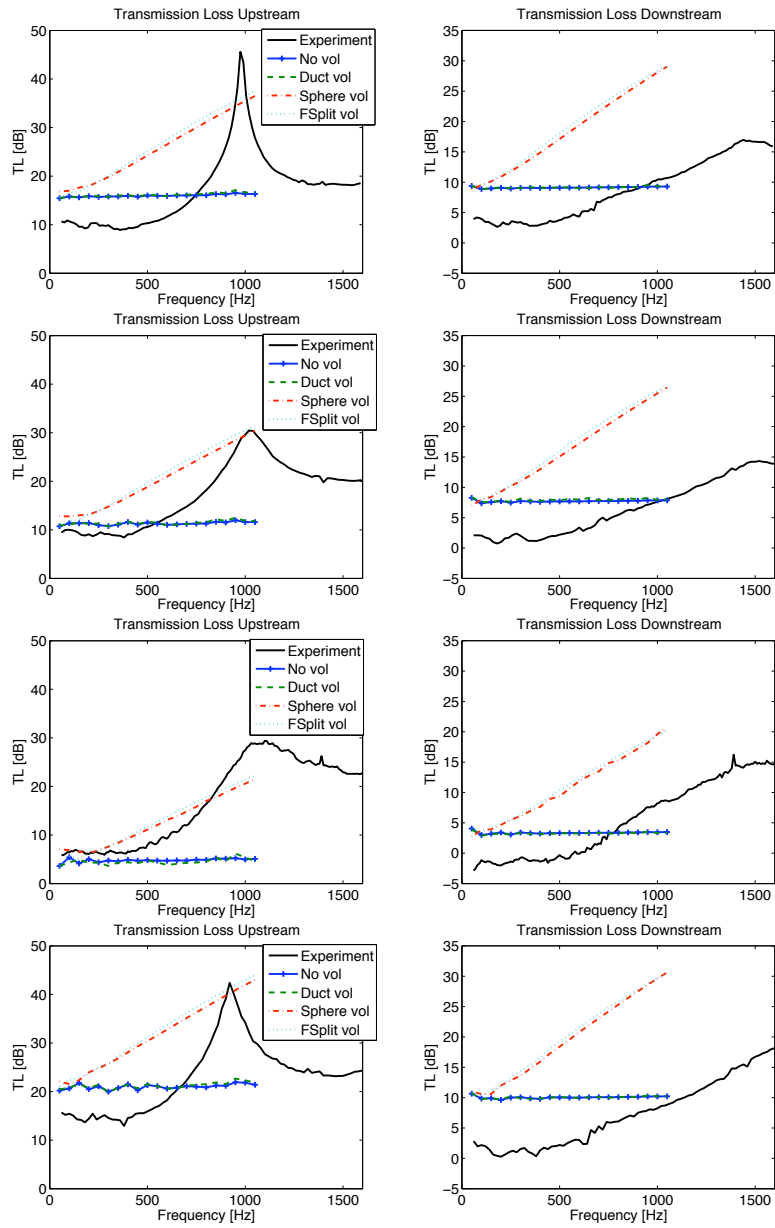
FIGURE 7.12. Comparison of the measured transmission loss and that computed with different setups and the un-damped map. For the operating points six to nine, starting with six at the top, where the positions of the operating points in the map can be seen in Figure 7.6.

the result for operating points close to the surge line, which is not desirable. For the lowest frequencies the damping does not significantly affect the result (except for the noise observed at some operating points). Compared to the measurements the damping improves the result slightly for the setup with only the map, by introducing a frequency dependence. However, there is still a large discrepancy due to the map giving the wrong level of the transmission loss and the frequency dependence introduced by the damping being different than that observed in the measurements, especially for the upstream transmission loss. For the setup with added volumes the damping increases the transmission loss to too high levels.
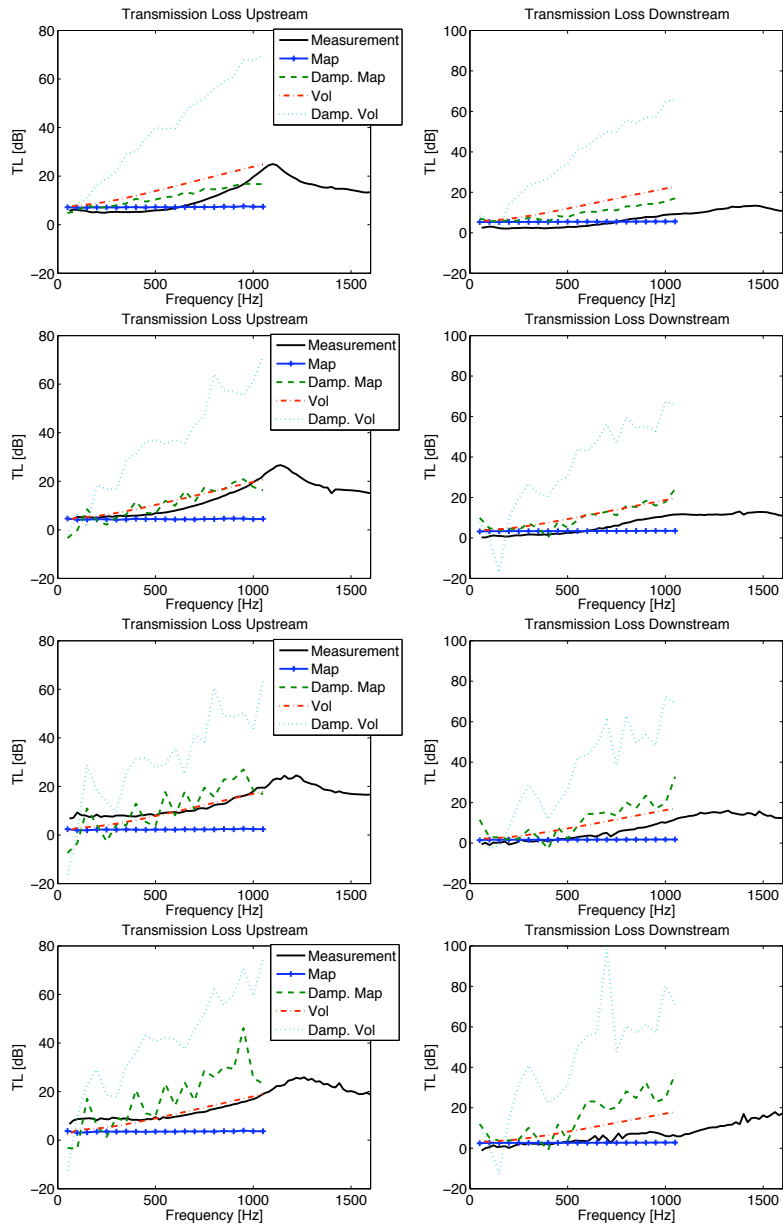
FIGURE 7.13. Comparison of the measured transmission loss and that computed with or without mass flow damping in the map. For the operating points two to five, starting with two at the top, where the positions of the operating points in the map can be seen in Figure 7.6.
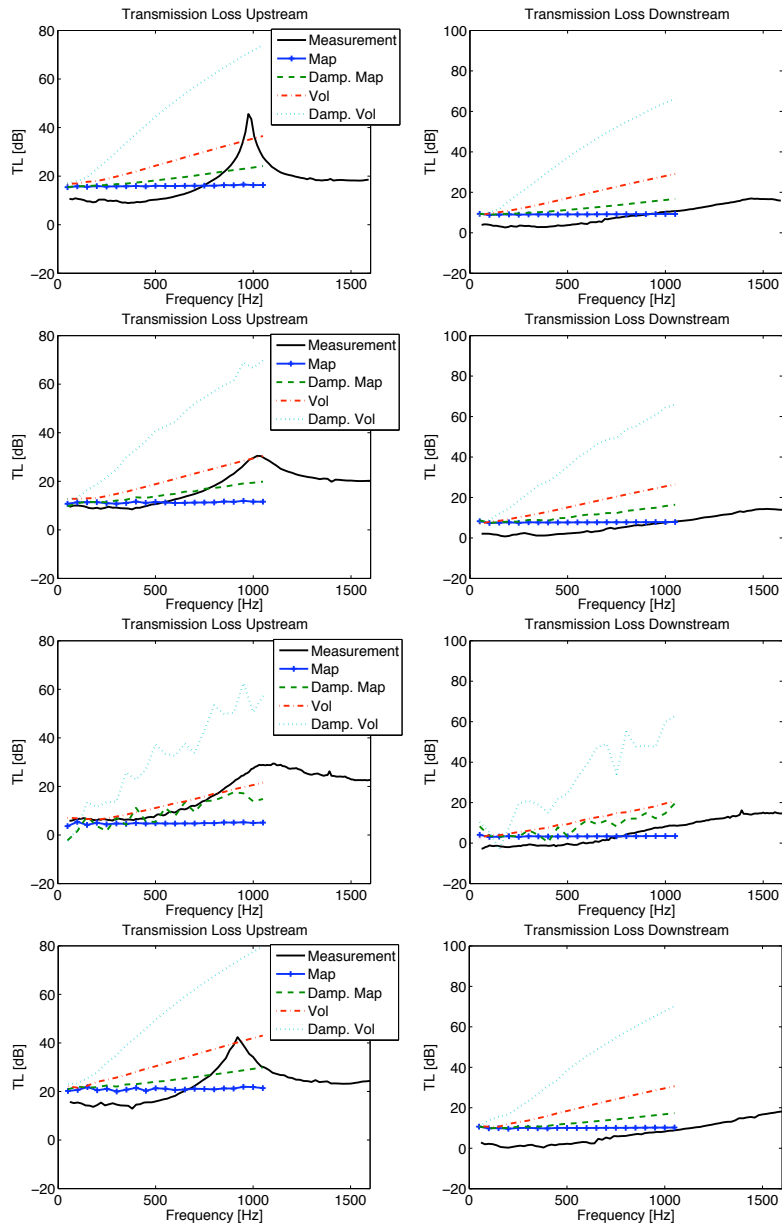
FIGURE 7.14. Comparison of the measured transmission loss and that computed with or without mass flow damping in the map. For the operating points six to nine, starting with six at the top, where the positions of the operating points in the map can be seen in Figure 7.6.

Summary, Conclusions and Future Work

8.1. 3D LES

In this work a method for studying the scattering of low frequency plane waves through LES has been investigated. The geometry used is a ducted orifice plate. The method is based on external excitation of a sum of harmonic acoustic waves and one of the main issues is to separate the acoustic fluctuations associated with these waves from the flow fluctuations. The effect of several different flow noise suppression methods have been evaluated with the following result:

- The excitation amplitude has to be carefully chosen, such that it is high enough to dominate over the flow generated noise and at the same time low enough to avoid non-linear effects. The performed simulations indicate that non-linear effects start to appear when the amplitude of the acoustic velocity fluctuations becomes higher than around 1 % of the mean velocity. When the in- and outlet boundary conditions are reflective resonance frequencies have to be avoided, since they give rise to high acoustic amplitudes and thereby non-linear effects.

- Using cross-section averages is an efficient way of suppressing turbulent fluctuations in the plane wave range. This method works better if slip boundary conditions are used at the walls of the duct. Thereby a uniform acoustic velocity at each cross-section is created.

- A sufficient number of phase averages have to be gathered in order to suppress statistical noise. The number of averages needed depends on the flow and where in the domain data is sampled.

- Correlating the sampled fluctuations with the excitation frequencies, to eliminate uncorrelated fluctuations, does not reduce the noise.

- Non-acoustic fluctuations can be suppressed by using the characteristics based filtering method such as proposed by Kopitz *et al.* (2005), i.e. averaging several cross-sections using the acoustic propagation speed. This does not however, give a significant effect if the mesh is stretched

so the turbulence is dissipated anyway while, the low frequency waves still are resolved.

The simulated scattering by the orifice plate has been compared to measurements for an inlet Mach number of 0.08. The downstream reflection and the down- to upstream transmission are in good agreement with the measurements. At the same time the amplitude of the upstream reflection, and partly also the up- to downstream transmission, becomes slightly too large compared to the measurements. However, it should be noted that the trend of a frequency independent scattering is present in both the simulations and the measurements. A rational explanation for the observed discrepancy has not yet been formulated, even though the effect of several different parameters have been studied with the following conclusions:

- The parameter that has the strongest influence on the result is the inlet Mach number. Decreasing the Mach number results in lower reflections and higher transmissions, as expected. However, the uncertainty in the inlet Mach number in the measurements cannot explain the observed discrepancy, since it affects all coefficients.

- Both the reflection and the transmission of waves coming from the upstream direction are too high, indicating that not enough of the acoustic energy is converted to vorticity at the plate edges in the simulations. This is also implied by the fact that the linear 2D simulations performed by Kierkegaard *et al.* (2008), using a mean flow at a lower Mach number ($M = 0.054$), gave good results compared to measurements and the fact that the change in the flow field when changing the wall boundary conditions from slip to no-slip did not significantly influence the result.

- The fact that the discrepancy only is seen for waves coming from the upstream direction could be explained by the acoustic waves seeing the geometry differently from the two directions due to the flow field. A wave coming from the upstream side clearly impinges on the upstream edge of the orifice, while the jet, with the vena contracta effect, partly hides the downstream edge from downstream excited waves. Errors in the prediction of the interaction between the wave and the sharp edge could therefore give a larger effect for waves coming from the upstream direction. An insufficient grid resolution at the plate could result in the observed effect. However, a grid refinement of this area did not improve the result.

8.1.1. *Future Work*

The work on the orifice configuration presented in this thesis will be continued in order to get a better understanding of the discrepancies found between the

simulations and the measurements. In the following work the sound generation will also be considered and methods, based on LES, to study the sound generating mechanisms in higher Mach number internal flows will be investigated. Besides new simulations, measurements of both the acoustics and the flow field will be performed, in order to validate the simulations.

The continued study will be performed for different flow situations, up to supersonic jet Mach numbers, to also investigate the effect of shocks. Furthermore, a thicker orifice plate will be considered to be able to study the whistling phenomena and the increase in acoustic energy that can be observed for the scattering at certain frequencies.

8.2. 1D Simulations

In industry 1D CFD programs for engine simulations are often used to predict engine performance. Sometimes also the acoustic pulsations, which are a part of the simulation, are studied. In this work the capability of the commercial program GT-Power to simulate the scattering of low frequency plane waves has been investigated for an orifice plate and a turbocharger compressor, respectively.

The orifice is a common object in engine models, which implies that it is important that it accurately can handle pulsating flows. Furthermore, it is a simple object that should be capable of predicting the pulsating flow. However, the amplitude of the simulated scattering of acoustic waves, at two inlet Mach numbers ($M = 0.08$ and $M = 0.054$), showed large discrepancies compared to measurements and theory. The most important results of the simulations are the following:

- Both measurements and theory predict a frequency independent scattering, while the simulations give a frequency dependence.

- By neglecting the plate thickness this frequency dependence is significantly reduced, but a large discrepancy could be observed for the level of the amplitude.

- An object parameter that is shown to have a significant influence on the level of the amplitude is the discharge coefficient, which is related to the vena contracta of the jet.

As a conclusion it can be said that by neglecting the plate thickness and specifying the discharge coefficient to a different value than the recommended it might be possible to tune the model to match the measurements. However, the discharge coefficient also affect the mean pressure drop over the orifice, which might not be desirable.

Compressors are usually modelled with performance maps, which describe their fluid mechanical properties at steady state. In GT-Power there is also an

option of damping the mass flow fluctuations, since they can become large even for small pressure fluctuations in some regions of the map. Simulations have been performed both with and without this damping. Furthermore, it has been tested to add artificial cavities (volumes) up- and downstream of the map to take into account the accumulation of mass inside the compressor during the acoustic pulse. It should however be mentioned that the code automatically adds a default orifice object between the volume and the map, which cannot be removed. The compressor transmission loss was simulated for nine compressor operating points and the results showed a large discrepancy compared to the measurements for all model setups. The most important effects of the different model setups are the following:

- The undamped map gives a frequency independent transmission loss, which also can be observed for lower frequencies in the measurements. There are however large discrepancies in the level for many of the operating points and there is no trend as to where in the map these points are located.

- Adding mass flow damping results in the transmission loss increasing with frequency, as seen in the measurements. However, the level at the lowest frequencies is not affected and the shape of the frequency dependence does not agree with the measurements. Furthermore, the damping does not seem to be completely linear and it introduced a scattering in the results for operating points where the damping is large.

- Adding volumes to the model also results in the transmission loss increasing with frequency. However, as for the damping the level at the lowest frequencies is not affected and the shape of the frequency dependence does not agree with the measurements.

As a conclusion it can be said that the compressor modelling used in GT-Power is not capable of correctly capturing the effect of the pressure pulsations (acoustic waves) that are a part of the simulations. It is however known that other 1D codes using a model consisting of a map and volumes are capable of capturing pressure pulsations, as is shown by Rämmal & Galindo (2010), who with good results used a similar model.

Acknowledgements

References

ÅBOM, M. 1991 Measurement of the scattering-matrix of acoustical two-ports. *Mechanical systems and signal processing* **5** (2), 89–104.

ADDAD, Y., LAURENCE, D., TALOTTE, C. & JACOB, M. 2003 Large eddy simulation of a forward-backward facing step for acoustic source identification. *International Journal of Heat and Fluid Flow* **24** (4), 562–571.

ALLAM, S. & ÅBOM, M. 2005 Aero-acoustic study of sigle and double diaphragm orifices under subsonic conditions. *Tech. Rep.*. KTH MWL, report prepared for Liebherr_Aerospace.

ANDERSON, J. 1995 *Computational fluid dynamics: the basics with applications*. McGraw-Hill.

BAILLY, C., BOGEY, C. & MARSDEN, O. 2010 Progress in direct noise computation. *International Journal of Aeroacoustics* **9** (1), 123–144.

BAINES, N. 2005 *Fundamentals of turbocharging*. Concepts NREC, White River Junction, Vt.

BOGEY, C. & BAILLY, C. 2005 Decrease of the effective Reynolds number with eddy-viscosity subgrid-scale modeling. *AIAA journal* **43** (2), 437–439.

BOGEY, C. & BAILLY, C. 2007 An analysis of the correlations between the turbulent flow and the sound pressure fields of subsonic jets. *Journal of Fluid Mechanics* **583**, 71–97.

BORIS, J., GRINSTEIN, F., ORAN, E. & KOLBE, R. 1992 New insights into large eddy simulation. *Fluid dynamics research* **10** (4-6), 199–228.

CHEN, H., HAKEEM, I. & MARTINEZ-BOTAS, R. 1996 Modelling of a turbocharger turbine under pulsating inlet conditions. *Proceedings of the Institution of Mechanical Engineers. Pt. A. Journal of Power and Energy* **210**, 397–408.

CHEN, H. & WINTERBONE, D. 1990 A method to predict performance of vaneless radial turbines under steady and unsteady flow conditions. *Proc. Inst. Mech. Eng., Part C: Mech. Eng. Sci., Proceedings of IMechE C* **405**.

CHUNG, J. & BLASER, D. 1980 Transfer function method of measuring in-duct acoustic properties. I. Theory. *The Journal of the Acoustical Society of America* **68**, 907–913.

COLONIUS, T. & LELE, S. 2004 Computational aeroacoustics: progress on nonlinear problems of sound generation. *Progress in Aerospace sciences* **40** (6), 345–416.

DIXON, S. 2005 *Fluid mechanics, thermodynamics of turbomachinery*. Butterworth-Heinemann.

DOKUMACI, E. 1998 On transmission of sound in circular and rectangular narrow pipes with superimposed mean flow. *Journal of sound and vibration* **210** (3), 375–389.

DURRIEU, P., HOFMANS, G., AJELLO, G., BOOT, R., AURÉGAN, Y., HIRSCHBERG, A. & PETERS, M. 2001 Quasisteady aero-acoustic response of orifices. *The Journal of the Acoustical Society of America* **110**, 1859.

ELIASSON, P. 2001 Edge, a navier-stokes solver for unstructured grids. *Tech. Rep..* Division of Aeronautics, FOI-Swedish Defence Research Agency.

EWERT, R. & SCHRÖDER, W. 2003 Acoustic perturbation equations based on flow decomposition via source filtering. *Journal of Computational Physics* **188** (2), 365–398.

FFOWCS WILLIAMS, J. & HAWKINGS, D. 1969 Sound generation by turbulence and surfaces in arbitrary motion. *Philosophical Transactions of the Royal Society of London. Series A, Mathematical and Physical Sciences* **264** (1151), 321.

FÖLLER, S. & POLIFKE, W. 2010 Determination of acoustic transfer matrices via large eddy simulation and system identification. In *16th AIAA/CEAS Aeroacoustics Conference*.

FÖLLER, S., POLIFKE, W. & TONON, D. 2010 Aeroacoustic characterization of t-junctions based on large eddy simulation and system identification. In *16th AIAA/CEAS Aeroacoustics Conference*.

FUKANO, T. & JANG, C. 2004 Tip clearance noise of axial flow fans operating at design and off-design condition. *Journal of Sound and Vibration* **275** (3-5), 1027–1050.

GLAV, R. & ÅBOM, M. 1997 A general formalism for analyzing acoustic 2-port networks. *Journal of Sound and Vibration* **202** (5), 739–747.

GLOERFELT, X. & LAFON, P. 2008 Direct computation of the noise induced by a turbulent flow through a diaphragm in a duct at low Mach number. *Computers & Fluids* **37** (4), 388–401.

GRINSTEIN, F., MARGOLIN, L. & RIDER, W. 2007 *Implicit large eddy simulation: computing turbulent fluid dynamics*. Cambridge Univ Pr.

GRÖSCHEL, E., SCHRÖDER, W., RENZE, P., MEINKE, M. & COMTE, P. 2008 Noise prediction for a turbulent jet using different hybrid methods. *Computers & Fluids* **37** (4), 414–426.

GT-POWER 2004 *User's Manual*. Gamma Technologies.

HEYWOOD, J. 1988 *Internal combustion engine fundamentals*. McGraw-Hill New York.

HOLMBERG, A. 2010 Experimental determination of aeroacoustic sources in low mach number internal flows. Licentiate thesis, KTH.

HOLSTE, F. & NEISE, W. 1997 Noise source identification in a propfan model by means of acoustical near field measurements. *Journal of Sound and Vibration* **203** (4), 641–665.

HOWE, M. 1998 *Acoustics of fluid-structure interactions*. Cambridge Univ Pr.

INGARD, U. & ISING, H. 1967 Acoustic Nonlinearity of an Orifice. *The Journal of the Acoustical Society of America* **42**, 6–17.

JAMESON, A., SCHMIDT, W. & TURKEL, E. 1981 Numerical solutions of the Euler equations by finite volume methods using Runge-Kutta time-stepping schemes. *AIAA paper* **81**, 1259.

JAPIKSE, D. & BAINES, N. 1994 *Introduction to turbomachinery*. Concepts Eti.

KAMEIER, F. & NEISE, W. 1997 Rotating blade flow instability as a source of noise in axial turbomachines. *Journal of Sound and Vibration* **203** (5), 833–853.

KIERKEGAARD, A. ., EFRAIMSSON, G. & BOIJ, S. 2008 Acoustic propagation in a flow duct with an orifice plate. In *ISMA conference*. Leuven, Belgium.

KIERKEGAARD, A. & EFRAIMSSON, G. 2007 Generation and propagation of sound waves in low mach number flows. In *Proceedings of the 13th AIAA-CEAS Acoustics conference*. Rome, Italy.

KIERKEGAARD, A., EFRAIMSSON, G., BOIJ, S. & ÅBOM, M. 2010 Simulations of the whistling potentiality of an in- duct orifice with linear aeroacoustics. In *16th AIAA/CEAS Aeroacoustics Conference*.

KNUTSSON, M. & ÅBOM, M. 2010 The effect of turbulence damping on acoustic wave propagation in tubes. *Journal of Sound and Vibration* .

KOPITZ, J., BRÖCKER, E. & POLIFKE, W. 2005 Characteristics-based filter for identification of planar acoustic waves in numerical simulation of turbulent compressible flow. In *12th Int. Congress on Sound and Vibration*. Lisabon.

LAI, H. & LUO, K. 2007 A three-dimensional hybrid LES-acoustic analogy method for predicting open-cavity noise. *Flow, turbulence and combustion* **79** (1), 55–82.

LAVRENTJEV, J., ÅBOM, M. & BODÉN, H. 1995 A measurement method for determining the source data of acoustic two-port sources. *Journal of Sound and Vibration* **183** (3), 517–531.

LEUNG, R., WANG, M., LI, X., SO, R. & STUDENT, P. 2005 Sound Absorption by In-duct Orifice. In *11 th AIAA/CEAS Aeroacoustics Conference (26 th Aeroacoustics Conference)*, pp. 1–9. Monterey, California.

LIGHTHILL, M. 1952 On sound generated aerodynamically. I. General theory. *Proceedings of the Royal Society of London. Series A, Mathematical and Physical Sciences* **211** (1107), 564–587.

MAILACH, R., LEHMANN, I. & VOGELER, K. 2001 Rotating instabilities in an axial compressor originating from the fluctuating blade tip vortex. *Journal of Turbomachinery* **123**, 453.

MCALPINE, A. & FISHER, M. 2001 On the prediction of" buzz-saw" noise in aeroengine inlet ducts. *Journal of Sound and Vibration* **248** (1), 123–149.

MCALPINE, A., FISHER, M. & TESTER, B. 2006 Buzz-saw noise: A comparison of measurement with prediction. *Journal of Sound and Vibration* **290** (3-5), 1202–1233.

PAYRI, F., BENAJES, J. & REYES, M. 1996 Modelling of supercharger turbines in internal-combustion engines. *International Journal of Mechanical Sciences* **38** (8-9), 853–869.

PEAT, K., TORREGROSA, A., BROATCH, A. & FERNÁNDEZ, T. 2006 An investigation

into the passive acoustic effect of the turbine in an automotive turbocharger. *Journal of Sound and Vibration* **295** (1-2), 60–75.

PIELLARD, M. & BAILLY, C. 2010 Several computational aeroacoustics solutions for the ducted diaphragm at low mach number. In *16th AIAA/CEAS Aeroacoustics Conference*.

PIERCE, A. 1989 *Acoustics: an introduction to its physical principles and applications*. Acoustical Society of Amer.

RAITOR, T. & NEISE, W. 2008 Sound generation in centrifugal compressors. *Journal of Sound and Vibration* **314** (3-5), 738–756.

RÄMMAL, H. & ÅBOM, M. 2007 Acoustics of turbochargers. In *SAE International*.

RÄMMAL, H. & ÅBOM, M. 2009 Experimental determination of sound transmission in turbo-compressors. In *SAE Technical Paper no. 2009-0101*.

RÄMMAL, H. & GALINDO, J. 2010 The passive acoustic effect of turbo-compressors. In *9th International Conference on Turbochargers and Turbocharging*.

RUPP, J., CARROTTE, J. & SPENCER, A. 2010 Interaction between the acoustic pressure fluctuations and the unsteady flow field through circular holes. *Journal of Engineering for Gas Turbines and Power* **132**, 061501.

SERRANO, J., ARNAU, F., DOLZ, V., TISEIRA, A. & CERVELLÓ, C. 2008 A model of turbocharger radial turbines appropriate to be used in zero-and one-dimensional gas dynamics codes for internal combustion engines modelling. *Energy Conversion and Management* **49** (12), 3729–3745.

SERRANO, J., TORREGROSA, A., DOPAZO, J. & SOLTANI, S. 2006 Experiments on Wave Transmission and Reflection by Turbochargers in Engine Operating Conditions. In *SAE international*. SAE International.

TESTUD, P., AURÉGAN, Y., MOUSSOU, P. & HIRSCHBERG, A. 2009 The whistling potentiality of an orifice in a confined flow using an energetic criterion. *Journal of Sound and Vibration* **325** (4-5), 769–780.

TIIKOJA, H., RÄMMAL, H., ÅBOM, M. & BODÉN 2010 Test-rig for complete acoustic characterization of turbochargers. In *16th AIAA/CEAS Aeroacoustics Conference*.

TORREGROSA, A., BROATCH, A., CLIMENT, H. & FERNÁNDEZ, T. 2006 Time-domain modelling of turbo-compressors in direct injection diesel engines. *Proceedings of the Institution of Mechanical Engineers, Part D: Journal of Automobile Engineering* **220** (4), 445–457.

TYLER, J. & SOFRIN, T. 1962 Axial flow compressor noise studies. *Transactions of the Society of Automotive Engineers* **70**, 309–332.

WAGNER, C., HÜTTL, T. & SAGAUT, P. 2007 *Large-eddy simulation for acoustics*. Cambridge Univ Pr.

WATSON, N. & JANOTA, M. 1982 *Turbocharging the internal combustion engine*. MacMillan London.